Demystifying mass transfer in electrolysis through 3D printed reactors

Citation for published version (APA):
Weusten, S. J-M. C. (2022). *Demystifying mass transfer in electrolysis through 3D printed reactors*. [Phd Thesis 1 (Research TU/e / Graduation TU/e), Chemical Engineering and Chemistry]. Eindhoven University of Technology.

Document status and date:
Published: 01/04/2022

Document Version:
Publisher’s PDF, also known as Version of Record (includes final page, issue and volume numbers)

Please check the document version of this publication:

• A submitted manuscript is the version of the article upon submission and before peer-review. There can be important differences between the submitted version and the official published version of record. People interested in the research are advised to contact the author for the final version of the publication, or visit the DOI to the publisher's website.
• The final author version and the galley proof are versions of the publication after peer review.
• The final published version features the final layout of the paper including the volume, issue and page numbers.

Link to publication

General rights
Copyright and moral rights for the publications made accessible in the public portal are retained by the authors and/or other copyright owners and it is a condition of accessing publications that users recognise and abide by the legal requirements associated with these rights.

- Users may download and print one copy of any publication from the public portal for the purpose of private study or research.
- You may not further distribute the material or use it for any profit-making activity or commercial gain
- You may freely distribute the URL identifying the publication in the public portal.

If the publication is distributed under the terms of Article 25fa of the Dutch Copyright Act, indicated by the “Taverne” license above, please follow below link for the End User Agreement:

www.tue.nl/taverne

Take down policy
If you believe that this document breaches copyright please contact us at:

openaccess@tue.nl

providing details and we will investigate your claim.

Download date: 04. Oct. 2023

Demystifying mass transfer in electrolysis through 3D printed reactors

PROEFSCHRIFT

ter verkrijging van de graad van doctor aan de Technische Universiteit Eindhoven, op gezag van de rector magnificus prof.dr.ir. F.P.T. Baaijens, voor een commissie aangewezen door het College voor Promoties in het openbaar te verdedigen op vrijdag 1 april 2022 om 13:30 uur

door

Stéphane Jean-Marie Christian Weusten

geboren te Tongeren, België

Dit proefschrift is goedgekeurd door de promotoren en de samenstelling van de promotiecomissie is als volgt:

Voorzitter: prof.dr. F. Gallucci
Promotor: prof.dr.ir. J. van der Schaaf
Copromotor : dr. M.T. de Groot
Leden: prof.dr.ir. G. Mul (Universiteit Twente)
prof.dr.ir. J.A.M. Kuipers
prof.dr.ir. A.W. Vreman
prof.dr. T. Breugelmans (Universiteit Antwerpen)

Het onderzoek of ontwerp dat in dit proefschrift wordt beschreven is uitgevoerd in overeenstemming met de TU/e Gedragscode Wetenschapsbeoefening

Demystifying mass transfer in electrolysis through 3D printed reactors

Stéphane Weusten
Eindhoven University of Technology, 2022

A catalogue record is available from the Eindhoven University of Technology Library

This research was funded under the HIGHSINC project

Design by Stéphane Weusten
Cover by Studio Vreys
Printed by Eurographics

Summary

Electrolyzers are likely to play a pivotal role in the energy transition from fossil to electric. This is because they are particularly suited for Power-to-X processes where electric energy is converted into a.o. chemical energy. Fully embracing this opportunity requires a deeper understanding of the current technology and it's limitations. One key parameter in the performance of electrolyzers is the rate of mass transfer. Often, electrochemical reactions are mass transfer limited due to fast kinetics that depend exponentially on the applied overpotential. Numerous correlations exist in literature that describe the rate of mass transfer. However, their predictions can vary up to almost an order of magnitude. The reason for this is the large geometric variety between the reactors that were investigated. In order to find a general description of mass transfer it is therefore nescessary to build and test many different reactor geometries. Additive manufacturing is particularly useful for this purpose, as it allows the rapid and inexpensive prototyping of highly customized reactors.

Electrochemical mass transfer studies are typically performed using the limiting current density method and the hexacyanoferrate(II)/ hexacyanoferrate(III) redox couple. However, this couple causes irreversible electrode poisoning which can lead to unreliable measurements. In **chapter 2**, hexachloroiridate(III)/hexachloroiridate(IV) is therefore investigated as an alternative. Using cyclic and linear sweep voltammetry, it is shown that hexachloroiridate is reversible and has a clearly defined limiting current density plateau suitable for limiting current density measurements. The stability of hexachloroiridate and hexacyanoferrate is compared during 16 hour long chronoamperometric experiments. During this time, electrode poisoning does not occur for the hexachloroiridate couple. However, there is a significant loss of bulk concentration due to degradation of the complex. The degradation depends on the pH and is least severe in acidic solutions (pH 2-3). This is in contrast to the hexacyanoferrate couple, which is more stable in solution but causes electrode poisoning.

In **chapter 3**, a 3D printed parallel plate reactor is used to determine the effect of the inlet type, entrance length and turbulence promoters on space-averaged mass transfer. It is shown that the inlet significantly influences the rate of mass transfer (up to a factor 2.2 increase). Furthermore, an earlier transition to turbulent flow is observed. The extent of both effects can be predicted by the ratio of the cross-sectional areas of the inlet to the channel. Expanding the entrance length reduces these effects and results in calmer flow. Gyroid-type turbulence promoters on the other hand increase mixing and result in a factor 2 to 4 mass transfer enhancement. Between different configurations, there is a minimal variation in pressure drop (<16 mbar).

On the local scale, significant variations can occur as a result of the inlet. This is investigated in **chapter 4** using segmented electrodes. The degree of non-uniformity corresponds to the cross-sectional area ratio of the inlet to the channel. However, the flow patterns can be complex and difficult to predict. The addition of a calming section results in increased uniformity at the cost of lower averaged mass transfer. Turbulence promoters result in uniformly high mass transfer. The lengthwise, one-dimensional, mass transfer profile is described well using equations of the form $Sh_x = a\, Re^b\, Sc^{0.33}\, (d_H/x)^d$. Herein, the Reynolds power b is representative of the flow condition and the constant d describes the local mass transfer dependency.

In **chapter 5**, the commercially available Electrocell MicroFlow and MP cells are investigated. Mass transfer correlations are establishd and the effect of the accompanying turbulence promoter is evaluated. The performance is similar to other reactors in literature. For the Electrocell MicroFlow cell, the effect of mesh electrodes is explored. These 3D electrodes act as turbulence promoters while simultaneously increasing the available electrode area. Woven and expanded mesh electrodes result in a factor 2.1 to 2.8 mass transfer enhancement solely due to turbulence promotion. Due to the increased electrode area, this results in an overall reaction rate that is a factor 5.9 to 6.7 faster for woven meshes, and a factor 1.9 to 3.0 for expanded meshes.

Introduction

1 - The energy transition and its opportunities

Throughout history, energy transitions have defined the progress of humanity.[1] The discovery of fire allowed our paleolithic ancestors to thrive, the discovery of coal drove industrialization and the exploitation of oil and gas is the beating heart behind our modern world. With each discovery, new opportunities emerged as our way of life was disrupted by new technologies. The advent of steam engines for instance, meant that we could replace physical labor with automated machinery. Less time needed to be spent on tedious, repetitive tasks and productivity increased dramatically. However, these new opportunities lead to new challenges: as more coal-powered factories were built, cities slowly filled with noxious gases. To improve the quality of life, cleaner methods of energy production were needed and as a result the path to another energy transition was set in motion. In the current age, we find ourselves in a similar situation. Our way of life, supported by a global oil economy, has led to significant strain on the environment. As a result, we are once again changing our energy infrastructure. Renewable energy is becoming increasingly important as an alternative to fossil fuels. In the year 2000, the renewable share of power generation was 18%. In 2018, this share reached 25%.[1]

Image: the lightbulb is not just a symbol of electricity, it is the symbol of a great idea

For the chemical industry, electrification can potentially offer many advantages. For instance, higher product qualities, more flexibility and increased safety can be achieved on top of a reduction in greenhouse gas emissions.[2] Therefore, there is an increasing attention towards electricity conversion pathways, which are also called Power-to-X.[3] Among these are: Power-to-Heat, Power-to-Fuels, Power-to-Steel, Power-to-Hydrogen, Power-to-Ammonia, Power-to-Chemicals in general, and so on.[3,4] For electrochemical engineers, this results in significant opportunities, as many of the Power-to-X conversions can be achieved through electrochemical reactions. For instance there is the the electroreduction of CO2 to produce fuels and chemicals, water electrolysis to produce hydrogen, the direct electroreduction of iron oxide to produce steel, nitrogen electroreduction to produce ammonia, the chlor-alkali process which produces chorine and caustic soda, and others. [1,5-9] It is therefore likely that electrochemical reactors will play a significant role in the global energy transition.

To facilitate the transition, new electrochemical reactors should achieve high cost-effectiveness. At the same time, in order to be sustainable and adhere to increasingly strict regulations, they will need to be cleaner, more efficient, and use fewer scarce resources (such as platinum or ruthenium). Furthermore, due to the intermittency of renewable energy sources, flexible operation is key. This is in contrast to existing electrolyzers, which typically rely on relatively constant base-load power. The combination of these demands creates an interesting challenge for the next generation of electrochemical reactors. To overcome this challenge, it is nescessary to deepen the understanding of electrolyzer technology and its limits.

1.1. Electrochemical mass transfer

The reaction rate of an electrochemical process is dependent on mass transfer and the reaction kinetics. Typically, the reaction kinetics can be fast because they depend exponentially on the applied overpotential. The overpotential is the difference between the thermodynamic potential and the applied potential. Because of this exponential dependency, a small increase in overpotential results in a large increase in kinetic reaction rate. Usually this means that electrochemical reactions have very fast kinetics at a sufficiently high overpotential. Mass transfer on the other hand is a comparatively slow process. Assuming a sufficient overpotential is applied, this results in an overall reaction rate that is mass transfer limited.

There are three main modes of mass transfer from the bulk of the electrolyte solution to the electrode: diffusion, convection, and migration. These are shown in eq.1[10,11]

$$-R_A = \frac{i_A}{nF} = -D\left(\frac{\partial C}{\partial y}\right) + v\,C - D\,C\left(\frac{nF}{RT}\right)\left(\frac{\partial \Psi}{\partial y}\right) \qquad \text{eq.1}$$

Where i_A is the current density, n is the number of electrons exchanged and F is Faraday's number, i.e. 96485 C/mol. The first term represents diffusion, which is a function of the diffusion coefficient D and the concentration gradient ($\partial C/\partial y$). The negative sign indicates that the gradient is negative. The second term represents convection, which is a function of the hydrodynamic flow velocity v and the concentration C. This term is typically zero as there is no net bulk flow of ions from the solution to the electrode in this particular direction (perpendicular to the electrode). For processes such as metal deposition, this term is not strictly zero. Nevertheless, the term can safely be assumed zero considering the net bulk flow is negligible (<0.3%) compared to the total flux. [11] The final term represents migration, which depends on the gradient of electrostatic forces ($\partial\Psi/\partial \mathrm{y}$), the diffusion coefficient D, the concentration C, the number of electrons n, the faraday constant F, the inverse of the temperature T and the inverse of the ideal gas constant R.

The rate of mass transfer can be influenced in several ways: First, by using a higher bulk concentration of electroactive species, a higher rate of diffusion is achieved. If the species and the electrode are of opposite charge, this also results in a positive effect on migration. Second, the diffusion constant D can be improved by increasing the temperature or decreasing the viscosity of the solution. This affects the diffusion positively and the migration term either positively or negatively depending on the charge of the species and the electrode. Finally and perhaps most importantly, increasing the rate of mixing decreases the thickness of the diffusion layer δy. This in turn significantly enhances the rate of diffusion.

The mixing performance can be measured by using what is known as the limiting current density method.[11] First, a supporting electrolyte is introduced, which is an inert electrolyte that can carry the electric charge in the solution. As long as the concentration of the supporting electrolyte is high compared to the electroactive species, this means that the migration term in eq.1 can be neglected. By removing the negligible terms (convection and migration), we can simplify eq.1 and obtain eq.2a.

$$\frac{i_A}{nF} = -D\left(\frac{\partial C}{\partial y}\right) \qquad \text{eq.2a}$$

By assuming a diffusion boundary layer, the equation resolves into eq.2b:

$$\frac{\mathrm{i_A}}{\mathrm{nF}} = \frac{\mathrm{D}}{\delta}(\mathrm{C_{bulk}} - \mathrm{C_e}) \qquad \text{eq.2b}$$

Here, δ is the thickness of the diffusion boundary layer, and C_{bulk} and C_e the concentration of the electroactive species in respectively the bulk and at the electrode. The ratio D/δ is commonly written as the liquid-solid mass transfer coefficient k_{ls}. When the overpotential is sufficiently high, the ions at the electrode deplete significantly faster than they are replenished by mass transfer. In a completely mass transfer limited situation, the result is that C_e becomes essentially zero. In this situation, the measured current density is also known as the limiting current density $i_{A,lim}$. The mass transfer coefficient k_{ls} is directly proportional to $i_{A,lim}$.

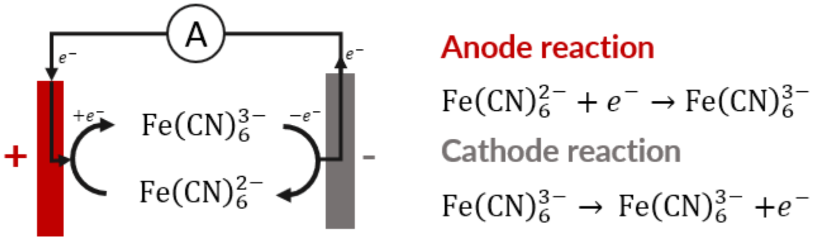

Figure 1: Illustration of the hexacyanoferrate(II)/hexacyanoferrate(III) redox couple and its half reactions. Electroactive species reacting on the anode are regenerated on the cathode and vice versa.

Measurements of the limiting current density typically involves the use of reversible redox couples. A reversible redox couple is a reducing agent combined with its oxidized form, such as e.g. hexacyanoferrate(II)/ hexacyanoferrate(III). A benefit of using these is that the bulk concentration C_{bulk} will remain more or less constant throughout the measurement. As can be seen in figure 1, this is because the half reactions are the reverse of one another and consequently, there should be no net conversion of species. In practice however, a loss of bulk concentration may still be observed. This is because the redox couple can suffer from side reactions or insufficient stability. For hexacyanoferrate(II)/hexacyanoferrate(III) in particular, there is a known poisoning problem that can severely affect the accuracy of the measurements. This poisoning problem is the result of a side reaction that deposits an inhibiting layer onto the electrodes. Although many strategies exist to alleviate this problem, none of them fully eliminate it.[12] Therefore, alternative redox couple such as hexachloroiridate(III)/hexachloroiridate(IV) are particularly interesting as they seem to avoid electrode poisoning entirely.[13,14] However, much remains to be discovered about them and their use in mass transfer studies.

1.2. Improved reactor design through additive manufacturing

Numerous correlations in literature exist to describe the rate of mass transfer in a specific reactor.[15] Despite this, it is difficult to predict the performance of an electrolyzer. This is because the correlations in literature show a large variation of performance depending on the design of the reactor. Furthermore, it is yet unknown how different geometric choices affect mass transfer. This is especially the case when more complex flow patterns are present. In order to demistify the different effects, it is therefore ideal to build and test a great number of different designs. Using traditional manufacturing, this is time-consuming and cost-ineffective.

With the advent of additive manufacturing as a consumer technology, an alternative method now exists to build highly customized components. This technology offers several advantages compared to traditional manufacturing and machining: First, additive manufacturing is fast and requires relatively few manual operations. This has the added consequence of making it less expensive. Second, more complex features can be built than was previously possible. This is because a 3D printed piece is built layer by layer, which allows every part of it to be accessed by the tool head. In CNC milling for instance, an enclosed space cannot be built because the drill head cannot reach it. This also simplifies the design process, as it is often not nescessary to consider how the tool will reach the feature. In essence, additive manufacturing allows us to rapidly build and test highly customized designs. For mass transfer studies, this is particularly interesting as many designs can be built in short notice. Moreover, an iterative design philosophy can be used as it is inexpensive to redesign and rebuild parts that do not meet the expected performance targets. This is in contrast to traditional manufacturing, where it is nescessary to minimize the number of redesigns due to cost and time-consumption.

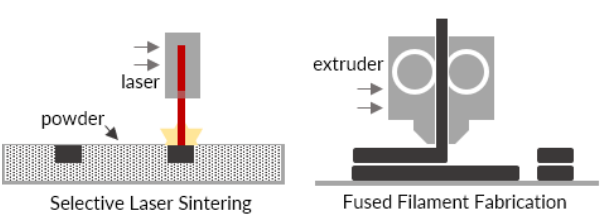

Figure 2: Illustration of the different 3D printing techniques. Left: SLS, middle: FFF, right: SLA.

Currently, there are three main methods of additive manufacturing: selective laser sintering (SLS), fused filament fabrication (FFF) and stereolithography (SLA). With SLS, a powder of a source material is selectively fused into a complete part using the heat of a high power laser. This method can be used to print both metals and certain plastics such as nylon and polypropylene. With FFF, a thermoplastic is fed through an extruder that continuously moves around the build plate to deposit a layer of molten plastic. Most thermoplastics can be printed in this way, though the most common are polylactic acid (PLA) and acrylonitrile butadiene styrene (ABS). Finally, with SLA, a liquid solution of UV-reactive monomers and oligomers is selectively hardened by lighting it with a UV-light source. Only a few specific, often proprietary polymers are able to be used for this method. Each of these methods offers different advantages and disadvantages. Notable advantages are that SLS can be used to print free-floating structures, FFF offers a large selection of materials, and SLA generally results in the finest details. The most important disadvantages are that: SLS requires expensive equipment, FFF is the least accurate, and that SLA can typically only build smaller objects with very little choice of material.

1.3. Scope and outline

The goal of this thesis is to demistify mass transfer in electrolysis. To that end, we developed a 3D printed lab-scale electrolyzer. The electrolyzer is a modular reactor of which the inlets, outlets, entry length and electrode assembly can easily be exchanged. Using this modular electrolyzer, various configurations and geometric design choices can be evaluated. For each configuration, the mass transfer performance is measured using the limiting current density method.

In **chapter 2**, hexachloroiridate(III)/hexachloroiridate(IV) is explored as an alternative redox couple to the traditionally used hexacyanoferrate(II)/ hexacyanoferrate(III). This is done to avoid the concerns with electrode poisoning that the latter couple poses. Cyclic voltammetry, linear sweep voltammetry, and chronoamperometry are used to compare the behavior of both redox couples.

In **chapter 3**, the space-averaged mass transfer of parallel-plate electrolyzers is investigated. In literature, a large variation up to a factor 10 is observed in mass transfer performance. The contribution of the inlet design to this variation is investigated in 3D printed electrolyzers. In **chapter 4**, similar investigations are performed on the local scale using segmented electrodes. Three different segmentation patterns (matrix, series and inlet-focused) were used. Moreover, the effect of turbulence promoters is shown on the local scale.

In **chapter 5**, two commercially available electrolyzers are investigated: the ElectroCell Microflow cell, and the ElectroCell MP cell. Mass transfer correlations are established for both the empty channel and for the channel with a turbulence promoter. These are compared to literature results for the ElectroCell ElectroSyn cell. Finally, the mass transfer enhancement by 3D mesh electrodes is explored in the ElectroCell microflow cell.

References

[1] International Renewable Energy Agency, Global energy transformation: A roadmap to 2050 (2019 edition), IRENA, Abu Dhabi, 2019.

[2] Wei M, McMillan C and de la Rue du Can S, Electrification of industry: potential, challenges and outlook, Current Sustainable/Renewable Energy Reports, no. 6, pp. 140-148, 2019

[3] Byfeld S and Vetter D, Flexibility concepts for the German power supply in 2050, Acatech, Munich, 2016

[4] Smith W, Burdyny T, Vermaas D and Geerlings H, Pathways to Industrial-Scale Fuel Out of Thin Air from CO2 Electrolysis, Joule, vol. 3, no. 8, pp. 1822-1834, 2019

[5] O'Brien T, Bommaraju T and Hine F, History of the Chlor-Alkali Industry, in Handbook of Chlor-Alkali technology, Sspringer, New York, 2004, pp. 17-36.

[6] Schiffer ZJ, Manthiram K, Electrification and decarbonization of the chemical industry industry, Joule, vol. 1, pp. 10-4, 2017.

[7] Maggio ANG, Andaloro APF and Squadrito G., Green hydrogen as feedstock: Financial analysis of a photovoltaic-powered electrolysis plant, Int. J. of Hydr. Energ., vol. 45, no. 20, pp. 11395-11408, 2020.

[8] Varela C, Mostafa M and Zondervan E, Modeling alkaline water electrolysis for power-to-x applications: A scheduling approach, Int. J. of Hydr. Energ., vol. 46, no. 14, pp. 9303-9313, 2021.

[9] Vogl V, Åhman M and Nilsson L, Assessment of hydrogen direct reduction for fossil-free steelmaking, J. of Cleaner Prod., vol. 203, pp. 736-745, 2018.

[10] Bard A and Faulkner L, Electrochemical methods: fundamentals and applications, New York: John Wiley & Sons, 2001.

[11] Mizushina T, The electrochemical method in transport phenomena, Adv. in heat transf. , vol. 7, pp. 87-161, 1971.

[12] Szánto DA, Cleghorn S, Ponce-de-Léon C and Walsh FC, The Limiting Current for Reduction of the Ferricyanide Ion at Nickel, AIChE, 54 (2008) 802.

[13] Meyer T and Taube H, Electron-transfer reactions of ruthenium ammines, Inorg. Chem., vol. 7, no. 11, pp. 2369-2379, 1968.

[14] Petrovic S, Cyclic Voltammetry of Hexachloroiridate(IV): An Alternative to the Electrochemical Study of the Ferricyanide Ion, Chem. Educator, 5 (2000) 231.

[15] Ralph TR, Hitchman M, Millington J and Walsh FC, Mass transport in an Electrochemical Laboratory Filterpress Reactor and its Enhancement by Turbulence Promoters, Electrochim. Acta, 41(1996) 591.

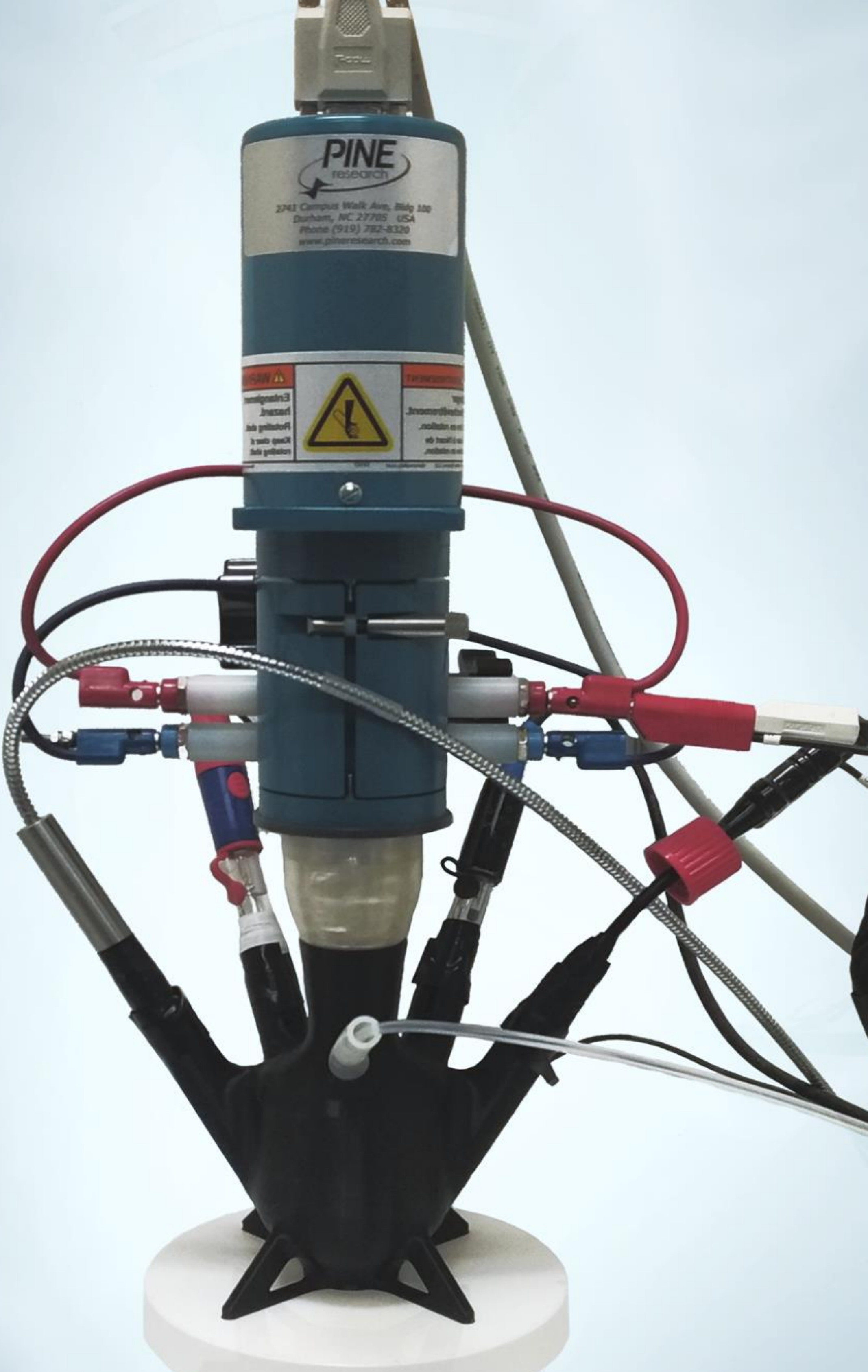
PINE
research
2741 Campus Walk Ave, Bldg 100
Durham, NC 27705 USA
Phone (919) 782-8320
www.pineresearch.com

A comparative study of the stability of hexachloroiridate and hexacyanoferrate in electrochemical mass transfer measurements

S.J.C. Weusten, M.T. de Groot, J. van der Schaaf

2 - Abstract

Hexacyanoferrate(II)/hexacyanoferrate(III) is a commonly used redox couple for measuring the mass transfer performance of electrochemical reactors. However, this redox couple can irreversibly poison the electrode, potentially leading to unreliable results. There are alternatives such as the hexachloroiridate(IV)/hexachloroiridate(III), but relatively little is known about their stability. Therefore, we have investigated the stability of the hexachloroiridate redox couple and compared this to the stability of the hexacyanoferrate couple. Voltammetry confirms that the hexachloroiridate couple is reversible, with a clear limiting current density plateau for the reduction on both platinum and nickel. Diffusion coefficients for hexachloroiridate(IV) and hexachloroiridate(III) were determined to be respectively $8.38*10^{-10}$ m^2/s and $6.10*10^{-10}$ m^2/s. Chronoamperometric limiting current density experiments of 16 hours at pH 4 show that the electrode is not poisoned. However, as evidenced by inline UV-VIS measurements the bulk concentration of hexachloroiridate(IV) decreases, which is probably due to a spontaneous reduction or hydroxylation reaction. UV-VIS measurements of iridate solutions show that in more acidic solutions (pH 2-3) the degradation occurs more slowly, whereas at pH>6 rapid hydroxylation of the complex occurs, making the couple unsuitable for mass transfer experiments at high pH. Experiments with hexayanoferrate show that that couple is more stable in solution, but that irreversible electrode poisoning cannot be avoided. Therefore, the hexachloroiridate couple seems especially suitable for testing electrode materials that are difficult to clean, such as three dimensional structures.

Image: the rotating disk electrode used in this work

2.1. Introduction

An important characteristic in the design of electrochemical reactors is the mass transfer performance. By using what is known as the limiting current density method, it is possible to determine the mass transfer performance of a given reactor experimentally.[1] From such experiments, Sherwood-Reynolds correlations can be established in order to compare the performance of different reactors and their specific configurations.

A reversible redox couple such as hexacyanoferrate(III)/ hexacyanoferrate(II) is typically used to determine the limiting current density.[2,3] However, care must be taken with regard to the experimental conditions to avoid relatively large measurement errors. Sources for these errors include surface oxides, dissolved oxygen, and the roughness of the surface. Of particular concern is the fact that over time the observed limiting current may decrease due to irreversible electrode poisoning.[4-8] The cause for this is the deposition of an insoluble species onto the electrodes, which forms an additional barrier to the flow of current. Measurements using Auger and infrared spectroscopy have suggested that these insoluble species are products such as $Fe(CN)_{3(s)}$ or perhaps $Fe_2O_{3(s)}$,. Prussian blue was suspected to be one of the species[9], but there is evidence that this is not the case.[5-6,10-11]

The formation of the passivating layer is irreversible, meaning that its removal requires abrasive polishing.[12] Typically, this is done by using a descending series of fine grains of alumina combined with different types of felt pads.[12] Since this process is time-intensive, several strategies have been proposed to alleviate the passivation problem. Szánto et al. have investigated the effect of experimental conditions on the passivation and have proposed a rigorous pretreatment procedure.[12] They also suggest to change the supporting electrolyte, since the poisoning effect is significantly diminished by using for instance K_2CO_3 or KNO_3 instead of KOH.[8,12]

For flat plate electrodes the polishing is relatively straightforward. However, many electrochemical processes make use of more intricate three-dimensional electrodes.[13] Adequately polishing such electrodes is difficult, if not impossible. The result is that once the electrode becomes passivated, it will have to be discarded as it cannot be cleaned by polishing.

Because of the difficulties encountered with the hexacyanoferrate redox couple, literature studies occasionally use other redox couples such as hexachlororiridate, hexaammineruthenium and ferrocenemethanol.[14-17] In the case of hexachloroiridate, Petrovic et al. already suggested that the stability of this couple during storage is superior to that of hexacyanoferrate.[18] Here we expand on their work and compare the stability of the hexachloroiridate redox couple to that of the traditionally used hexacyanoferrate redox couple during typical mass transfer measurements. For this purpose the limiting current is tracked during continuous overnight reduction for both systems and compared. Inline UV-VIS spectroscopy is used to track the change of bulk concentration throughout these experiments to be able to discern the difference between a decrease in solution concentration and electrode poisoning. These experiments are performed in both the well-described environment of the rotating disc electrode, and a typical parallel plate electrolyzer. Finally, the effect of pH on the stability of the hexachloroiridate couple is investigated.

2.2. Materials and methods

Two setups were used in this work. For most experiments, a high-speed (0-7000 RPM) rotating disc electrode (RDE) setup (Pine instruments) was used. For long-term stability measurements a custom-built 3D printed parallel plate electrolyzer was used. In either case, electrochemical measurements were performed using an Ivium Compactstat and the associated Ivium software.

Experiments with the RDE were carried out with a 0.196 cm^2 platinum or nickel working electrode. A specially designed 3D printed 100 mL black polylactic acid (PLA) reactor vessel was used to prevent interference from light. Moreover, this vessel was kept under a nitrogen atmosphere to prevent influence from atmospheric oxygen. A platinum counter electrode and an Ag/AgCl (3.0 M KCl) reference electrode were used. All potentials in this paper are listed with respect to SHE, which means that the measured potentials were shifted by 0.210 V. The setup was equipped with a Consort pH probe and a stainless steel UV-VIS variable path dip probe (Avantes).

The 3D printed parallel plate electrolyzer setup consisted of a storage vessel from which the electrolyte was pumped (Tuthill D-type gear pump) into the electrolyzer at a constant flow rate of 40 L/h. The Ag/AgCl (3.0M KCl) reference electrode was placed in the storage vessel. A 5 mm path length inline UV-VIS flow cell (Avantes) was used to track the concentration of either hexachloroiridate(IV) or hexacyanoferrate(III). The electrolyzer itself was designed in-house and printed by the 3D printing company ZiggZagg using selective laser sintering of nylon powder. The electrodes were 4 cm (width) x 10 cm (length) nickel plates and were mounted parallel to each other with a gap distance of 5 mm. More details on the printed reactor are available elsewhere.[19]

Prior to all experiments the working electrode (WE) was pretreated in accordance to the recommendations of Szánto et al.[12] :

1. The WE was carefully polished using a series of fine-grain alumina suspensions in decreasing order (from 1.0 micron to 0.3 micron to 0.05 micron).
2. The WE was then submerged in >15.0 MΩcm demineralized water and sonicated twice for 15 minutes. The water was refreshed between the first and the second sonification.
3. The WE was then activated by evolving hydrogen on its surface for 10 min at a current density of 10 mA cm^{-2} in 1.0M KOH.

Two types of electrolyte solutions were used: one containing hexacyanoferrate, the other containing hexachloroiridate. Table 1a and 1b list the compounds used in each. The compounds were analytical reagent grade chemicals obtained from VWR, except for hexachloroiridate(IV) and hexachloroiridate(III), which were obtained from Merck/Sigma Aldrich (>99.99% pure. trace metals basis). The water content of both iridate compounds was verified to be negligible through thermogravimetric analysis (no weight loss observed after 60 minutes at 180°C in N_2 atmosphere). The chemicals for the iodometric titrations - Potassium iodide (powder, >99%) and sodium thiosulphate (0.1N standard solution) - were obtained from VWR.

Table 1a: The hexacyanoferrate electrolyte solution used in this work

Role	Compound	Formula	Concentration
Reductant	Potassium Hexacyanoferrate(II)	$K_4Fe(CN)_6$	0.5 mM
Oxidant	Potassium Hexacyanoferrate(III)	$K_3Fe(CN)_6$	0.5 mM
Supporting	Potassium Nitrate	KNO_3	0.5 M
Buffer	None		

Table 1b: The hexachloroiridate electrolyte solution used in this work

Role	Compound	Formula	Concentration
Reductant	Potassium Hexachloroiridate(III)	K_3IrCl_6	0.5 mM
Oxidant	Potassium Hexachloroiridate(IV)	K_2IrCl_6	0.5 mM
Supporting	Potassium Nitrate	KNO_3	0.5 M
Buffer	Potassium Acetate Acetic Acid	CH_3COOK CH_3COOH	0.1 M total at pH 4

The electrolyte solutions were prepared by dissolving the oxidant/reductant separately from the supporting electrolyte and buffer. The reason for this was that we experienced minor difficulties in dissolving the hexachloroiridate compounds in the same flask in a reasonable amount of time. The full procedure was as follows:

(1) A blank stock solution containing only the supporting electrolyte and buffer (if applicable) was prepared at twice the desired concentration (i.e. 1.0 M KNO_3 and 0.2M buffer solution for hexachloroiridate experiments).

(2) A fresh solution of 1.0mM of both the reductant and oxidant were prepared in 100 mL of deionized (>15 MΩ) water

(3) The 100 mL oxidant/reductor solution was diluted with 100 mL of blank stock solution, resulting in 200 mL of electrolyte solution with the concentrations listed in table 1a or 1b.

At the start of each experiment the black PLA reactor vessel (RDE setup), or storage vessel (Electrolyzer setup) was filled with blank reference solution in order to set a baseline for the UV-VIS probe. To create a blank reference solution, 100 mL of the blank stock solution was diluted with 100 mL of deionized water. Thereafter, the vessel was emptied, pre-rinsed and filled with the electrolyte solution.

UV-VIS measurements were performed both inline and offline. The inline flow cell or probe was used in connection with an Avantes tungsten lamp and Avaspec spectrometer. For the offline measurements a Shimadzu UV2501(PC) spectrometer was used. To ensure that the dip probe was set to the correct path length, a 0.1mM methylblue solution was measured and compared to ex-situ measurements and the literature values.[20] Ex-situ absorbance measurements were used to determine the initial bulk concentration of hexachloroiridate(IV), in-situ measurements were used to continuously track the bulk concentration once the experiment was started. The hexachloroiridate(III) concentration could not be measured by UV-VIS, since its peaks are obscured by the hexachloroiridate(IV) spectrum (see figure 8). For the few hexachloroiridate(III) oxidation experiments, the concentration was estimated to be equal to the dissolved amount of hexachloroiridate(III) combined with the observed loss of hexachloroiridate(IV). This assumes that part of the hexachloroiridate(IV) spontaneously converts into hexachloroiridate(III) upon dissolution. Typically, around 10% of hexachloroiridate(IV) was converted this way (see 3.4 on the stability of hexachloroiridate(IV)).

The extinction coefficients for hexachloroiridate(IV) were determined using the offline spectrometer and verified using a biamperometric iodometric titration as specified in the work of Lichtig [21] (also mentioned in Wöhler et al.[22]).The endpoint in this iodometric titration is determined by a dead stop in the current (zero current). Here we used an Ivium compactstat and two 5 cm^2 platinum foils as the electrodes. A potential of 30 mV was applied between both electrodes. Two sets of 10 solutions of hexachloroiridate(IV) with concentrations varying between 0.05 and 0.9 mM were prepared for the calibration curve. The first set was dissolved in 0.1M HCl, the second in pure water. This was done in order to rule out effects of the pH because of the spontaneous reduction reaction. The extinction coefficient of hexachloroiridate(IV) at 488nm was found to be 4.06 $mM^{-1}cm^{-1}$ for both sets. More results are summarized in table B1 in the supporting info. Extinction coefficients for hexachloroiridate(III), hexacyanoferrate(II), and hexacyanoferrate(III) were obtained without verification by means of iodometric titration and are also found in table B1. Spectra for each of these compounds are given in figures B1 and B2.

In the 16h stability experiments the limiting current density was normalized with respect to either the starting concentration or the actual concentration. In the former case, the limiting current was divided by the initial bulk concentration of the oxidant for all data points measured using that solution, i.e. $I_A/\mathrm{C}_{\mathrm{t=0}}$. In the latter case, the limiting current density was normalized with respect to the bulk concentration at the moment of measurement for each specific data point, i.e. $I_A/\mathrm{C}_{\mathrm{t}}$. These values are then further normalized by the diffusion coefficient of the oxidant (either hexachloroiridate(IV) or hexacyanoferrate(III) to the power 2/3, i.e. $D_{ox}^{2/3}$.

2.3. Results and discussion

2.3.1. Cyclic voltammetry

In figure 1 the cyclic voltammetry of a hexachloroiridate solution is shown for different scan rates. Reduction and oxidation peaks can be seen around the formal reduction potential of +0.8665 $V_{/SHE}$.[23] The corresponding reaction is as follows:

$$\mathrm{IrCl_6^{3-}} \rightleftharpoons \mathrm{IrCl_6^{2-}} + \mathrm{e^-}$$

The reaction is reversible as evidenced by the small peak separation (~70 mV) and lack of peak shift with increased scan rate. The potential window between the hydrogen (HER) and oxygen evolution reaction (OER) (figure 2) of the electrolyte solution extends from -0.2 $V_{/SHE}$ to 1.2 $V_{/SHE}$ and contains no side reactions except for those typical for platinum electrodes: the reduction peak at 0.37 $V_{/SHE}$ is the result of the reduction of platinum oxides, the formation of which (between 1.0 $V_{/SHE}$ to 1.2 $V_{/SHE}$) is nearly invisible as a result of its proximity to the hexachloroiridate(III) oxidation and the oxygen evolution reaction (OER).[24]

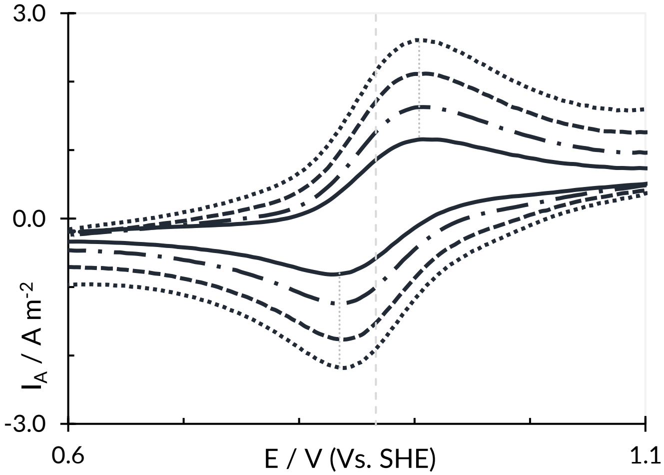

Figure 1: Cyclic voltammogram of 0.5 mM/0.5mM Hexachloroiridate(IV)/ hexachloroiridate(III) in a pH 4 0.1M acetate buffered, 0.5M KNO3 solution on platinum at 20 (full line), 40 (dash-dotted), 60 (small dashes) and 80 (dotted) mV/s. Measured using the platinum RDE and platinum counter electrode at zero rotation.

In comparison for hexacyanoferrate the redox peaks are found close to +0.358 V/SHE in accordance with literature values.[4,23] The hexacyanoferrate redox couple is as follows:

$$\mathrm{Fe(CN)_6^{4-} \rightleftharpoons Fe(CN)_6^{3-} + e^-}$$

The potential window between HER and OER of the hexacyanoferrate solution extends from -0.65 V/SHE to 1.3 V/SHE, which is larger than for hexachloroiridate. This is a result of the difference in pH of both electrolyte solutions (9.4 for ferrate and 4.0 for iridate): the OER shifts by a smaller potential than the HER with changing pH. This is related to the fact that platinum is a better oxygen evolution catalyst in acidic media than in alkaline media, which in turn relates to the presence of a platinum oxide film.[25-26]

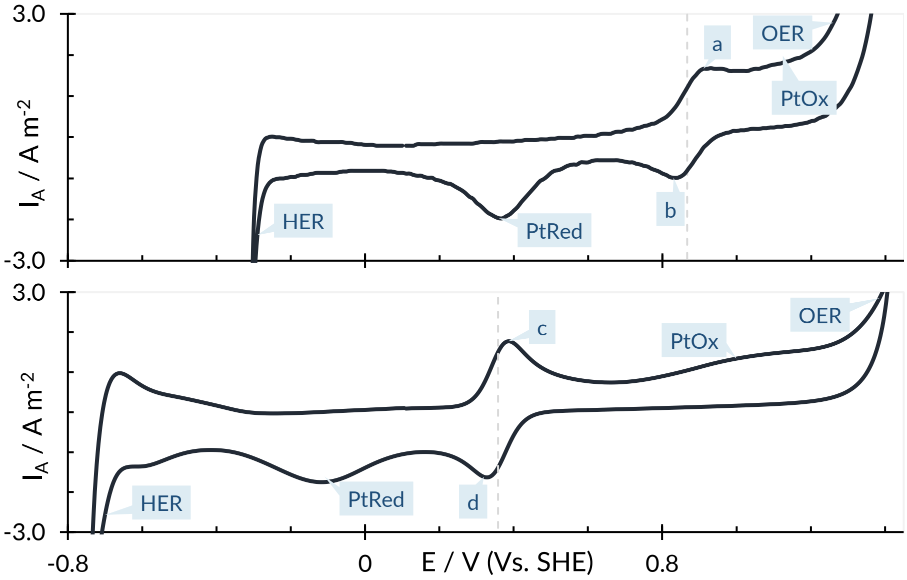

Figure 2: Cyclic voltammogram on platinum at 40 mV/s. Top: 0.5 mM hexachloroiridate(IV) and 0.5 mM hexachloroiridate(III) in pH4 0.1M acetate buffered 0.5M KNO3 solution, bottom: 0.5 mM/0.5mM hexacyanoferrate(III)/hexacyanoferrate(III) in ~pH 9.4 unbuffered 0.5M KNO3 solution. HER: Hydrogen evolution reaction, OER: oxygen evolution reaction, PtRed: Platinum oxide reduction, PtOx platinum oxidation, a: hexachloriridate(III) oxidation, b: hexachloroiridate(IV) reduction, c: hexacyanoferrate(II) oxidation, d: hexacyanoferrate(III) reduction.

The behavior of the hexachloroiridate couple on a glassy carbon or nickel electrode is similar to that on platinum (figure A.1), which shows that the couple is not influenced by the electrode materials shown here. A larger potential window (-0.4 $V_{/SHE}$ to 1.3 $V_{/SHE}$) exists for nickel electrodes, because the water splitting reactions (HER/OER) occur at higher overpotentials. Peaks related to the corrosion of nickel were not observed, because the thin protective oxide layer on the surface of the nickel electrode is sufficiently stable at pH 4 [27].

2.3.2. The limiting current density plateau

For electrochemical mass transfer measurements, the limiting current density plateau should ideally be free from interference by side reactions. Concretely, this means that we wish to see a wide flat plateau. Linear sweep voltammograms of the hexachloroiridate and hexacyanoferrate solutions (figure 3) show that a flat plateau is present for the two solutions during both oxidation and reduction. The hexachloroiridate(IV) reduction plateau extends from around 0.75 $V_{/SHE}$ to -0.25 $V_{/SHE}$ and is about 0.2 V larger than the hexacyanoferrate(III) reduction plateau that extends from 0.2 $V_{/SHE}$ to -0.6 $V_{/SHE}$. The reason for this is the higher reduction potential of the hexachloroiridate ion. However, the effect is partly offset by the more acidic pH and hence higher hydrogen evolution potential of the hexachloroiridate solution. For the oxidation reactions the difference is larger: only a small plateau for the hexachloroiridate(III) oxidation is found (0.95 $V_{/SHE}$ to 1.1 $V_{/SHE}$) compared to that of hexacyanoferrate(II) (0.5 $V_{/SHE}$ to 1.1 $V_{/SHE}$). The combined plateaus of hexacyanoferrate are larger than those of hexachloroiridate due to the larger potential window between HER and OER.

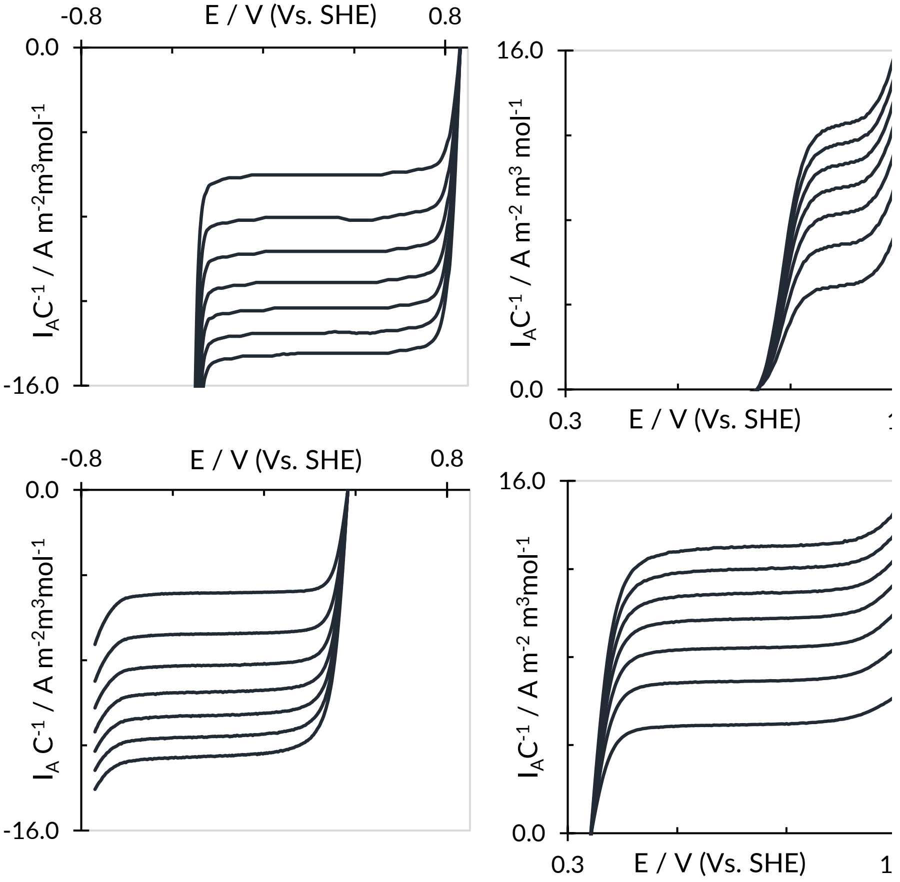

Figure 3: Linear sweep voltammograms at 10 mV/s. Top left: reduction of hexachloroiridate(IV), top right: oxidation of hexachloroiridate(III), bottom left: reduction of hexacyanoferrate(III), bottom right: oxidation of hexacyanoferrate(II). The rotation rate was varied between 1000 RPM and 7000 RPM in steps of 1000 RPM. The limiting current was corrected for the actual concentration of the oxidant species as tracked by the inline UV-VIS. The concentrations and compositions of the hexacyanoferrate and hexachloroiridate solutions are listed in table 1a and table 1b respectively

The limiting current density plateau for hexachloroiridate reduction on nickel is similar (figure A.2). It extends from 0.7 $V_{/SHE}$ to -0.35 $V_{/SHE}$ and is therefore longer than on platinum (0.75 $V_{/SHE}$ to – 0.25 $V_{/SHE}$) due to the fact that the hydrogen evolution starts at a lower potential.

Without nitrogen flushing, oxygen will be present in the solution, which then leads to an oxygen reduction plateau on top of the existing plateau. In figure 4 this effect is shown. Since the hexachloroiridate reduction occurs at a higher potential, one might expect that a larger part of its plateau will remain unaffected by the oxygen reduction. This is not the case because the lower pH of the hexachloroiridate solution shifts the oxygen reduction to higher potentials. Overall, the reduction plateau for hexachloroiridate is shrunk from a width of 1.0 V to 0.35 V. In the hexacyanoferrate solution, the width is decreased from 0.8 V to 0.3 V. Given the fact that the remaining plateau is still sufficiently long, it can be concluded that nitrogen flushing is not strictly necessary for measurements relatively close to the equilibrium potential.

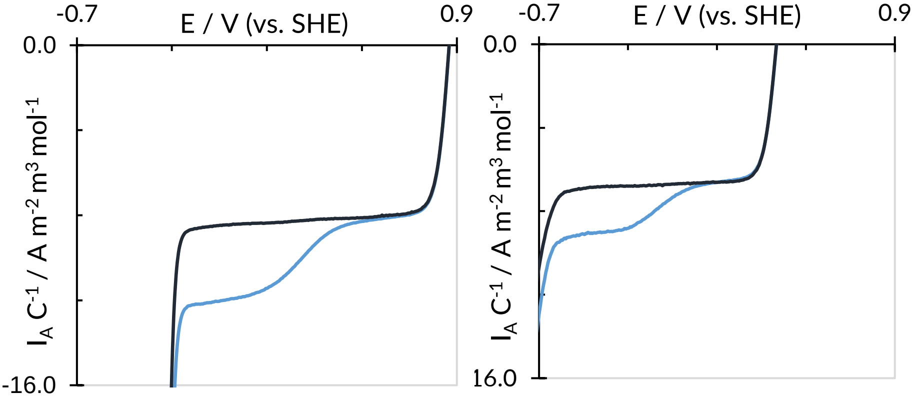

Figure 4: Linear sweep voltammogram at 10 mV/s and 2000 RPM. Blue line: before nitrogen flushing, Black line, after nitrogen flushing. Left: hexachloroiridate(IV) reduction, right: hexacyanoferrate(III) reduction. The concentrations and compositions of the hexacyanoferrate and hexachloroiridate solutions are listed in table 1a and table 1b respectively.

2.3.3. The diffusion coefficient and mass transfer

The diffusion coefficients of the oxidant and the reductant were determined for both redox couples. The results are shown in figure 5 and table 2. Values comparable to those in literature were found in this work. The diffusion coefficient of hexachloroiridate(III) (the reductant) appears to be lower than of hexachloroiridate(IV) (the oxidant). For hexacyanoferrate on the other hand, the diffusion coefficient of the oxidant is higher than that of the reductant. The reason for this behavior is unclear.

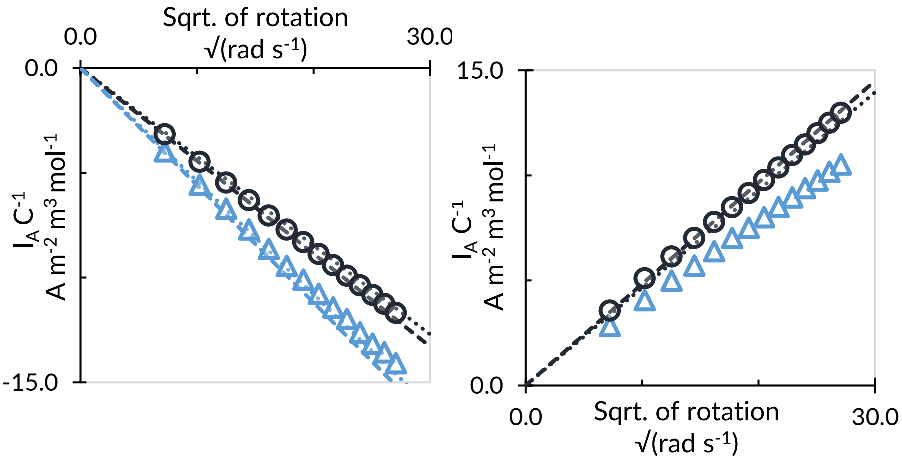

Figure 5: Levich plots of hexacyanoferrate and hexachloroiridate. Left: the oxidant species (Dox), right: the reductant species (Dred). Black circles: hexacyanoferrate (experimentally determined in this work), black dotted line: expected levich plot based on literature values [28,29], black dashed line: expected plot based on reference [30]. Blue triangles: Hexachloroiridate (this work), blue dotted line: expected levich plot based on reference [18], blue dashed line: plot based on reference [31]. The concentrations and compositions of the hexacyanoferrate and hexachloroiridate solutions are listed in table 1a and table 1b respectively.

Table 2: Selected diffusion coefficients from literature in comparison to this work.

Redox Couple	Medium	D_{ox} 10^{-10} m^2 s^{-1}	D_{red} 10^{-10} m^2 s^{-1}	Reference
Hexacyanoferrate	1.0 M KCl	5.88	6.77	[28, 29]
Hexacyanoferrate	0.5 M NaOH	6.29	7.17	[30]
Hexacyanoferrate	0.5 M KNO_3	6.09	7.09	This work
Hexachloroiridate	0.1 M KNO_3	8.93	//	[18]
Hexachloroiridate	0.5 M KNO_3	8.46	//	[31]
Hexachloroiridate	0.5 M KNO_3 0.1 M Acetate	8.38	6.10‡	This work

D_{ox} refers to the diffusion coefficient of the oxidant (hexachloroiridate(IV) or hexacyanoferrate(III), D_{red} refers to that of the reductant (hexachloroiridate(III) or hexacyanoferrate(II)). ‡: Note: The actual concentration of hexachloroiridate(III) was not measured directly using UV-VIS, it was estimated based on the amount dissolved and the loss of concentration of hexachloroiridate(IV) (see 2.2.2).

The stability of the limiting current density plateaus of hexachloroiridate(IV) and hexacyanoferrate(III) was investigated using a platinum RDE (see figure 6a and 6b). It can be seen that the limiting current density (normalized by start concentration) for reduction of both species drops over time. After 16 h a current loss of 39.2% is observed for hexachloroiridate(IV) and 19.5% for hexacyanoferrate(III). If the sytems would be fully reversible this should not happen, as the reduced oxidant species should be re-oxidized at the counter electrode and hence the concentration should not change. Therefore, either electrode passivation or some form of degradation of the reacting species occurs.

Refreshing the solution after 16 hours leads to almost complete restoration of the current to the initial value for hexachloroiridate(IV), but not for hexacyanoferrate(III). The current (normalized by starting concentration) is restored to 99.6 % of the initial value for hexachloroiridate(IV) and 93.0 % for hexacyanoferrate (III). This means that the observed decrease in current for hexachloroiridate is almost entirely due to a decreasing concentration, whereas for hexacyanoferrate electrode poisoning seems to be a significant factor. Similar experiences have been reported for hexacyanoferrate in literature by a.o. Szanto et al.[8,12] However, compared to the work of Szánto et al. our decrease in current is slightly faster. We find a loss of 3.9% after 2 hours, compared to a loss of 2.5% after 2 hours in similar conditions.[12] A key difference between both works is that we used a UV-VIS probe that continuously emitted light into the dark vessel. Since the presence of light can affect the stability of this species,[32] it is likely that the higher loss of current is a result of the probe's light emissions.[12]

In essence it appears that for ferrate optimizing the reaction conditions can slow the poisoning process, but cannot stop it completely. Therefore, a small but ever-increasing error will grow and persist through the measurements until the electrode is abrasively polished. Indeed this is shown in the figure 6b, where we account for the actual bulk concentration losses. Here the hexachloroiridate(IV) current remains stable, whereas the current of hexacyanoferrate(III) weakens over time at a rate of about 0.031 $A/m^{2}*m^{3}/mol/h$. Between the final (t=16 h, before refresh) and initial values (t=0 h), a deviation of 7 % is seen for hexacyanoferrate, and a deviation of <1% for hexachloroiridate. Similar results were obtained for nickel electrodes (figure A3).

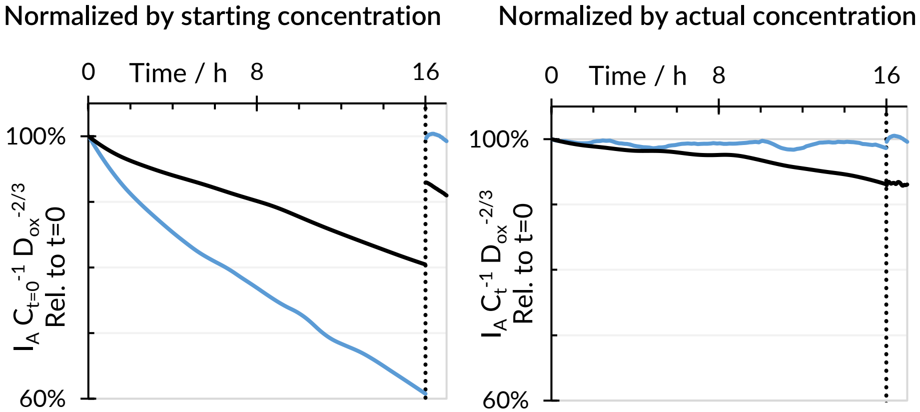

Normalized by starting concentration

Normalized by actual concentration

Figures 6a(on the left) and 6b(on the right): The limiting current density at 2000 RPM of the reduction of hexachloroiridate(IV) in blue and hexacyanoferrate(III) in black. At 16 hours, the solution was refreshed. The composition of the hexacyanoferrate and hexachloroiridate solutions are listed in table 1a and 1b respectively. A platinum RDE was used. Figure 6a is normalized by the initial concentration of the oxidant species as determined by ex-situ UV-VIS measurement. In figure 6b, the current density is normalized by the concentration the moment it was measured using the UV-VIS dip probe.

The rotating disc electrode has a well-described hydrodynamic flow pattern, which can be solved analytically. For other electrolyzers this is rarely the case, which means we rely on empirical Sherwood-Reynolds correlations. It is therefore important to demonstrate the stability of the redox couple in a typical electrolyzer, so that it can be ascertained that reliable correlations can be obtained.

In figure 7a and 7b, we explore how the limiting current densities of hexacyanoferrate and hexachloroiridate change in 16 h in a parallel plate electrolyzer. For the hexachloroiridate(IV) reduction current a loss of 76.6 % is seen in only two hours at pH 4 as opposed to a loss of 15.1 % for the hexacyanoferrate(III) current. At the end of the 16 hour period, the hexachloroiridate solution had a faint yellow color, with a UV-VIS spectrum similar to that of hexachloroiridate(III). After refreshing, the hexachloroiridate current is restored to 97.6% of its original value, whereas the hexacyanoferrate current is only restored to 89.9%.

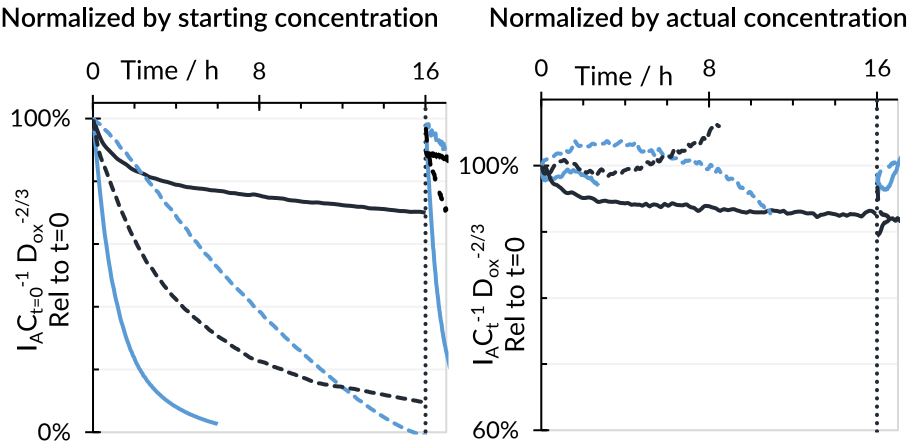

Figure 7a (on the left) and 7b (on the right): The limiting current density of 0.5mM/0.5mM hexacyanoferrate(III)/(II) and 0.5mM/0.5mM hexachloroiridate(IV)/(III) at 40 l/h flowrate through a 3D printed parallel plate electrolyzer with 40 cm2 nickel electrodes in 0.5 M KNO_3*. After 16 hours, the solution is refreshed. Full black line: hexacyanoferrate in 0.5M KNO3 (unbuffered); dashed black line: hexacyanoferrate in 0.5M KOH, full blue line: hexachloroiridate in 0.1M pH 4 acetate buffer, dashed blue line: hexachloroiridate in 0.1M pH 2 phosphate buffer. In figure 7a (left) the current density is normalized by the initial concentration, in figure 7b (right) it is normalized by the actual concentration. In the latter case, the graph ends when the absorbance reaches a value of 0.10. The concentration data over time is shown in figure A.4.*

Using hexachloroiridate at pH 2 instead of pH 4 results in a much smaller loss of current of only 14.3 % after 2 hours. Therefore, the pH is of significant importance to the stability of the hexachloroiridate complex (see also figure A.5). When using hexacyanoferrate, it is known from literature that an alkaline supporting electrolyte such as KOH significantly worsens the stability[8,12] and this is also observed here (the current loss is 38.4% after 2 hours for hexacyanoferrate in KOH). In either case the current is restored to similar values after refreshing, therefore showing a similar degree of poisoning. In figure A.6 the characteristic yellowing of the electrodes as a result of the hexacyanoferrate poisoning can be seen. Figure 7b shows a graph of the limiting current density normalized by actual concentration. This graph is relatively noisy as a result of noisy data of the current. Despite this, some general trends can be inferred. For all solutions, the current density remains relatively stable. The pH 2 solution of hexachloroiridate remains useable (peak absorbance > 0.1) up to approximately 14 hours, the hexacyanoferrate in KNO_3 for the entire 16 hours. Moreover, it is clear that a solution of higher pH shortens the lifetime of hexachloroiridate (to about 3 hours). The hexachloroiridate current is restored to the initial value.

Comparing figure 6 and 7 shows that both redox couples seem to degrade faster when used in the parallel plate electrolyzer compared to the RDE. One explanation is the larger surface area of the electrodes compared to the volume of electrolyte (200 cm^2/L solution in the parallel plate setup vs. 0.98 cm^2/L solution in the RDE). Another reason is that we used glass vessels and translucent plastic tubing. Despite running the experiments mostly during the night, this resulted in more ambient light exposure for the electrolyte, as the environment was never completely dark. Finally, it is more difficult to completely clean and mirror polish a 40 cm^2 flat plate compared to a 0.196 cm^2 RDE. Therefore, small contaminants could be present that accelerate the degradation of either redox couple. The same is true for cleaning the setup in general due to its larger scale. All in all, these conditions lead to a decreased stability of the reduction plateaus.

Though both couples are affected to some extent, it is more severe for hexachloroiridate. A possible explanation could be that hexachloroiridate predominantly suffers from side reactions on the electrode during the redox process (see 3.4 On the stability of hexachloroiridate(IV)), whereas hexacyanoferrate is mostly affected by the ambient conditions (specifically light). This is because we expect the former effect to be exacerbated more due to the factor 200 difference in the area-volume ratio of the setups. The effect of light on the other hand would be smaller because the difference in light levels between both setups was not that large, especially when considering that the experiments were performed overnight.

2.3.4. On the stability of hexachloroiridate(IV)

Spectral data (figure 8) were taken in order to evaluate the causes behind the degradation of the hexachloroiridate redox couple, specifically with respect to the pH. It is clear that the pH has a strong effect on the stability of the hexachloroiridate(IV) complex. In acidic media (pH <5) the spectrum closely resembles the hexachloroiridate(IV) spectrum reported in literature.[33-34] However, a slightly decreasing intensity of the 488 nm absorption is observed when the pH is increased from pH 2 to pH 4. As the pH is further increased, a strong loss of the 488 nm absorbance starts occurring. At a weakly acidic pH (5-6) the hexachloroiridate(IV) peaks are still identifiable, though less intense. Above pH 7 the characteristic peak at 488 nm disappears entirely, with more absorbance appearing in the 360-390 nm region. At pH 10 and pH 11 the solution loses its brown color and becomes faintly blue instead. Moreover, a small amount of dark precipitate is formed.

Several reactions are known in literature that could explain the loss of bulk hexachloroiridate(IV) in aqueous media:

(1) Substitution of one chloride ligand with water: aquation of the complex [35-36]

$$IrCl_6^{2-} + H_2O \rightleftarrows Ir(H_2O)Cl_5^{-} + Cl^{-}$$

(2) Auto-reduction of hexachloroiridate(IV) to hexachloroiridate(III) through oxidation of the surrounding water [34-36]

$$4IrCl_6^{2-} + 2H_2O \rightleftarrows 4IrCl_6^{3-} + 4H^{+} + O_2$$

(3) Hydroxylation of the hexachloroiridate complex followed by precipitation of $Ir(OH)_6^{2-}$ and formation of IrO_2.[22, 33, 36-39]

$$IrCl_6^{2-} + 6OH^{-} \rightleftarrows Ir(OH)_6^{2-} + 6Cl^{-}$$
$$Ir(OH)_6^{2-} \rightarrow IrO_2.2H_2O + 2OH^{-}$$

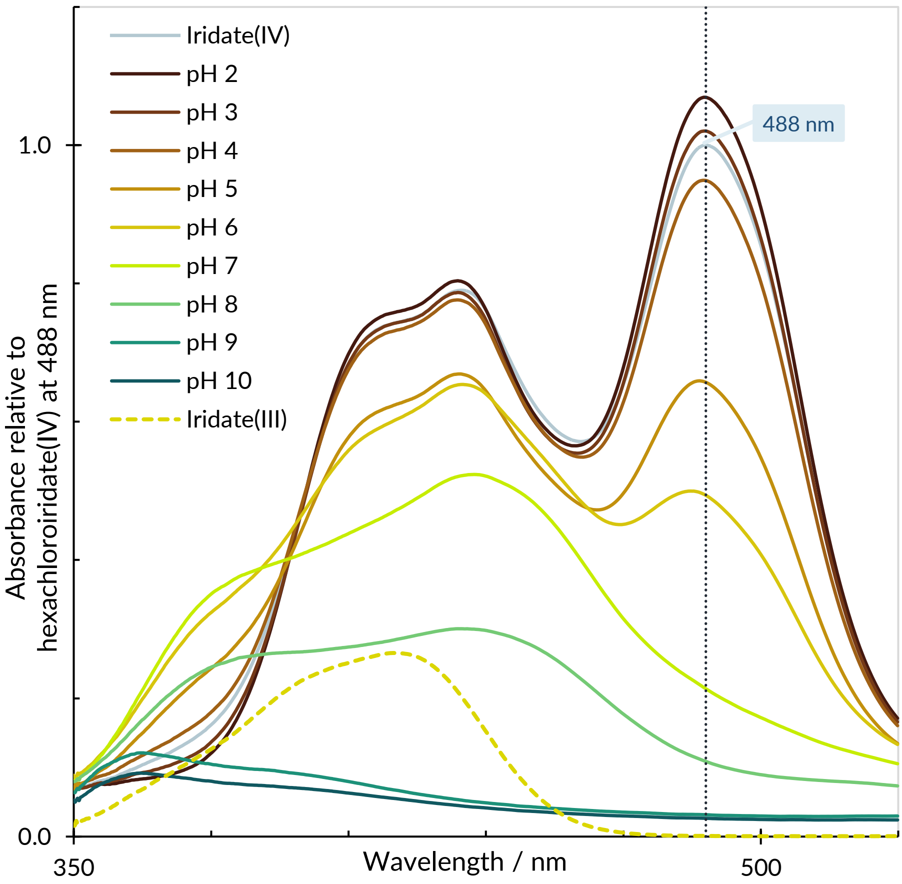

Figure 8: The effect of pH on the concentration of hexachloroiridate(IV) as measured by UV-VIS spectroscopy. The absorbance is normalized relative to the 488 nm peak of 0.5mM hexachloroiridate (IV) in pure water. The spectrum of this unbuffered 0.5mM hexachloroiridate solution is denoted as "Reference". The color of the line approximates the color of the solution -except for the reference solution which is shown as a gray dashed line. Spectra for specific pH values were obtained from solutions of 0.5 mM hexachloroiridate(IV) in the presence of either a 0.1M phosphate buffer (pH 2-3 and pH 6-9) , 0.1M acetate buffer (pH 4-5), or 0.1M bicarbonate buffer (pH 10). The solution was left stirring for 15 minutes after the addition of hexachloroiridate(IV) before taking the spectra.

The first possible reaction is an aquation reaction. From the work of Poulsen and Garner it is known that aquopentachloroiridate(IV) strongly absorbs light around 450 nm and therefore forms dark reddish-orange solutions.[34] Though this is a small change from the dark brown hexachloroiridate(IV) solution, it should be easily identifiable through the UV-VIS spectrum. In figure 8 there are no strong 450 nm peaks, indicating that aquopentachloroiridate(IV) is not significantly present. The same is true for the spent solution of the 16 hour reduction experiment, which was faintly yellow and did not show 450 nm peaks either. However, these observations do not exclude the possibility of hexachloroiridate(III) undergoing aquation. This is because the UV-VIS spectra of both hexachloroiridate(III) and aquopentachloroiridate(III) are similar.[34] In the work of S. Petrovic, a solution of hexachloroiridate(IV)/(III) was left under ambient conditions for six weeks.[18] Cyclic voltammetry of this solution showed an additional reversible redox wave close to that of the hexachloroiridate couple. This wave was suspected to be due to the aquopentachloroiridate(III)/(IV) complex. In our experiments, cyclic voltammograms of the aged solutions did not show this additional wave. As a result, it seems unlikely that neither hexachloroiridate(III) nor hexachloroiridate(IV) underwent aquation.

The second reaction is the spontaneous reduction of hexachloroiridate. This phenomenon is investigated more deeply in the works of Dwight A. Fine,[36] and Peixoto Cabral et al.[40] Both suggest that the reduction is accompanied by water oxidation and not by the oxidation of ligand chloride. Since this reaction forms hexachloroiridate(III), the solution is expected to turn to faint yellow. This is indeed what we observe, which suggests that the auto-reduction reaction is occurring. Furthermore, the reaction is pH dependent, which matches our observations in figures 7 and 8 [36]. However, it should be noted that at pH > 5, a different reaction occurs since the spontaneous reduction cannot explain the appearance of absorption peaks in the 360-390 nm range and the 430-450nm range.

The third possible reaction is the hydroxylation of the hexachloroiridate complex. This reaction is well-known in electrocatalysis as it allows the creation of thin films or nanoparticles of highly active iridium dioxide catalyst for O_2 evolution. [38-39] At the end of the process, the solution turns from brown (characteristic of hexachloroiridate(IV) to blue (indicating the iridium oxide particles).[33,38-39] Similar to the spontaneous reduction, the hydroxylation reaction is dependent on the pH. However, more alkaline conditions are required for the hydroxylation reaction. In the synthesis of the iridium oxide catalysts for instance, a pH value above 11 or 12 is typically used.[38-39] The appearance of absorbance peaks in the 360-390 nm and consequently the color shift to faint blue are indicative of the hydroxylation reaction. Therefore it is reasonable to assume that the spectrum at pH 9 and pH 10 is that of the iridium oxide particles formed in the hydroxylation reaction. At a pH of 6-8 a spectrum is seen that is distinct from the spectra of the other pH regions. Its most pronounced feature is the peak around 340 nm. It is unknown which compound or combination thereof this represents, though it is likely an intermediate in the hydroxylation process. In general, the hydroxylation reaction results in noticeable degradation of the hexachloroiridate(IV) complex at a pH of 6 and above.

It is clear that the stability of the hexachloroiridate(IV) complex is heavily dependent on the pH: the more acidic, the slower the degradation. In acidic solutions the spontaneous reduction is the main path for degradation, resulting in the formation of hexachloroiridate(III). It is likely that the spontaneous reduction can be reversed in strongly acidic solution, though we did not test this.

2.4. Conclusion

In this work hexachloroiridate was compared to hexacyanoferrate with a special focus on the stability of both couples. In contrast to hexacyanoferrate no electrode poisoning was observed for hexachloroiridate during overnight measurements of the limiting current density.

For 3D electrodes the poisoning effect is especially troublesome as they cannot easily be polished. Hexachloroiridate does not have this problem and is therefore more suitable for these electrodes. However, hexachloroiridate(IV) degrades faster than hexacyanoferrate(III), which means that the electrolyte solution must be frequently refreshed. Due to the relative high price of hexachloroiridate compared to hexacyanoferrate, this may be a concern.

The concentration loss of hexachloroiridate(IV) is predominantly the result of either spontaneous reduction or hydroxylation. At weakly acidic to strongly acidic pH, the former seems more important. In neutral to alkaline media, the complex degrades quickly as a result of the hydroxylation reaction. As a consequence, hexachloroiridate(IV) is only sufficiently stable in solutions below pH 5, with the best results found for pH 4 or lower. Therefore, hexachloriridate cannot be used for metal electrodes that are unstable in acidic media.

In table 3 the main differences between both redox couples are summarized. The choice between both redox couples will largely depend on the type of electrode that is measured. For flat plate electrodes it is likely more cost-effective to use hexacyanoferrate and periodically polish the electrodes. For more complex electrodes, using hexachloroiridate may be preferred. Essentially, a trade-off exists between the cost of the electrode and the cost of the hexachloroiridate solution. The choice therein lies in whether to use a more expensive redox couple or to sacrifice the electrode. In either case, reliable results can be obtained as long as adequate care is taken towards the experimental conditions. In the case of hexacyanoferrate, transparent vessels should be avoided as ambient light significantly decreases the longevity of the complex.

Table 3: Comparison between the hexachloroiridate and hexacyanoferrate redox couple

	Hexachloroiridate	Hexacyanoferrate
Reaction	$\mathrm{IrCl_6^{3-} \rightleftharpoons IrCl_6^{2-} + e^-}$	$\mathrm{Fe(CN)_6^{4-} \rightleftharpoons Fe(CN)_6^{3-} + e^-}$
Redox potential	+0.8665 V_{SHE} [4]	+0.358 V_{SHE} [4]
Reduction plateau (Platinum WE)	+0.75 V_{SHE} to -0.25 V_{SHE}	+0.2 V_{SHE} to -0.6 V_{SHE}
Oxidation plateau (Platinum WE)	+0.95 V_{SHE} to +1.1 V_{SHE}	+0.5 V_{SHE} to +1.1 V_{SHE}
Diffusion coefficient	$8.38 * 10^{-10}$ m^2/s	$6.09 * 10^{-10}$ m^2/s
Solution pH	pH < 5	Avoid strong acids
Stability in solution	A few days to weeks [18]	Refresh daily [12]
Reduction stability:	39.2% loss after 16h	19.5% loss after 16h
Side reactions	Spontaneous reduction Hydroxide formation	Electrode poisoning Photosensitivity
Peak extinction coeff.	4.06 $mM^{-1}cm^{-1}$ (488 nm)	1.064 $mM^{-1}cm^{-1}$ (420 nm)

Acknowledgements

The authors of this work acknowledge the A.H. Schlatter for verifying the quality of the hexachloroiridate compound, A. Chaudhuri for verifying the water content using thermogravimetric analysis, and M.D.T. Claessen and G.J.M. Bouwman for their exploratory experiments comparing buffered and unbuffered hexachloroiridate solutions and the effect of pH.

Nomenclature

C = Concentration, M = mol/m^3

D_{ox} = Diffusion coeficient of the oxidant, m^2/s

D_{red} = Diffusien coefficient of the reductant, m^2/s

E = Potential, V

I_A = Current density, I_A

HER = Hydrogen Evolution Reaction

OER = Oxygen Evolution Reaction

References

[1] Mizushina T, The Electrochemical Method in Transport Phenomena, Adv. Heat Transf. 7 (1971) 87.

[2] Gomathi H, Chemistry and Electrochemistry of Iron Complexes, Bull. Electrochem., 16 (2000) 459.

[3] Ralph TR, Hitchman M, Millington J and Walsh FC, Mass transport in an Electrochemical Laboratory Filterpress Reactor and its Enhancement by Turbulence Promoters, Electrochim. Acta, 41(1996) 591.

[4] Beriet C and Pletcher DJ, A Microelectrode Study of the Mechanism and Kinetics of the Ferro-/Ferricyanide Couple in Aqueous Media, J. Electroanal. Chem., 361 (1993) 93.

[5] Stiebl M and Jüttner K, Surface Blocking in the Redox System Pt/[Fe(CN)6]3-,[Fe(CN)6]4-, J. Electroanal. Chem., 290 (1990) 163.

[6] Pons S, Datta M, McAleer J and Hinman A, Infrared Spectroelectrochemistry of the Fe(CN)6,4-/Fe(CN)6,3- Redox System, J. Electroanal. Chem., 160 (1984) 369.

[7] Kawiak J, Kulesza P and Galus Z, A search for conditions permitting model behavior of the [Fe(CN)6]3-/4- system, J. Electroanal. Chem., 226 (1987) 305.

[8] Taama W, Plimpley R and Scott K, Influence of Supporting Electrolyte on Ferricyanide Reduction at a Rotating Disc Electrode, Electrochimica Acta, 41(1996) 549.

[9] Niwa K and Doblhofer K, IR spectroscopic study of adsorbed species formed on electrodes during the Fe(CN)3−4−6 charge transfer reaction, Electrochim. acta, 31 (1986) 439.

[10] Baltruschat H, Lu F, Song D and Lewis S, Adsorption of Ferricyanide at Pt(111) as a Function of Electrode Potential Studied by Auger Spectroscopy, J. Electroanal. Chem., 234 (1987) 229.

[11] Kunimatsu K, Shigematsu Y, Uosaki K and Kita H, Study of the Fe(CN)6,3-/Fe(CN)6,4- Redox System on Pt by EMIRS, J. Electroanal. Chem., 262 (1989) 195.

[12] Szánto DA, Cleghorn S, Ponce-de-Léon C and Walsh FC, The Limiting Current for Reduction of the Ferricyanide Ion at Nickel, AIChE, 54 (2008) 802.

[13] Abrantes LM, Three-Dimensional Electrode, in: Kreysa G., Ota K., Savinell R.F. (Eds.), Encyclopedia of Applied Electrochemistry., Springer, New York, 2014, p.2077.

[14] Belding SR, Laborda E, Compton RG, Steady-state voltammetry at a microdisc electrode in the absence of excess supporting electrolyte for reversible, quasi-reversible and irreversible electrode kinetics, Phys. Chem. Chem. Phys., 14 (2012) 14635-14649

[15] Watkins JJ, White HS, Ion-pairing kinetics investigated using nanometer-size Pt electrodes, J. Electroanal. Chem. 582 (2005) 57-63

[16] Doneaux T, de Ghellinck A, Triffaux E, Brouette N, Sferrazza M, Buess-Herman C, Electron Transfer Across an Antifouling Mercapto-hepta(ethylene glycol) Self-Assembled Monolayer, J. Phys. Chem. C, 120 (2016) 15915-15922

[17] Watkins JJ, White HS, The Role of the Electrical Double Layer and Ion Pairing on the Electrochemical Oxidation of Hexachloroiridate(III) at Pt Electrodes of Nanometer Dimensions, Langmuir, 20 (2004) 5474-5483

[18] Petrovic S, Cyclic Voltammetry of Hexachloroiridate(IV): An Alternative to the Electrochemical Study of the Ferricyanide Ion, Chem. Educator, 5 (2000) 231.

[19] Weusten SJC, Murrer LCEM, de Groot MT and van der Schaaf J, Demystifying Mass Transfer in Electrolyzers through Rapid Prototyping with 3D Printed Parallel Plate Cells, in 2019 AIChE Annual Meeting, Orlando, USA, 10-15 November 2019.

[20] Taniguchi M and Lindsey J, Database of Absorption and Fluorescence Spectra of >300 Common Compounds for use in PhotochemCAD, Photochem. Photobiol., 94 (2018) 290.

[21] Lichtig J, Iodometric Standardization and Biamperometric Determination of Iridium(IV), Talanta, 29 (1981) 961.

[22] Wöhler L and Witzmann W, Die Oxyde des Iridiums, Z. Anorg. Chem., 57 (1908) 323.

[23] Rumble J, Electrochemical Series, in CRC Handbook of Chemistry and Physics, 99th edition, Press/Taylor & Francis, Boca Raton, 2018.

[24] Daubinger P, Kieninger J, Unmüssig T, Urban GA, Electrochemical characteristics of nanostructured platinum electrodes – a cyclic voltammetry study, Phys. Chem. Chem. Phys., 2014, 16, 8392

[25] Birss V and Damjanovic A, A Study of the Anomalous pH Dependence of the Oxygen Evolution Reaction at Platinum Electrodes in Acid Solutions, Journal of the Electrochem. Soc., 130 (1983) 1694.

[26] Birs V and Damjanovic A, Oxygen Evolution at Platinum electrodes in Alkaline Solutions, J. Electrochem. Soc., 134 (1987) 113.

[27] Macdougall B, Mitchell D and Graham M, The Use of Electrochemical and Surface-Analytical Techniques to Characterize Passive Oxide Films on Nickel, Corrosion-Nace, 38 (1982) 85.

[28] Arvia A, Bazán J, and Carrozza J, The Diffusion of Ferro- and Ferricyanide Ions in Aqueous Potassium Chloride Solutions and in Solutions containing Carboxymethylcellulose Sodium Salt, Electrochim. Acta, 13 (1968) 81.

[29] Konopka S and McDuffle B, Diffusion Coefficients of Ferri- and Ferrocyanide Ions in Aqueous Media, Anal. Chem., 42 (1970) 1741.

[30] Bazán J and Arvia A, The Diffusion of Ferro- and Ferricyanide Ions in Aqueous Solutions of Sodium Hydroxide, Electrochim. Acta, 10 (1965) 1025.

[31] Granados-Mendoza P, Weusten SJC, M. Groot, Keurentjes J, Schouten J and van der Schaaf J, Liquid-solid mass transfer to a rotating mesh electrode in a rotor-stator spinning disc configuration, Int. J. Heat Mass Transf., 104 (2017) 650.

[32] Selmian J and Tobias C, Mass transfer measurements by the limiting current technique, Adv. Chem. Eng., 10 (1978) 211.

[33] Morris D and Ritter T, Reduction of hexachloroiridate(IV) with borohydride, J. Less-Common Metals, 59 (1978) 73.

[34] Poulsen I and Garner C, A thermodynamic and kinetic study of hexachloro and aquopentachloro complexes of iridium(III) in aqueous solutions, J. Am. Chem. Soc., 84 (1962) 2032.

[35] Peoxoto Cabral J, Radiochemical processes in iridium complexes, J. Inorg. Nucl. Chem., 26 (1964) 1657.

[36] Fine DA, On the spontaneous reduction of hexachloroiridate(IV) in aqueous solution, Inorg. Chem., 8 (1969) 1014.

[37] Van Loon G and Page J, The Chemistry of Iridium in Basic Aqueous Solution, Can. J. of Chem., 44 (1966) 515.

[38] Nakagawa T, Beasley C and Murray R, Efficient Electro-oxidation of water near its reversible potential by a mesoporous IrOx nanoparticle film, J. Phys. Chem., 113 (2009) 12958.

[39] Hintermair U, Hashmi S, Elimelech M and Crabtree R, Particle Formation during Oxidation Catalysis with Cp*Iridium Complexes, J. Am. Chem. Soc., 134 (2012) 9785.

[40] Cabral P, Radiochemical processes in iridium complexes, J. Inorg. Nucl. Chem., 26 (1964) 1657.

Supporting information A

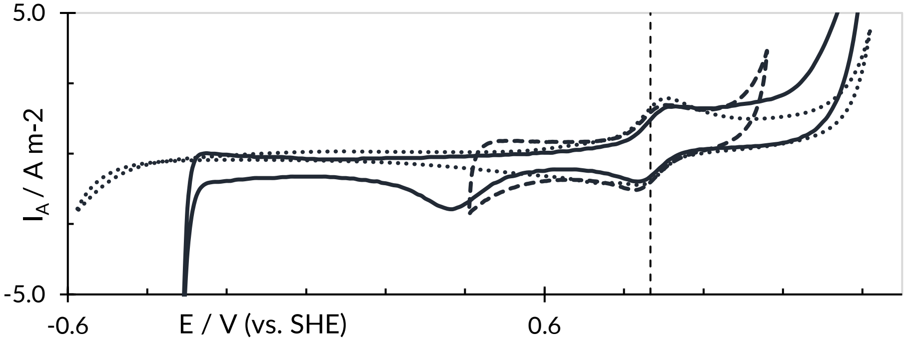

Figure A1: Cyclic voltammetry of 0.5 mM hexachloroiridate(IV) and 0.5 mM hexachloroiridate(III) at 40 mV/s in 0.1M pH4 acetate buffered, 0.5M KNO3 solution. Full line: on platinum, dashed line: on glassy carbon, dotted line: on nickel.

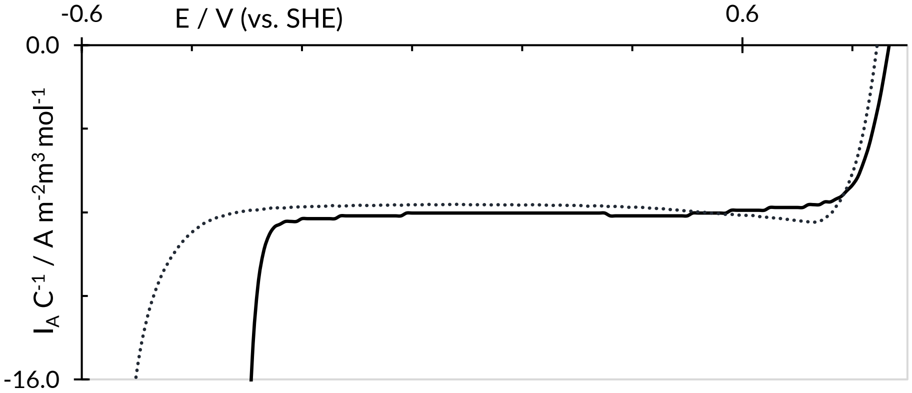

Figure A2: Linear sweep voltammogram at 10 mV/s and 2000 RPM. Full line: on platinum, dotted line: on nickel. The limiting current was corrected for the actual concentration of the oxidant species as tracked by the inline UV-VIS. The concentrations and compositions of the hexacyanoferrate and hexachloroiridate solutions are listed in table 1a and table 1b respectively.

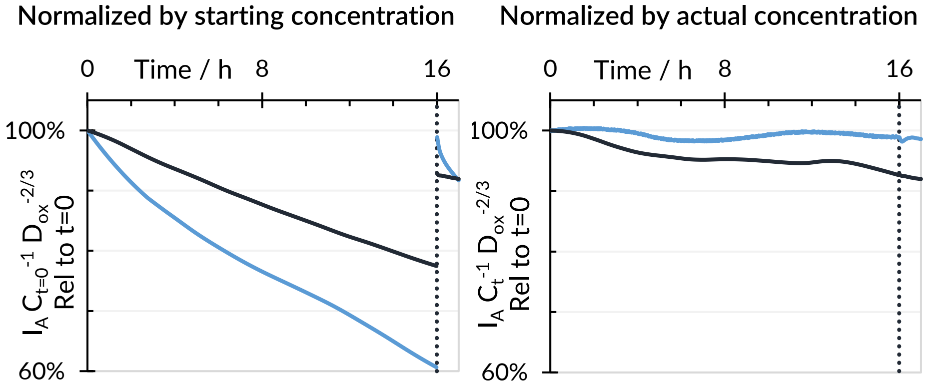

Figure A3: The limiting current density at 2000 RPM of the reduction of hexachloroiridate(IV) in blue and hexacyanoferrate(II) in black at nickel electrodes. At 16 hours, the solution was refreshed. The composition of the hexacyanoferrate and hexachloroiridate solutions are listed in table 1a and 1b. A platinum RDE was used for the top row, for the bottom row this was nickel. The left column is normalized by the initial concentration of the oxidant species as determined by ex-situ UV-VIS measurement. For the right column, the current density is normalized by the concentration the moment it was measured using the UV-VIS dip probe.

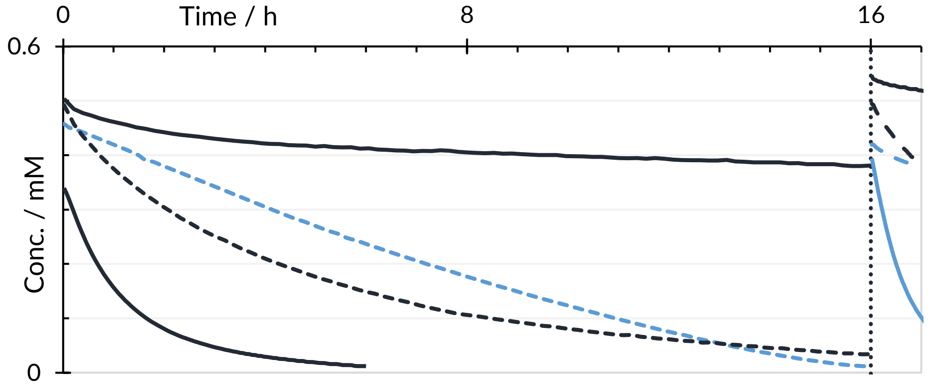

Figure A4: Concentration as determined by inline UV-VIS during the reduction of hexachloroiridate(IV) or hexacyanoferrate(II) in a 3D printed parallel plate electrolyzer with 40cm2 nickel electrodes (see figure 7). After 16 hours, the solution is refreshed. Full black line: hexacyanoferrate in 0.5M KNO3 (unbuffered); dashed black line: hexacyanoferrate in 0.5M KOH, full blue line: hexachloroiridate in 0.1M pH 4 acetate buffer, dashed blue line: hexachloroiridate in 0.1M pH 2 phosphate buffer. The target concentrations and compositions of the hexacyanoferrate and hexachloroiridate solutions are listed in table 1a and table 1b respectively.

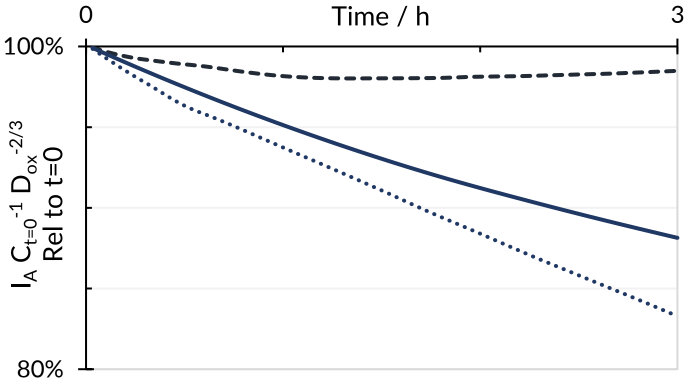

Figure A5: The limiting current density at 2000 RPM (RDE) of the reduction of 0.5 mM hexachloroiridate(IV) in the presence of 0.5 mM hexachloroiridate(III) and either 0.1M pH 2 phosphate buffered 0.5M KNO3 (dashed line), or 0.1 M pH 4 acetate buffered 0.5M KNO3 (full line), or 0.1M pH6 phosphate buffered 0.5M KNO3 (dotted line).

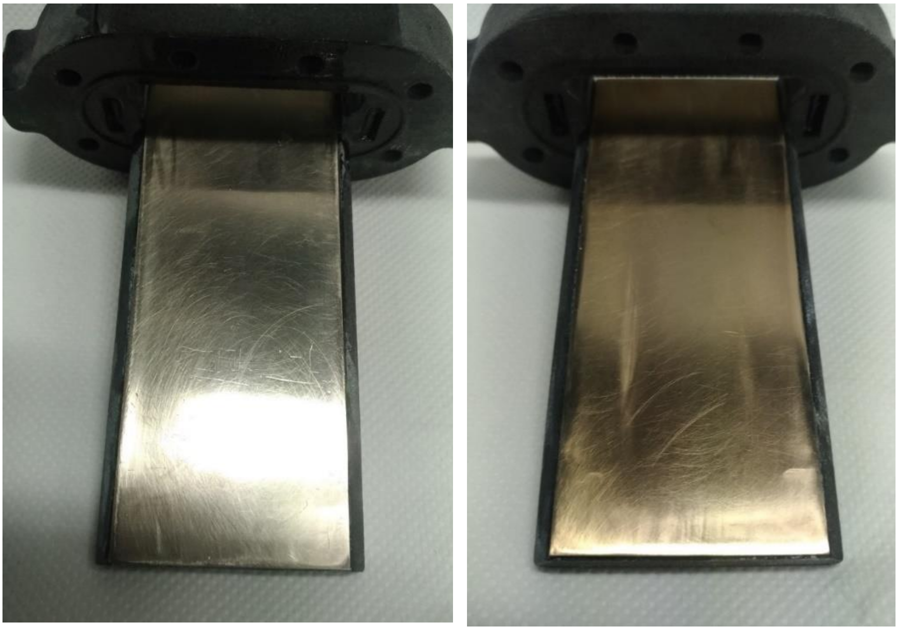

Figure A6: Yellowing of the electrodes in the printed cell. Left: before the 17h reduction experiment shown in figure 7, right: after 17 hours of hexacyanoferrate(III) reduction in 0.5M KOH.

Supporting information B

Both hexachloroiridate(IV) and hexacyanoferrate(III) form colored solutions when dissolved. Moreover, the color of these solutions is easily distinguished from the color of respectively hexachloroiridate(III) and hexacyanoferrate(II). As a result, it is possible to measure their concentration using UV-VIS spectroscopy. To that end, extinction coefficients can be determined for each component using a simple calibration series. However, in the case of hexachloroiridate (IV) this procedure is complicated by the spontaneous reduction reaction.[36] Essentially, part of the compound is immediately reduced upon dissolving, meaning that its weighed mass does not fully end up as hexachloroiridate(IV) in the solution. As a result, it is unreliable to determine the solution concentration by the mass of the compound weighed during preparation (see table 3). Instead, the actual hexachloroiridate(IV) content must be determined through a second analytical technique such as iodometric titration.[21-22] Using this method, molar extinction coefficients were obtained for hexachloroiridate(IV) (table B.1). The hexachloroiridate(IV) extinction found here agrees well with that of Poulsen et. Al. (4.050 ± 35 1/mM/cm).[30]

Table B1: Colors and molar extinction coefficients of the species used in this work.

Species	Color	Peak abs. nm	Molar ext. $mM^{-1}\,cm^{-1}$	Medium
Hexachloro-iridate(IV)	Dark brown	488|435| 418|305	4.063|3.131| 3.037|1.262	0.1 M HCl
		488|435| 418|305	4.060|3.157| 3.068|1.294	Pure water
Hexachloro-iridate(III)	Light yellow	415	0.097	0.5 M KNO3 0.1 M Acetate
Hexacyano-ferrate(III)	Light green	420	1.064	0.5 M KNO3
Hexacyano-ferrate(II)	Colorless	362.5	0.045	0.5 M KNO3

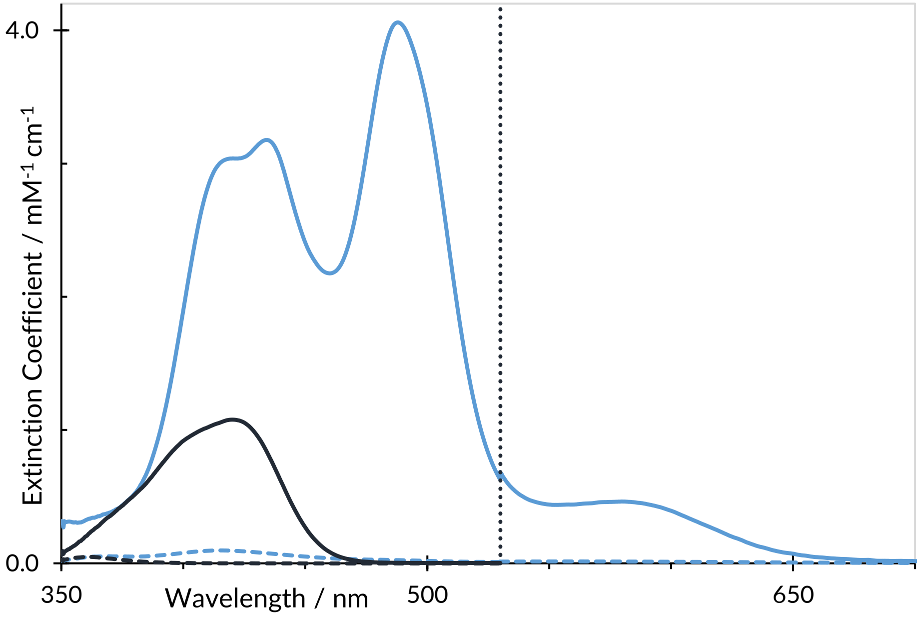

Figure B1: Spectra of the electro-active species used in this work. Blue full line: hexachloroiridate(IV), black full line: hexacyanoferrate(III), blue dashed line: hexachloroiridate(III), black dashed line hexacyanoferrate(II) (barely visible between 350-380nm). Solutions of 0.5mM were used for the oxidant species and 2.0mM for the reductant species due to their significantly lower absorbance. The spectra are shown as extinction coefficients vs. wavelength to account for this difference in concentration. For hexachloroiridate(IV) the effect of the spontaneous reduction was taken into account and corrected for by using the iodometric method described earlier. The range from 350 nm to 530 nm was observed separately from the range of 520nm to 700nm and was been combined afterwards. A vertical dotted line denotes the seam.

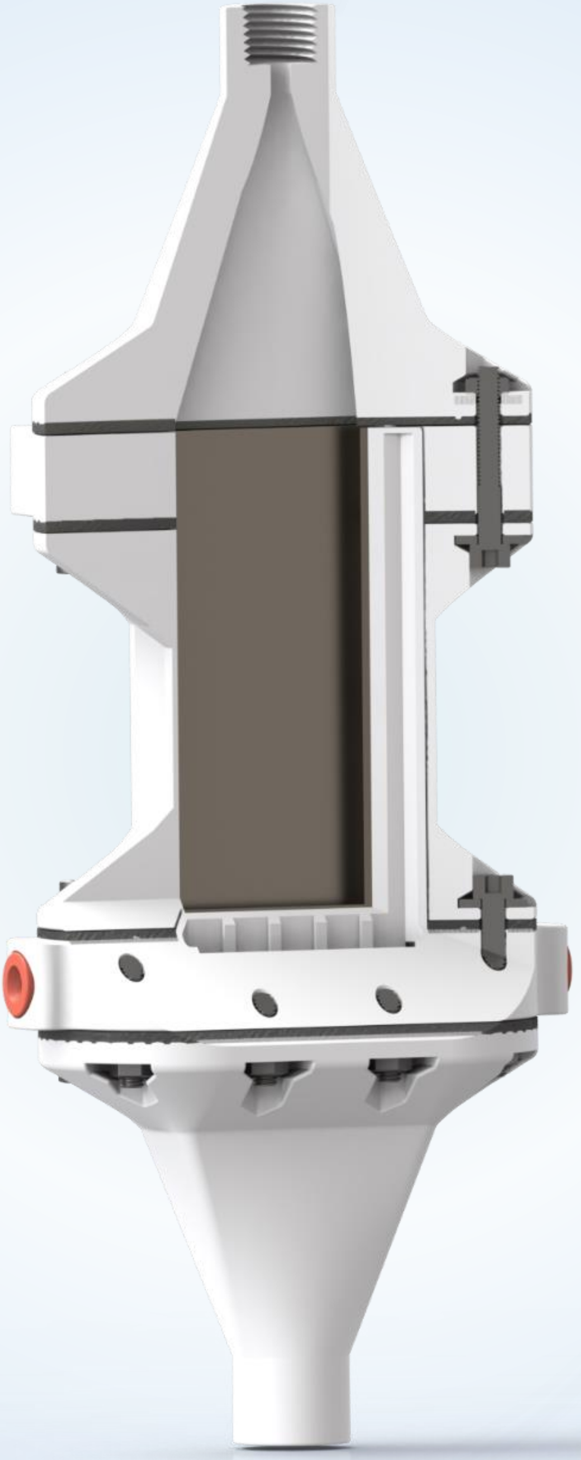

Mass Transfer in 3D printed electrolyzers:
The importance of inlet effects

S.J.C. Weusten, L.C.E.M. Murrer, M.T. de Groot, J. van der Schaaf

3 - Abstract

Many mass transfer correlations have been established for parallel plate electrolyzers, and the predicted performance differs up to a factor 10 depending on electrolyzer type. In this paper we investigate the effect of inlet shape, entrance length and turbulence promoters on mass transfer by using 3D printed electrolyzers. Our results show that the inlet design can promote turbulence and leads to an earlier transition to turbulent flow. The Reynolds number at which the transition occurs can be predicted by the ratio of the cross-sectional area of the inlet to the cross-sectional area of the electrolyzer channel. A longer entrance length results in more laminar behavior and a later transition to turbulent flow. With an entrance length of 550mm, the inlet design did no longer affect the mass transfer performance significantly. The addition of gyroid type turbulence promoters resulted in a factor 2 to 4 increase in mass transfer depending on inlet design, entrance length and the type of promoter. From one configuration to another, there was a minimal variation in pressure drop (<16 mbar). Though the difference was very small, higher pressure drops coincided with higher rates of mass transfer. The observations on the investigated effects can explain the large variations up to a factor 10 found in literature.

Image: the 3D printed electrolyzer used in this work

3.1. Introduction

In recent years, a renewed interest in electrolyzers has emerged. They are expected to play a pivotal role in enabling the ongoing global energy transition, as they are able to directly convert electricity into chemical energy. Moreover, the process can be done cleanly if green energy is used, thereby opening up the way to a sustainable chemical industry.

A key property of an electrolyzer is its mass transfer performance. A high mass transfer performance indicates that the reactants can quickly reach the electrode, in this way enabling faster reactions and higher currents. Typically, mass transfer is expressed as a Sherwood-Reynolds correlation. In the past decades, many such correlations have been established,[1-5] but there is a large variance in the reported mass transfer performance. For empty parallel plate electrolyzers, the difference can be up to an order of magnitude depending on the configuration and specific design choices that were used, such as e.g. the design of the inlet.[1] In literature, several CFD studies are available that investigate these effects.[6-7] However, the comparison of results between reactors remains complicated. Moreover, the importance of certain mass transfer enhancing effects depends on the scale. Small-scale electrolyzers for instance will be affected more by inlet effects than large scale cells. Therefore, when results from a small cell are extrapolated to a larger electrolyzer, significantly over- or underestimations can occur if these scaling effects are not considered.

In order to increase our understanding of mass transfer in electrolyzers more configurations need to be tested. Therein lies another complication since most of the cells described in the literature were built in-house or produced decades ago, resulting in them no longer being available for present-day research. For new research, it can therefore be difficult to find a suitable cell with known mass transfer behavior. Building new ones is not straightforward either, as it requires design work and complex machining. A solution to this problem is to 3D print electrolyzers, as it allows the quick construction of numerous prototypes.

The purpose of this work is to carry out a systematic investigation into electrolyzer mass transfer performance. 3D printed parallel plate electrolyzers are used to investigate the effects of different inlet designs, inlet lengths, and turbulence promoters and results are compared to previous work.

3.2. Theory

3.2.1. Measuring mass transfer

The limiting current density method is often used to determine the mass transfer performance of electrolyzers.[8-9] Typically, this involves reversible redox couples such as hexacyanoferrate or hexachloroiridate , for which the rate of reaction is limited by mass transfer at sufficient overpotential.[10-12] The limiting current is related to the Sherwood number as shown in eq. 1.

$$Sh = \frac{d_H}{D} . k_{LS} = \frac{d_H}{D} . \frac{i_{A,lim}}{n\, F\, C_{bulk}} \qquad \text{eq.1}$$

To understand how mass transfer occurs in electrolyzers it is important to realize that there are two different boundary layers (see figure 1). The first, is the hydrodynamic boundary layer which is the region where the velocity of the flow is lower due to friction with the wall. The second is the diffusive boundary layer, which is where the concentration of reactant species is lower due to the reaction at the electrode surface. In liquids the diffusive boundary layer is much thinner than the hydrodynamic boundary layer, since liquid diffusion coefficients are typically at least a factor 1000 smaller than liquid viscosities. Moreover, the hydrodynamic and diffusive boundaries do not necessarily develop simultaneously. For instance, if an inert section of wall precedes the electrode, then the flow can be hydrodynamically developed before the diffusive boundary layer begins to form. Essentially, there are three distinct situations:

(A) Hydrodynamically and diffusively developing flow

(B) Hydrodynamically developed, but diffusively developing flow

(C) Hydrodynamically and diffusively developed flow

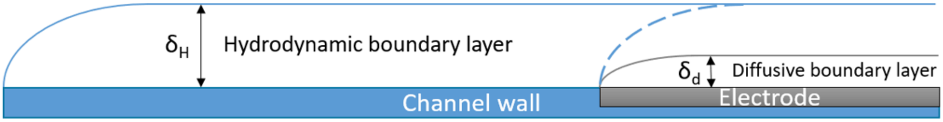

Figure 1: Illustration of the boundary layers. The blue line shows the hydrodynamic boundary layer, the gray line the diffusive boundary layer. The hydrodynamic boundary layer can develop simultaneously to or before (blue line) the diffusive boundary layer (gray line).

Situation A is most common in electrolyzers, where the electrode typically starts directly after the inlet. Situation B occurs when a certain entrance length without electrodes is used in which the flow is allowed to develop before reaching the electrodes. Situation C only occurs after a certain length of electrode and can therefore only be seen in the downstream segments of a segmented electrode.

The distance required for a flow to reach fully developed conditions is known as the hydrodynamic entrance length. More specifically it is defined as the length needed for the centerline velocity to reach 99% of its fully developed value. In laminar flow, the entrance length depends on the Reynolds number as shown in eq. 2.

$$L_{entry} = \Phi \, d_h \, Re \qquad \text{eq. 2}$$

Where Φ is a parameter that depends on the geometry. For a rectangular channel it is nonlinearly dependent on the aspect ratio of the cross-section γ'.[13] Table 1 lists the six values Han established.[13]

Table 1: Φ values in a rectangular channel as a function of γ', from Han et al.

$\gamma' = S/B$	Φ
1.000	0.0752
0.750	0.0735
0.500	0.0660
0.250	0.0427
0.125	0.0227
0.000	0.0099

To obtain fully developed turbulent flow, a hydrodynamic entrance length is required that is 50 hydraulic diameters d_H long, regardless of the flowrate.[14]

In figure 2 the current in a typical mass transfer experiment is shown. In such an experiment the flow is turned on prior to the potential, giving the hydrodynamic boundary layer time to develop. When the potential is applied (at t=0), a current appears and quickly trends toward a stable value that is determined by the thickness of the diffusive boundary layer. The high initial current is due to the development of this layer. At most flowrates, the reaction is fully limited by mass transfer from the bulk after at most 7 seconds. At low flow rates (20 dm^3/h and 30 dm^3/h), it takes several seconds longer for the diffusive boundary layer to develop. This is because at lower flow rates the diffusive boundary layer is thicker and therefore there is more reactant present in this layer.

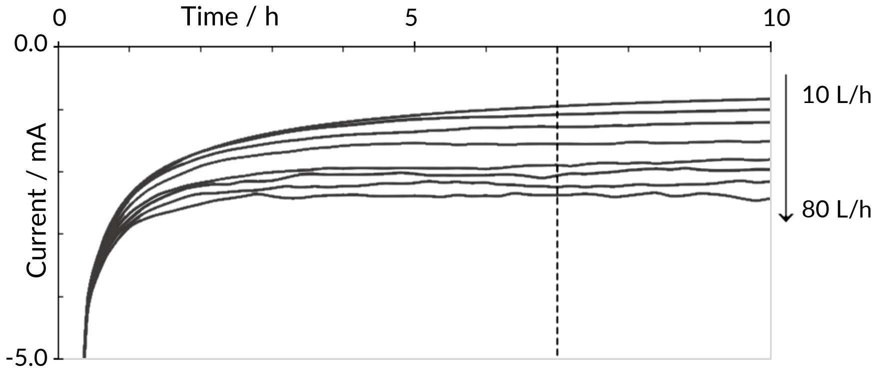

Figure 2: Current in a mass transfer experiment. The empty channel printed electrolyzer with conic inlets was used here. The electrolyte composition is given in table 3. The flow rate ascends from 10 dm3/h to 80 dm3/h in steps of 10 dm3/h from top to bottom.

3.2.2. Mass transfer in hydrodynamically developed flow

In a perfectly laminar flow, with a perfectly hydrodynamically developed flow, the mass transfer coefficient between parallel plates in a rectangular channel can be described by a theoretical Leveque-type equation, eq. 3a.[14] Here, γ is the aspect ratio of the electrode: B/L. In the work of Ong and Picket no significant effect has been found of the developing diffusive layer on the rate of mass transfer in laminar flow. As a consequence, eq.3a is valid for both short and long electrodes.[14-15]

$$Sh = 1.467\left(\frac{2}{1+\gamma}\right)^{0.33}\left(Re\,Sc\,\frac{d_H}{L}\right)^{0.33} \qquad \text{eq.3a}$$

In some publications an alternative correlation is reported in the form of eq.3b. [1,15-16]. This correlation is based on a best fit of the experimental data obtained by Ong and Pickett.[15] The difference with eq. 3a has been explained as being the result of electro-organic absorption of m-nitrobenzene.[14]These electro-organic impurities poison the electrode surface resulting in lower than expected mass transfer, especially at higher flowrates. Similar poisoning behavior is seen for the hexacyanoferrate redox couple.[10-12]

$$Sh = 2.54\left(Re\,Sc\,\frac{d_H}{L}\right)^{0.296} \qquad \text{eq.3b}$$

The correlations for a perfectly developed turbulent regime are based on analogies between momentum and mass transfer. Many different analogies exist, both theoretical (Prandtl, Von Karman) and empirical (Chilton-Colburn, Lin-Koulton-Putnam, Deissler, Vieth-Porter-Sherwood, Wasan-Wilke, Dittus-Boelter). Most of these analogies can be rewritten in the form of $Sh \sim Re^{b}\,Sc^{c}$, with varying powers of Re and Sc. In the work of Ong, the Chilton-Colburn analogy is found to be most representative of their dataset:[14]

$$Sh = \frac{f}{2} Re\,Sc^{0.33} \qquad \text{eq. 4a}$$

This analogy sets c at a value of 0.33 and uses the friction factor f. Typically, f is determined by a further correlation to the Reynolds number, i.e.: $f \sim a^{*}Re^{b^{*}}$. In some references, eq.4a is written using the J-factor instead of the friction factor.[14-15,17] The M subscript denotes mass transfer. The J-factor is equal to f/2:

$$Sh = J_M Re\, Sc^{0.33} \qquad \text{eq. 4b}$$

For fully developed turbulent flow, Pickett and Ong determined two separate correlations for the J-factor: one for short electrodes with $Le = L/d_H < 10$, and another for long electrodes with $Le = L/d_H > 12$.[15] Filled into eq.4b, these result in eq.5a and eq.5b. For short electrodes (eq.5a) the Le number was introduced as a variable, because mass transfer depended significantly on their relative length. Hence eq. 5a corresponds to a situation that is hydrodynamically developed, diffusively developing, whereas eq. 5b corresponds to a turbulent, hydrodynamically and diffusively developed situation.

$$Le < 10: \quad Sh = 0.125\, Re^{0.66} Sc^{0.33} Le^{-0.25} \qquad \text{eq. 5a}$$

$$Le > 12: \quad Sh = 0.023\, Re^{0.8} Sc^{0.33} \qquad \text{eq. 5b}$$

3.3. Experimental

In this work, a 3D-printed electrolyzer was used. The structural parts of the 3D-printed electrolyzer were printed both in-house and externally. In the former case, a Makergear M3-ID or a Prusa MK3S was used. In both printers, PETG was extruded during the fused filament fabrication process. In the latter case parts were ordered from the 3D printing company ZiggZagg, who used the multi jet fusion of Nylon. The gaskets were printed in-house using TPU filament Ninjatek-Ninjaflex and the Makergear M3-ID. The electrolyzer is shown in figure 3 and consisted of exchangeable inlets and electrode assemblies. In table 2 the characteristic dimensions of the electrolyzer are shown. The electrode assembly was built by affixing a 100x50mm nickel plate to a printed substrate using epoxy resin. The electrical connection was provided by two wires soldered to the backside of the nickel plate on one end, and 2 banana plugs on the other end.

Table 2: Geometric details of the electrolyzer used in this work

Symbol	Property	Value
L	Electrode length	10 cm
B	Electrode width (breadth)	4 cm
S	Electrode spacing	0.5 cm
A	Electrode area	40 cm^2
γ	Electrode aspect ratio B/L	0.40
d_H	Hydraulic diameter 2*B*S/(B+S)	0.89 cm
Le	Length number L/d_H	11.25 cm

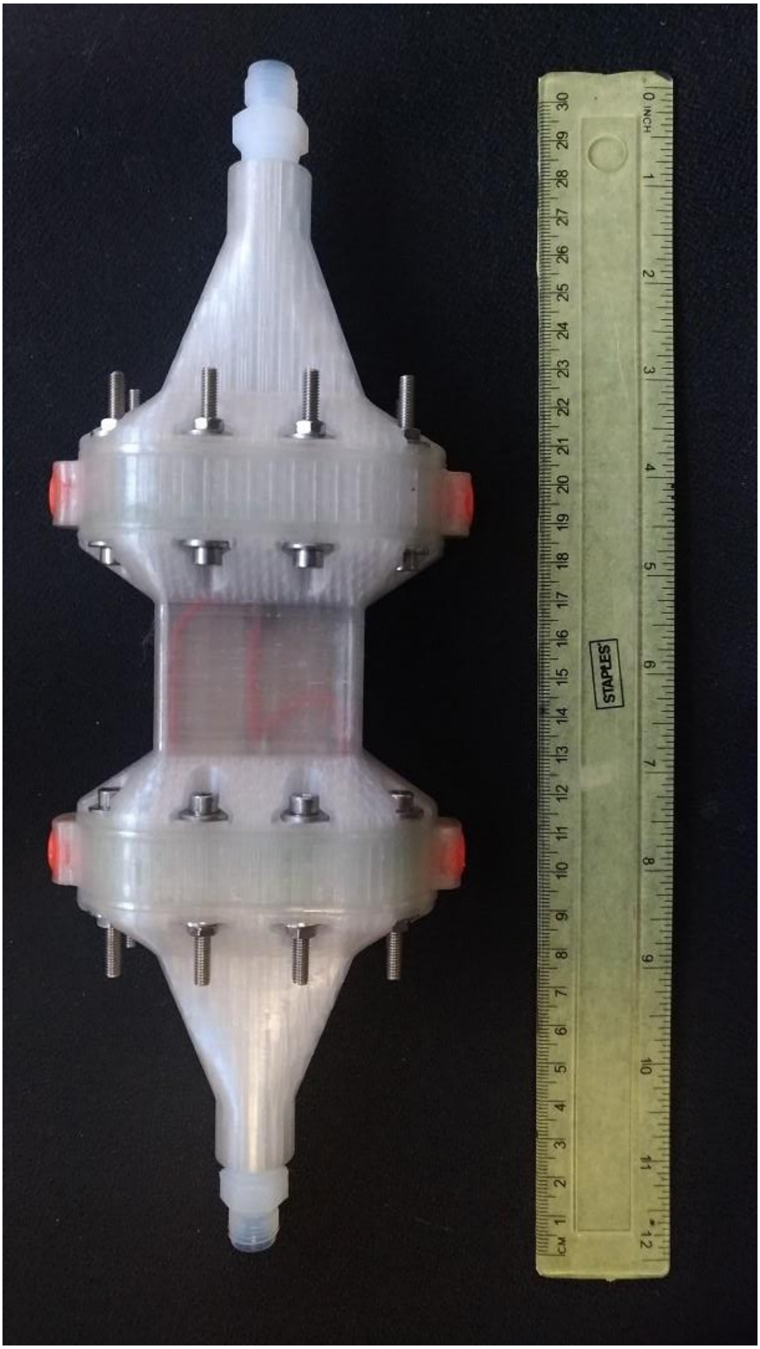

Figure 3: Photograph of the printed electrolyzer in its shortest configuration.

For the 3D-printed electrolyzer, three different inlets were used in this work: a tube inlet, a conic inlet, and a divider inlet (see figure 4). Additionally, it was possible to add a calming section with printed extender pieces that were either 100 mm, 150 mm or 200 mm long, thereby increasing the hydrodynamic entrance length. These extender pieces contained an empty rectangular channel with the same cross-section as the part containing the electrodes. Measurements with longer calming sections of 300 mm and 550 mm were carried out by using multiple extender pieces.

Turbulence promoters could be inserted into the channel of the electrolyzers. Four different designs were tested: tube grid, large gyroid, medium gyroid and small gyroid (figure 5). The designs were printed in a small form (100x40 mm) built to fit the non-extended electrolyzer and a longer 250x40 mm form meant to fit a channel extended by 150 mm (figure 6).

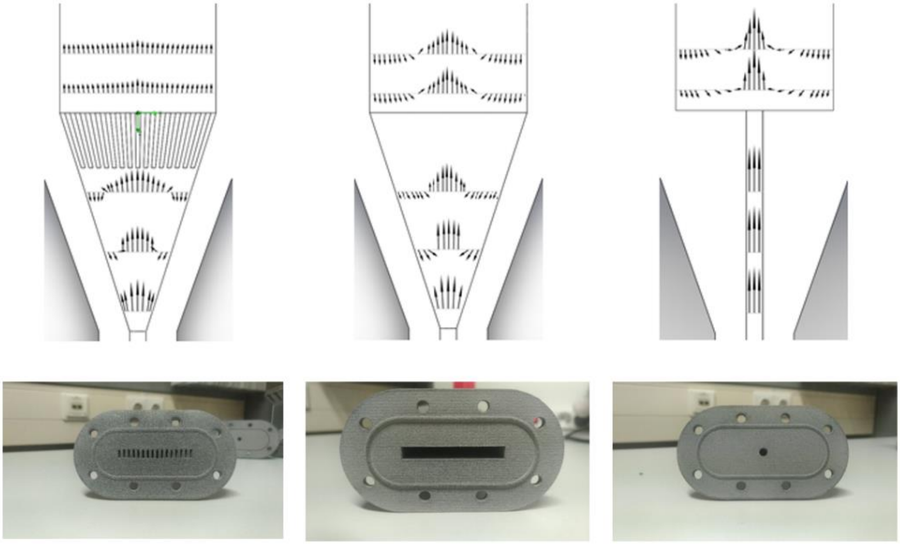

Figure 4: Different inlets for the printed electrolyzer. Top row: Schematic top-down view of the expected flow pattern, bottom row: photographs. From left to right: the divider type inlet, the conic inlet and the tube inlet. Note that the material is different from figure 3, this is because these inlets were made using selective laser sintering of Nylon rather than filament extrusion printing.

Figure 5: 3D printed turbulence promoters used in this work. From left to right: Tube grid promoter, large gyroid, medium gyroid and small gyroid. These are the 100 mm long variants, 250 mm long variants were also used.

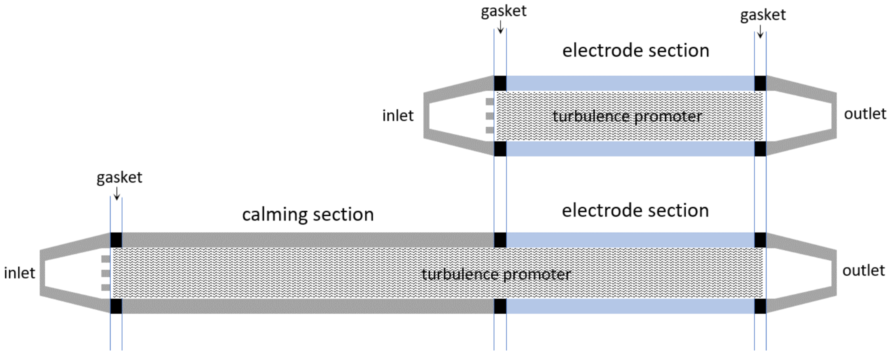

Figure 6: schematic of the electrolyzer and turbulence promoter without (top) and with a 150 mm calming section (bottom)

The setup consisted of an electrolyte vessel connected via a gear pump to the printed electrolyzer and is schematically shown in figure 7. A variable area flow meter (Swagelok) was used to measure the flow rate. The pressure drop was measured by means of an 800 mm tall U-tube filled with water. The electrolyte vessel was continuously flushed with nitrogen. A water lock was used to prevent backmixing of atmospheric oxygen. The concentration of the oxidant (hexachloroiridate(IV)) was tracked throughout the experiment using an inline UV-VIS flow cell (Avantes).

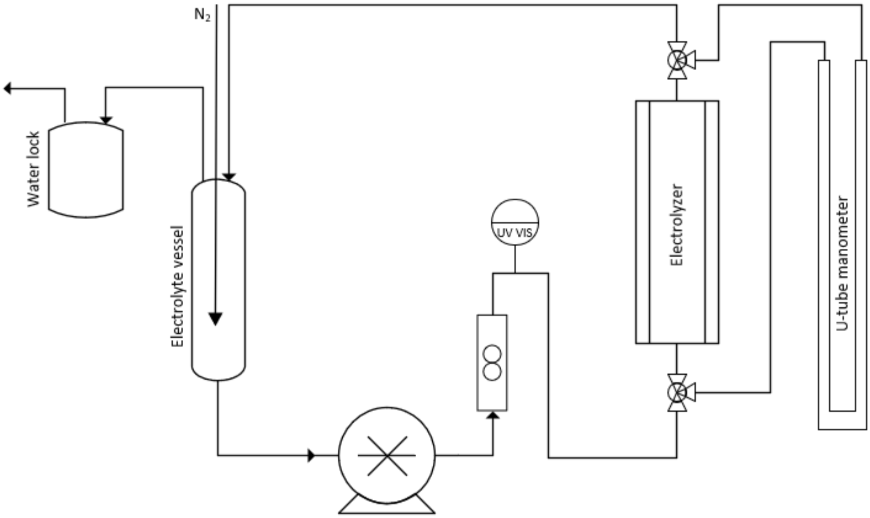

Figure 7: Schematic of the setup. From the electrolyte vessel the electrolyte is pumped by a gear pump through a flow meter and inline UV VIS sensor to the electrolyzer. Right before and after the electrolyzer a T piece connects to the U-tube in order to measure the differential pressure. The electrolyte vessel is bubbled with nitrogen, and any excess gas is allowed to escape through a waterlock, which prevents backmixing of air.

The hexachloroiridate(IV)/hexachloroiridate(III) redox couple was used for the limiting current density measurements. The electrolyte consisted of 0.5 mol/m^3 potassium hexachloroiridate(IV) (>99.99% from Merck/Sigma Aldrich) and 1.0 mol/m^3 hexachloroiridate(III) (>99.9% from Merck/Sigma Aldrich) in a solution of 0.5 mol/dm^3 KNO_3 (>99% from VWR Chemicals), containing 0.1 mol/dm^3 of potassium acetate pH 4 buffer (made from >99% potassium acetate and >99% acetic acid from VWR Chemicals). More background on the performance of the hexachloroiridate redox couple can be found in previous work .[18] A list of the electrolyte properties is available in table 3.

Table 3: Physical properties of the electrolyte, relevant constants

Symbol	Property	Value
$\boldsymbol{\rho}$	Density of the electrolyte	1029.8 kg/m^3 [16-17]
$\boldsymbol{\nu}$	Kinematic viscosity	9.52*10^{-7} m^2/s [17]
$\boldsymbol{T}$	Temperature	298 K
$\boldsymbol{C_{(III)}}$	Concentration of hexachloroiridate(III)	1.0 mol/m^3
$\boldsymbol{C_{(IV)}}$	Concentration of hexachloroiridate(IV)	0.5 mol/m^3
$\boldsymbol{D}$	Diffusion coefficient of hexachloroiridate(IV)	8.38*10^{-10} m^2/s
$\boldsymbol{Sc}$	Schmidt number of the electrolyte	1011

Before the experiments, the electrodes were pretreated following the recommendations of Szanto et al. [11] The procedure consisted of polishing the electrodes using felt paper and a descending series of alumina particles (namely 1.0 µm, 0.3 µm and 0.05 µm), followed by two times 15 minutes sonication and 15 minutes of hydrogen evolution in 0.5 mol/dm^3 KOH solution. The setup was then thoroughly rinsed with a solution containing 0.1 M pH 4 acetate buffer and 0.5 mol/dm^3 KNO_3. During this time, a baseline measurement of the UV-VIS probe was taken. After this, the setup was drained, flushed with nitrogen and the hexachloroiridate electrolyte was added. For another 15 minutes, nitrogen was bubbled through the electrolyte vessel to remove dissolved oxygen from the solution.

Chronoamperometry experiments were performed in order to determine the limiting current density. The procedure was as follows: First, the gear pump was set in motion to produce the desired flow rate. Then, a cell potential of -0.8 V was applied and a waiting time of at least 7 seconds was implemented in order to reach a steady state situation. The limiting current was determined from the average of 30 data points measured over a period of 3 seconds after the current had stabilized.

In our work we record all current data after 7 seconds. Since for low flow rates (see figure 2) the current has not always completely stabilized after 7 seconds, the Sherwood numbers obtained at lower flow rates (and hence lower Reynolds numbers) may be overestimated slightly in our work.

3.4. Results and discussion

3.4.1. Overview of mass transfer correlations in electrolyzers

Numerous experimental studies with the aim of establishing mass transfer correlations have been reported.[1-5,14-16,20-38] (See table 4 and figure 8) Generally, they are of the form $Sh = a\,Re^{b}Sc^{c}Le^{-d}$. For these, the Schmidt power is typically set to 0.33 which is in accordance with the Chilton-Colburn analogy. In rare cases, the relative length of the electrode $Le = L/d_H$ is taken into consideration, denoted by a non-zero d coefficient. Typically, this is done when a dependency on the electrode length could be confirmed. However, most studies do not vary the electrode length which could be a reason for not including this parameter in their investigation.

Generally, literature correlations show Reynolds powers between 0.6 and 0.8, which is an indication of a turbulent regime. The correlations by Picket et al. [15] for developed turbulent flow also follow this trend: for short electrodes the power is 0.66, for long electrodes it is 0.8. Interestingly, most electrolyzers appear turbulent long before the expected transition point of Re = 2000. This could be due to several reasons, such as surface roughness, turbulence caused by the inlet or even imperfections in the cell itself.

The rate of mass transfer varies significantly depending on the electrolyzer type. In e.g. the UA16.15, a mass transfer rate is found that is nearly 10 times higher than the correlations by Picket et al. In other electrolyzers, increased mass transfer is also observed, though the effect is less extreme. There are several explanations for this difference: Firstly, most electrolyzers do not use calming sections and are therefore not operating in developed flow, unlike the one used in the work of Pickett et al.[15] Secondly, significant turbulence is generated by the inlets into the channel, which varies between designs. Thirdly, the design of the channel could be of importance: square, rectangular and even circular parallel plates have been used in literature.[25,30,36] Finally, within the same electrolyzer variations in performance may exist as a result of differences in assembly. For instance, with a filter-press design, the layers of gaskets, spacers and electrodes may be stacked in slight misalignment. This would result in higher than expected mass transfer than expected due to these misalignments. In turbulent flow the surface roughness is also of importance.[31]

Table 4: Literature correlations of parallel plate electrolyzers and their geometric data

	Cell type	a	b	c	d	Reynolds	S	L	B	dH	Le
[13]	Dev. Laminar (Pickett) †	2.10	0.33	0.33	0.33	58 - 2000	7	149	40	12	12.51
[13]	Dev. Turbulent Le >12 (Pickett)	0.023	0.8	0.33	-	2000 - 20000	7	149	40	12	12.51
[13]	Dev. Turbulent Le <10 (Pickett)	0.125	0.66	0.33	0.25	4000 - 20000	7	60	40	12	5.04
[1]	FM01-LC (Hammond)	0.174	0.68	0.33	-	120 - 450	6	160	40	10	16.55
[18]	FM01-LC (Brown)	0.22	0.71	0.33	-	200 - 1000	6	160	40	10	16.55
[22]	FM01-LC (Griffiths)	0.18	0.73	0.33	-	500 - 2200	6	160	40	10	16.55
[22]	FM01-LC (Szanto)	0.24	0.7	0.33	-	200 - 1000	6	160	40	10	16.55
[5]	ElectroSyn (Carlsson)*	0.39	0.63	0.33	-	70 - 800	9	297	148	17	17.50
[1]	Filterpress (Ralph)	0.28	0.7	0.33	-	148 - 6109	20	100	100	33	3.00
[23]	DiaCell (Santos)	0.141	0.7	0.33	-	100 - 2500	7	130	94	13	9.98
[28]	Unbaffled (Wragg)	0.19	0.812	0.33	-	1250 - 6900	15	150	150	27	5.50
[28]	Baffled (Wragg)	0.46	0.66	0.33	-	3000 - 15000	15	450	50	23	19.50
[26]	Unbaffled (Oduoza)	0.49	0.7	0.33	-	900 - 10000	15	150	150	27	5.50
[26]	Baffled (Oduoza)	0.91	0.6	0.33	-	2500 - 20000	15	450	50	23	19.50
[4]	UA200.08 (González)	0.35	0.7	0.33	-	94 - 804	8	120	180	15	7.83
[21]	UA16.15 (Frías-Ferrer)	1.08	0.61	0.33	-	272 - 2571	15	40	40	22	1.83
[21]	UA63.15 (Frías-Ferrer)	0.84	0.63	0.33	-	170 - 1664	15	90	70	25	3.64
[21]	UA63.03 (Frías-Ferrer)	0.17	0.82	0.33	-	117 - 629	3	90	70	6	15.64
[27]	3D Printed (Ponce de Leon)	1.22	0.65	0.33	0.25	150 - 800	14	70	70	23	3.00

Note †: The correlation for developed laminar flow is based on eq. 3a, with $a = 1.467\left(\frac{2}{1+\gamma}\right)^{0.33}$*, where* γ *is calculated for the dimensions of the printed electrolyzer.*

*Note *: For the Electrosyn cell a different correlation is given in reference [1] compared to reference [5]. Here we report the latter.*

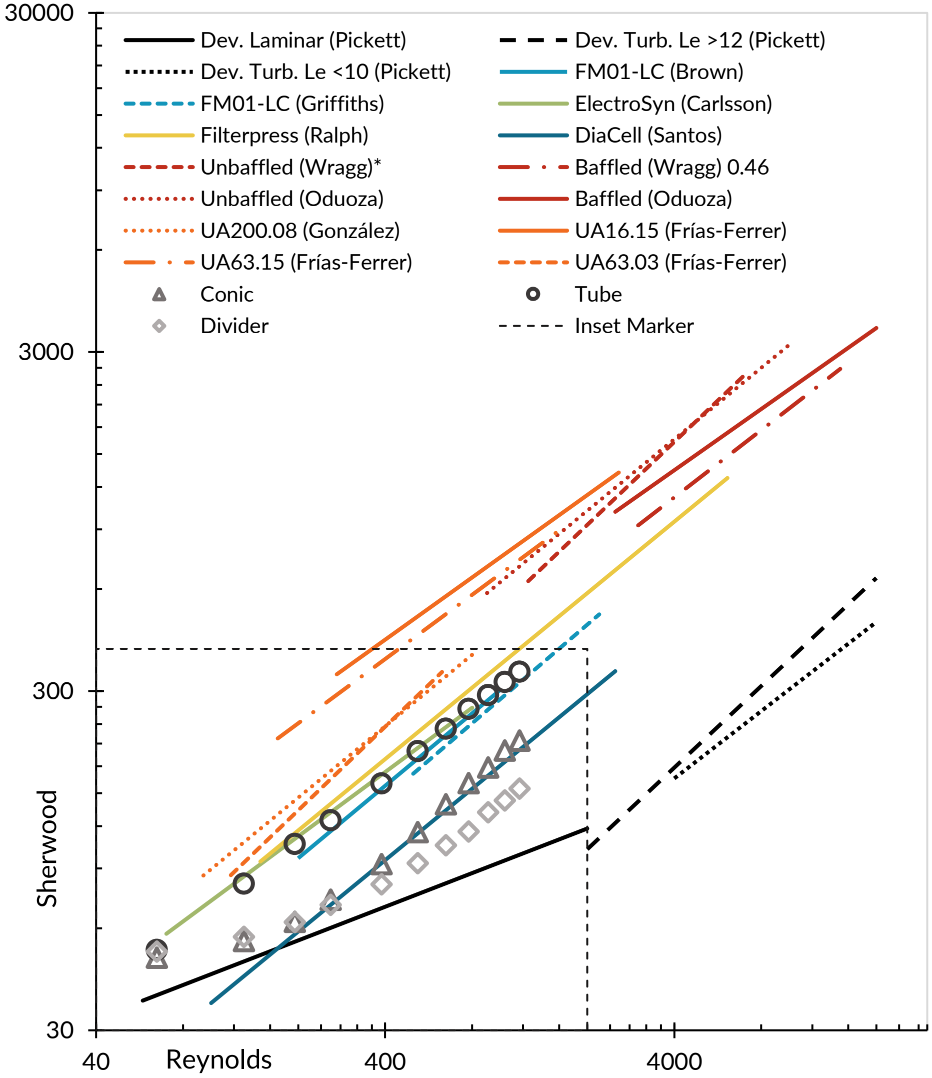

Figure 8: Sherwood-Reynolds plot of the correlations shown in table 4. Lines in this graph denote literature correlations within their respective Reynolds ranges. Except for the developed flow correlation, all correlations were plotted using the geometric parameters given for the electrolyzer the correlation was established with. For the developed flow correlation, the geometric data of the printed electrolyzer used in this work was used. This was done to offer a comparison between our experimental data and the developed flow prediction. The circle, triangle and diamond markers are experimental data obtained with the 3D printed electrolyzer whose correlations are shown in table 6. Electrolyte data is available in table 3. The dashed box (extending from the origin to Sh = 400 and Re = 2000) marks the region of this graph that is used for figure 9.

3.4.2. 3D printed electrolyzer with different inlets

To systematically investigate inlet effects, we developed a modular 3D printed electrolyzer with exchangeable inlets. Three types of inlets were used: a conic inlet, a tube inlet and a divider type inlet (shown in figure 4). Results for these inlets are shown in figure 9. All three inlets produce higher rates of mass transfer than expected from the predictions by Pickett et al (eq 2.). Furthermore, for the conic and divider type inlet, a region with a smaller slope and a (Re < 300) region with a larger slope (Re > 300) can be discerned. The tube inlet shows a large slope at all flow rates. The aforementioned regions represent laminar and turbulent flow respectively. In the laminar region, a similar performance is seen for the conic and divider inlet. Therefore, only one mass transfer correlation is established (eq.6) for both inlets in laminar flow (Re <300).

$$Conic, divider\ inlet: Re < 300: \quad Sh = 1.72\, Re^{0.247} Sc^{0.33} \qquad \text{eq. 6}$$

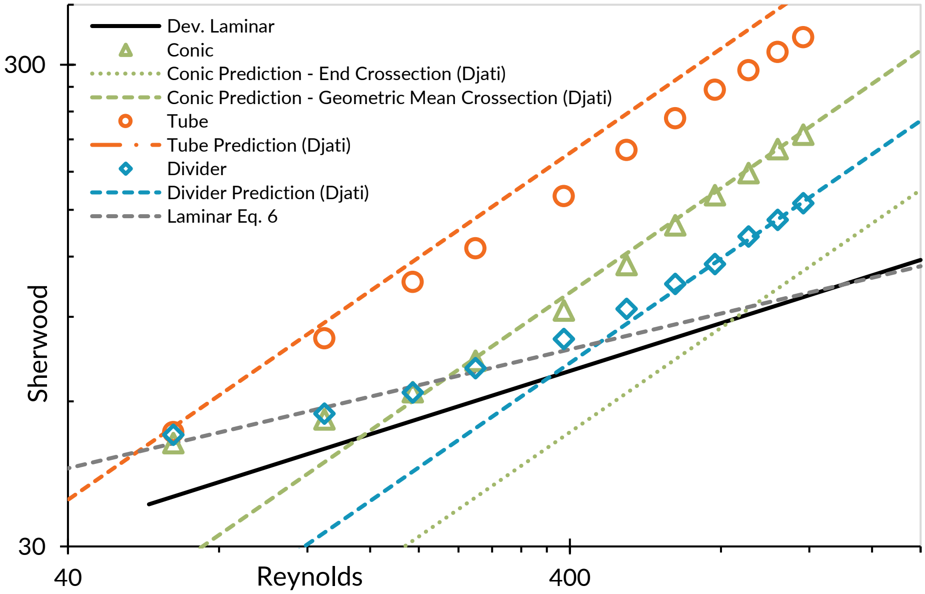

Figure 9: Sherwood-Reynolds plot of the experimental data obtained with the shortest empty channel printed electrolyzer. A divider inlet (Diamonds), conic inlet (Triangles) and tube inlet (Circles) were measured. The full line is the correlation for hydrodynamically developed laminar flow shown in table 4 and eq.3a. Electrolyte data is available in table 3.

Compared to eq.3a a higher rate of mass transfer is observed. This could be due to protrusions resulting from imperfections in the printed parts or the rubber seals between them. Additionally, the Reynolds power in eq.6 is 0.247 compared to the power of 0.33 in eq.3a. The likely reason for this is that the current at low flow rates is not fully stabilized, as shown in figure 2. The effect likely also contributes to the higher performance in eq.6 compared to eq.3a.

In the turbulent region the rate of mass transfer with the conic inlet is a factor 1.4 higher (at Re = 1000) compared to the divider inlet. Mass transfer with the tube inlet is a factor 2.3 higher (at Re = 1000) compared to the divider inlet. This difference is the result of an earlier transition to the turbulent regime, which in turn is caused by the sudden expansion of the inlet to the channel. Djati et al.[21] investigated the effect of these expansions on the rate of mass transfer in slit and tube inlets. They established a correlation using the inlet to channel cross sectional area ratio A_{in}/A_{ch} as a parameter (eq. 6). If $A_{in}/A_{ch} = 1$, no expansion occurs and the equation describes hydrodynamically developed turbulent flow comparable to equation 5a. The difference between eq.7 and eq.5a or eq.5b is small.[21]

$$Sh = 0.068 \left(\frac{A_{in}}{A_{ch}}\right)^{-0.5} Re^{0.72} Sc^{0.33} \qquad \text{eq. 7}$$

In our case, the tube inlet has an area ratio of 0.07. The divider inlet is a series of slits, with the ratio of the area of all openings to the channel being 0.52. The conic inlet ends in the same cross-sectional area as the channel, which implies that the ratio is 1.0. Using these values, eq. 7 results in a good prediction for the divider inlet at Re > 500 (max deviation < 8%) and to a lesser extent the tube inlet (max deviation <18%). For the conic inlet on the other hand the prediction appears to be inaccurate. This is because the ratio of 1.0 implies that there is no expansion, but expansion is occurring in the inlet. Therefore, we used the geometric mean to determine the ratio: $A_{in} = \sqrt{A_{in,0} * A_{in,1}}$, where $A_{in,0}$ is the area at the beginning of the inlet and $A_{in,1}$the area and the end of the inlet. For the conic inlet the area ratio then becomes 0.26. With this ratio, the prediction closely matches the experimental results at Re > 300 (max deviation < 6%)

By finding the intersect of the laminar and turbulent correlations, the Reynolds number at which the transition occurs Re_t can be determined. When combined, and solved for Re, eq.6 and eq.7 lead to eq.8, which gives Re_t as a function of the cross-sectional area ratio of the inlet to the channel.

$$Re_t = 925\left(\frac{A_{in}}{A_{ch}}\right)^{1.06} \qquad \text{eq. 8}$$

Eq. 8 predicts that the flow transition occurs at Re_t = 223 for the conic inlet, Re_t = 463 for the divider inlet and Re_t = 56 for the tube inlet. The transition for the conic and divider inlet are observed in figure 9. For the tube inlet Re_t is near the first datapoint of the graph and therefore the transition cannot be seen. When A_{in}/A_{ch} = 1, no expansion takes place and Re_t = 925. This is far earlier than expected from the work of Ong and Pickett,[14-15] possibly due to the imperfections in the printed parts and the assembly thereof.

3.4.3. 3D printed electrolyzer with different entrance lengths

In figure 10 the effect on mass transfer of adding a calming section between the inlet and the electrolyzer is shown. When no calming section is used, the type of inlet is important as the turbulence generated by it greatly enhances mass transfer. By adding a calming section, this effect is diminished and for a calming section of 550 mm the type of inlet no longer seems to matter. According to eq. 5 the laminar entrance length is 240 mm at the highest Reynolds number measured (Re = 1200). Therefore, it makes sense that an inlet well beyond this distance would no longer influence the mass transfer to the electrodes. Furthermore, the divider type inlet seems to perform similar at any length of calming section. This implies that a good inlet design can enable hydrodynamically fully developed laminar flow.

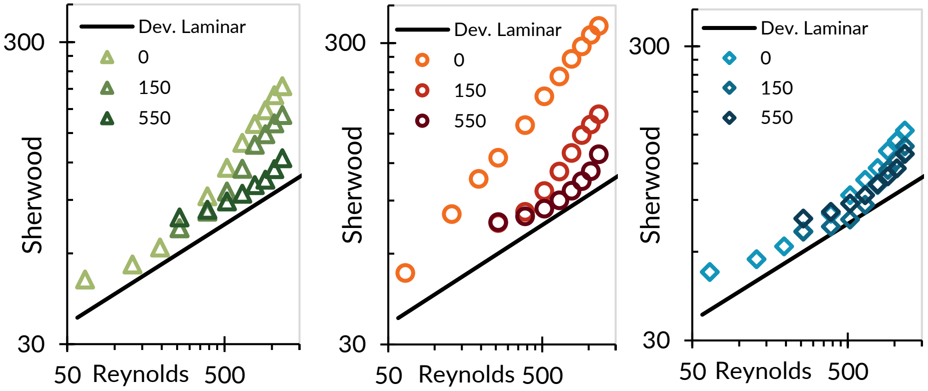

Figure 10: The effect of a calming section on mass transfer with different inlets in the 3D printed electrolyzer (without turbulence promotors). The left figure shows the tube inlet with calming sections of 0mm, 150mm and 550mm, the middle figure the tube inlet and the right figure the divider inlet. The full line in each of these is the correlation for hydrodynamically developed laminar flow shown in table 4 and eq.2. Electrolyte data is available in table 3.

Despite using a 550 mm long calming section, our correlations still do not completely match the hydrodynamically fully developed laminar flow correlation established by Ong at Reynolds numbers below 500. As previously mentioned, an overestimation of mass transfer occurs at low Reynolds numbers, since the current is not fully stabilized after 7 seconds. Apart from this effect, additional experimental error is expected due to the limitations of 3D printing. A first limitation is that due to the print process imperfections may be introduced into the channel wall. These imperfections lead to increased surface roughness, which may result in higher mass transfer and an earlier transition to the turbulent regime. Secondly, because the longest dimension of a print is limited to around 200 mm, the assembly consists out of multiple smaller parts with joints between them. At these joints, minor protrusions may exist that can introduce turbulence.

3.4.4. 3D printed electrolyzer with turbulence promoters

Often, turbulence promoters are added to parallel plate electrolyzers in order to enhance mass transfer.[1,5] This degree of mass transfer enhancement is also widely seen in literature.[2,4-5,20,22,24,26] However, the opposite is observed in the work of Frias ferrer et al.[23], where the turbulence promoter reduces mass transfer. The difference is probably due to the design of the inlet device: the electrolyzer used by Frias-ferrer et al.[23] uses an inlet that causes high turbulence and high rates of mass transfer. A turbulence promoter added to this environment calms down the highly turbulent inlet flow.

In figure 11 the performance is shown of a selection of turbulence promoters in the 3D printed electrolyzer, with and without a 150 mm calming section. The promoters fill the entire empty channel in both configurations (see figure 6). In either case, the turbulence promoters increase mass transfer significantly. The enhancement at Re = 1000 varies between a factor 2.3 and 2.8 without a calming section and between a factor 1.8 and 4.0 with the calming section. Interestingly the variation in enhancement is larger when a calming section is used, despite having similar empty channel performance. A possible explanation is that a secondary inlet effect occurs when the flow first hits the turbulence promoter. In the first few centimeters of the promoter this could result in higher than expected turbulence, which would initially increase the rate of mass transfer. This would explain why promoters such as the tube promoter perform better in the cell without calming section. However, with the small gyroid promoter the opposite effect is observed, as it performs better with a calming section than without. Here it is possible that the divider type inlet is channeling the flow into certain paths in the structure of the promoter, resulting in localized spots with little flow and mass transfer. For the cell without calming section, this would result in lower average mass transfer. With a calming section, this flow channeling is smoothed out before the electrode section is reached and therefore the effect of the localized dead volumes is not seen.

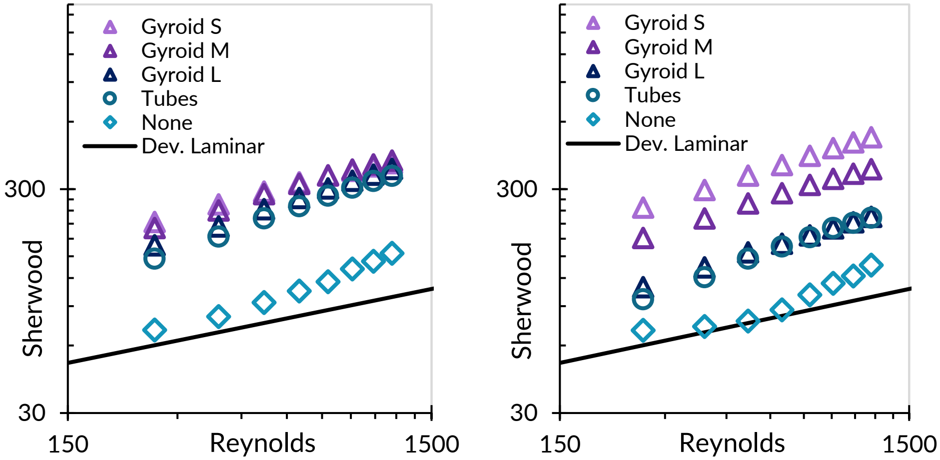

Figure 11: Effect of turbulence promoters on mass transfer, without (on the left) and with (on the right) a 150 mm long calming section. The divider inlet was used in each case. Electrolyte data is available in table 3.

3.4.5. Pressure drop in the printed cell

The pressure drop of the 3D printed electrolyzer without turbulence promoters was small and varied between 2600 ± 200 Pa and 3800 ± 200 Pa at Reynolds 1000 depending on the configuration (see also supporting information figure A1). The highest pressure drop was found for the tube inlet, the lowest for the divider inlet. Since these differences are small, it is likely that their accuracy is strongly affected by the imperfections in the print and the gasket joints between components of the cell. Furthermore, because the pressure drop was measured across the entire electrolyzer, it may be possible that factors such as the placement of the external tubing or the tightness of the fittings lead to further inaccuracy. Turbulence promoters did not significantly affect the pressure drop. For the divider inlet without calming section, the pressure drop at Reynolds 1000 was 2700 ± 200 Pa for every promoter (see also supporting information figure A2). In the cell with divider inlet and a 150 mm calming section, the pressure drop for varied between 2700 ± 200 Pa and 3500 ± 200 Pa for the promoters compared to 2200 ± 200 Pa in the empty channel. Generally, a trend exists wherein the better performing turbulence promoters cause a higher pressure drop, though the difference is small.

3.5. Conclusion

The different design choices made in the construction of an electrolyzer greatly affect the mass transfer performance. Between the electrolyzers found in literature, up to a factor 10 difference is observed (see figure 8). This variation is the result of several different geometric design choices in the electrolyzer. Using a 3D printed electrolyzer, we were able to investigate the effect of some of these choices.

Depending on the type of inlet that was used, up to a factor 2.2 difference in Sherwood numbers was seen. Furthermore, an earlier transition to the turbulent regime was found. The tube inlet already produced turbulent flow at Re = 65, the conic and divider inlet transitioned around Re = 300. The higher than expected mass transfer is due to the sudden expansion of the inlet to the channel. In turbulent flow, the correlation by Djati et al. predicts mass transfer fairly well. [21] This correlation uses the ratio of cross-sectional area of the inlet and channel as parameter to predict the magnitude of expansion turbulence. In the conic inlet, the cross-sectional area varies throughout the inlet and this was accounted for by using the geometric mean cross-sectional area. The correlation deviated from the experimental results by <18% for the tube inlet, <8% for the divider inlet and <6% for the conic inlet.

The addition of a calming section minimized these effects. With a calming section of 550 mm, the type of inlet no longer seemed to affect the rate of mass transfer. This length is over twice the predicted hydrodynamic entrance length of 240 mm at Re = 1200 (based on eq. 5). Therefore, it is reasonable to assume that the flow is fully developed and that the inlets no longer matter. Despite this, our results did not completely match the correlations for hydrodynamically developed flow established by Ong.[14-15] This is likely the result of the limitations of 3D printing, as this process can result in imperfections in the printed parts that may disturb the flow.

Turbulence promotors generally lead to an enhancement of mass transfer. The presence of a calming section significantly changed the enhancement effect of the promoters. Without calming section, most of our promoters resulted in comparable Sherwood numbers, whereas with an entrance length a larger variance in performance was found. Inlet turbulence therefore greatly influences the effect of a turbulence promoter.

The pressure drop was measured for the different configurations of inlet length, inlet type and turbulence promoters. Overall, only very small differences between each configuration were observed (in the order of 100 Pa). Though the difference is marginal, it appears that higher pressure drops result in higher mass transfer rates.

Mass transfer in electrolyzers can be significantly enhanced by turbulence promoters or turbulence causing inlets. The added pressure drop for these is minimal, which implies that large performance increases can be achieved for little extra pumping costs. However, due diligence must be taken in extrapolating results from the lab-scale to the industrial scale. Since the importance of the inlet effect diminishes as the electrolyzer scales up, mass transfer may be slower than expected from the lab-scale. As we have shown, a good inlet design or a calming section can reduce inlet turbulence in smaller electrolyzers, so that they are more representative of their larger counterparts.

Acknowledgements

This project has received funding from Nouryon as part of the HIGHSINC project. We thank Nouryon for their contributions. We thank A.W. Vreman (Nouryon, TU Eindhoven) for the discussions surrounding mass transfer in electrolyzers and assistance in furthering our understanding in the material.

Nomenclature

A = Electrode area, m^2
A_{ch} = Cross-sectional area of the channel, m^2
A_{in} = Cross-sectional area of the inlet, m^2
B = Electrode width (breadth), m
$C_{(III)}$ = Concentration of hexachloroiridate(III), mol/m^3
$C_{(IV)}$ = Concentration of hexachloroiridate(IV), mol/m^3
C_{bulk} = Bulk concentration of the reacting species, mol/m^3
D = Diffusion coefficient, m^2/s
d_H = Hydraulic diameter 2 BS/(B+S), dimensionless
F = Faraday's number, 76485 C/mol
$i_{A,lim}$ = Limiting current density, A/m^2
k_{LS} = Liquid-solid mass transfer coefficient, m/s
L = Electrode length, m
L_{entry} = Hydrodynamic entry length, m
n = number of electrons exchanged, dimensionless
S = Electrode spacing, m
T = Temperature, K
v_0 = Flow velocity over the electrode, m/s

Dimensionless groups

f = Friction factor, dimensionless

J_M =J-factor for mass transfer, dimensionless

Le = Length number (= L/d_H), dimensionless

Re = Reynolds number (= $v_0 d_H/\nu$), dimensionless

Sc = Schmidth number (= ν/D), dimensionless

Sh = Sherwood number (= $k_{LS} d_H/D$), dimensionless

Greek Letters

γ = Electrode aspect ratio (=B/L), dimensionless

ν = Kinematic viscosity, m^2/s

ρ = Density of the electrolyte, kg/m^3

Φ = Geometry parameter for laminar entry length, dimensionless

References

[1] Ralph TR, Hitchman ML, Millington JP, Walsh FC. Mass transport in an Electrochemical Laboratory Filterpress Reactor and its Enhancement by Turbulence Promoters. Electrichim. Acta. 1996;41:591-603.

[2] Rivera FF, Ponce de León C, Walsh FC, JL Nava. The reaction environment in a filter-press laboratory reactor: the FM01-LC flow cell. Electrichim. Acta. 2015;436-462:161

[3] Rivera FF, Ponce de León C, Nava JL, Walsh FC. The filter-press FM01-LC laboratory flow reactor and its applications. Electrichim. Acta. 2015;338-354:163

[4] González-Garcia J, Frias A, Expósito E., Montiel V, Aldaz A. Characterization of an electrochemical pilot-plant filter-press reactor by hydrodynamic and mass transport studies. Ind. Eng. Chem., 2000;1132-1142:39.

[5] Carlsson L, Sandegren B, Simonsson D, Rihovsky M. Design and Performance of A Modular, Multi-Purpose Electrochemical Reactor. J. Electrochem. Soc. 1983;342-345:130.

[6] Rivero EP, Rivera FF, Cruz-Diáz MR, Mayen E, González Ignacio. Numerical simulation of mass transport in a filter press type electrochemical reactor FM01-LC: comparison of predicted and experimental mass transfer coefficient. Chem. Eng. research and design. 2012;1969-1978:90.

[7] Pérez T, Arenas LF, Villalobos-Lara D, Zhou N, Wang S, Walsh FC, Nava JL, Ponce de Léon C. Simulations of fluid flow, mass transport and current distribution in a parallel plate flow cell during nickel electrodeposition. J. Electroanal. Chem. 2020;114359:873.

[8] Mizushina T. The Electrochemical Method in Transport Phenomena. Adv. Heat Transf. 1971;87-161:7

[9] Velasco-Martinez G, Gutiérrez-Granados A, Alatorre-Ordaz A, Rodriguez-Torres I. Methodology for the Characterization of a parallel-plates Electrochemical Reactor. ECS Transact. 2007;1-12:3

[10] Weusten SJC, de Groot MT, van der Schaaf J. A comparative study of the stability of hexachloroiridate and hexacyanoferrate in electrochemical mass transfer measurements. J. Electroanal. Chem., 2020;114512:878.

[11] Szánto DA, Cleghorn S, Ponce-de-Léon C, Walsh FC. The Limiting Current for Reduction of the Ferricyanide Ion at Nickel. AIChE Journal. 2008;802-810:54.

[12] Petrovic S. Cyclic Voltammetry of Hexachloroiridate(IV): An Alternative to the Electrochemical Study of the Ferricyanide Ion. The Chem. Ed. 2000;231-235:5.

[13] Han LS. Hydrodynamic Entrance Lengths for Incompressible Laminar Flow in Rectangular Ducts. J. Appl. Mech. 1960;403-409:27.

[14] Ong KL. Doctoral Thesis: The Influence of Hydrodynamic and mass-transfer entrance effects on the performance of parallel plate electrochemical flow cells.ManChester: Victoria University of Manchester, 1972.

[15] Pickett DJ, Ong KL. The Influence of Hydrodynamic and Mass Transfer Entrance Effects on the Operation of a Parallel Plate Electrolytic Cell. Electrochim. Acta. 1974;875-882:19.

[16] Pickett DJ and Stanmore BR. Ionic mass transfer in parallel plate electrochemical cells. J. of Appl. Electrochem. 2, 1971;151-156.

[17] Tobias CW, Eisenberg M, Wilke CR. Diffusion and Convection in Electrolysis - A Theoretical Review. J. Electrochem. Soc. 1952;359-365:99.

[18] Söhnel O,Novotny P. Densities of Aqueous Solutions of Inorganic Substances. Amsterdam: Elsevier, 1985.

[19] Wolf AV. Aqueous Solutions and Body Fluids, Their Concentrative Properties and Conversion Tables, New York: Harper and Row, 1966.

[20] Brown CJ, Pletcher D, Walsh FC, Hammond JK and Robinson D, Studies of space-averaged mass transport in the FM01-LC laboratory electrolyser. J. Apl. Electrochem., 1993;38-43:23.

[21] Djati A, Brahimi M, Saidani B. Entrance effect on mass transfer in a parallel plate electrochemical reactor. J. Apl. Electrochem. 2001;833-837:31.

[22] Focke WW. On the mechanism of transfer enhancement by eddy promoters. Electrochim. Acta, 1983;1137-1146:28.

[23] Frías-Ferrer Á, González-García J, Sáez V, Ponce de Léon C, Walsh FC. The effects of manifold flow on mass transport in electrochemical filter-press reactors. AIChE Journal, 2008;811-823:54.

[24] Griffiths M, Ponce de Léon C, Walsh FC. Mass transport in the rectangular channel of a filter-press electrolyzer (the FM01-LC reactor). AIChE Journal. 2005;681-687:51

[25] Santos JLC, Geraldes V, Velziarov S, Crespo J. Characterization of fluid dynamics and mass-transfer in an electrochemical oxidation cell by experimental and CFD studies. Chem. Eng. J. 2010;379-392:157

[26] Letord-Quemere MM, Coeuret F, Legrand J. Mass transfer at the wall of a thin channel containing an expanded turbulence promoting structure. J. Electrochem. Soc. 1988;3063-3067:135.

[27] Mizushina T, Ogino F, Oka Y, Fukuda H. Turbulent Heat and Mass Transfer between Wall and Fluid Streams of Large Prandtl and Schmidt Numbers. J. Heat Mass Transf. 1971;1705-1716:14.

[28] Oduoza C, Wragg AA. Effects of baffle length on mass transfer in a parallel plate rectangular electrochemical cell. J. Appl. Electrochem. 2000;1439-1444:30.

[29] Ponce De Leon C, Hussey W, Frazao F, Jones D, Ruggeri E, Tzortzatos S, Mckerracher R, Wills RGA, Yangb S, Walsh FC, The 3D Printing of a Polymeric Electrochemical Cell Body and its Characterisation. Chem. Eng. Trans. 2014;1-6:41.

[30] Wragg AA, Leontaritis A. Local mass transfer and current distribution in baffled and unbaffled parallel plate electrochemical reactors. Chem. Eng. J. 1997;1-10:66

[31] Zhao W, Trass O. Electrochemical mass transfer measurements in rough surface pipe flow. Int. J. Heat Mass Transfer. 1997; 2785-2797:40.

[32] Colli AN, Toulser I, Bergmann MEH, Bisang JM. Mass-transfer studies in an electrochemical reactor with a small interelectrode gap. Electrochim. Acta, 2013;78-84:100.

[33] Oduoza C, Wragg AA. Effects of baffle length on mass transfer in a parallel plate rectangular electrochemical cell. J. Appl. Electrochem. 2000;1439-1444:30.

[34] Hammond JK, Robinson D. Mass transport studies in filterpress monopolar (FM-Type) Electrolysers. Dechema-Monographs, 1991;279-295:123

[35] Qi J, Savinell R. Mass transfer in a laminar-flow parallel plate electrolytic cell with simultaneous development of velocity and concentration boundary layers. J. Appl. Electrochem., 1990;885-892:20.

[36] Colli AN, Bisang JM. Mass-transfer characterization in a parallel-plate electrochemical reactor with convergent flow. Electrochim. Acta, 2013;575-582:113.

[37] Rodriguez A, Rivera FF, Orozco G, Carreno G, Castaneda F. Analysis of inlet and gap effect in hydrodynamics and mass transport performance of a multipurpose electrochemical reactor: CFD simulation and experimental validation. Electrochim. Acta, 2018; 520-532:282.

[38] Arenas LF, Ponce de León C, Walsh FC. Critical Review - The Versatile Plane Parallel Electrode Geometry: An Illustrated Review. J. Electrochem. Soc. 2020;023504:167

Supporting information

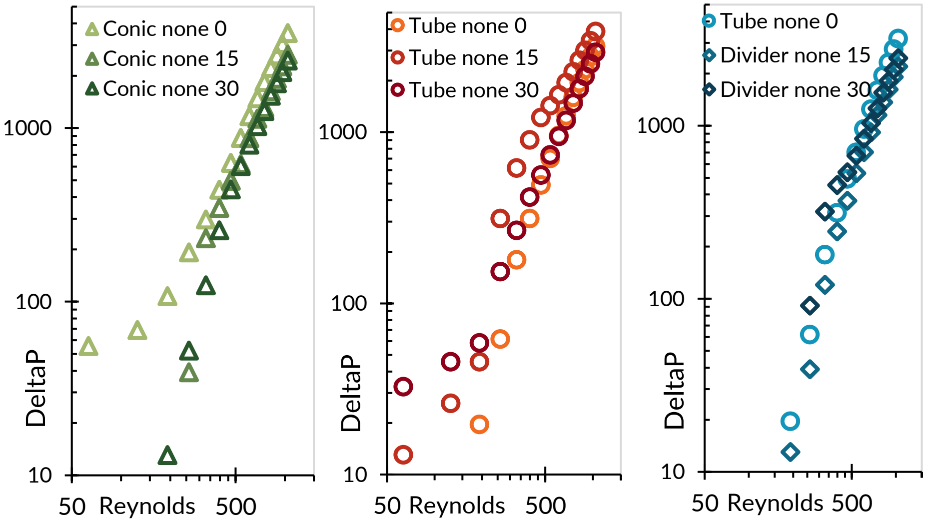

Figure A1: Logarithmic plot of the pressure drop versus the Reynolds number for different inlets of the printed electrolyzer at different entrance lengths. Left: tube inlet with entrance lengths 0mm, 150mm and 300mm. Middle: the tube inlet. Right: divider inlet. Pressure drop measurements were performed with water and no electrolyte.

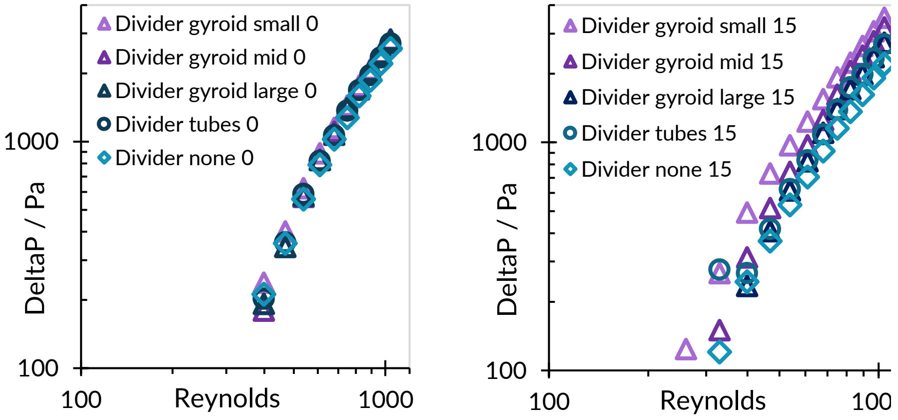

Figure A2: Effect of turbulence promoters on the pressure drop, with (on the right) and without (on the left) a 150mm long calming section. The divider inlet was used for both graphs. Electrolyte data is available in table 3.

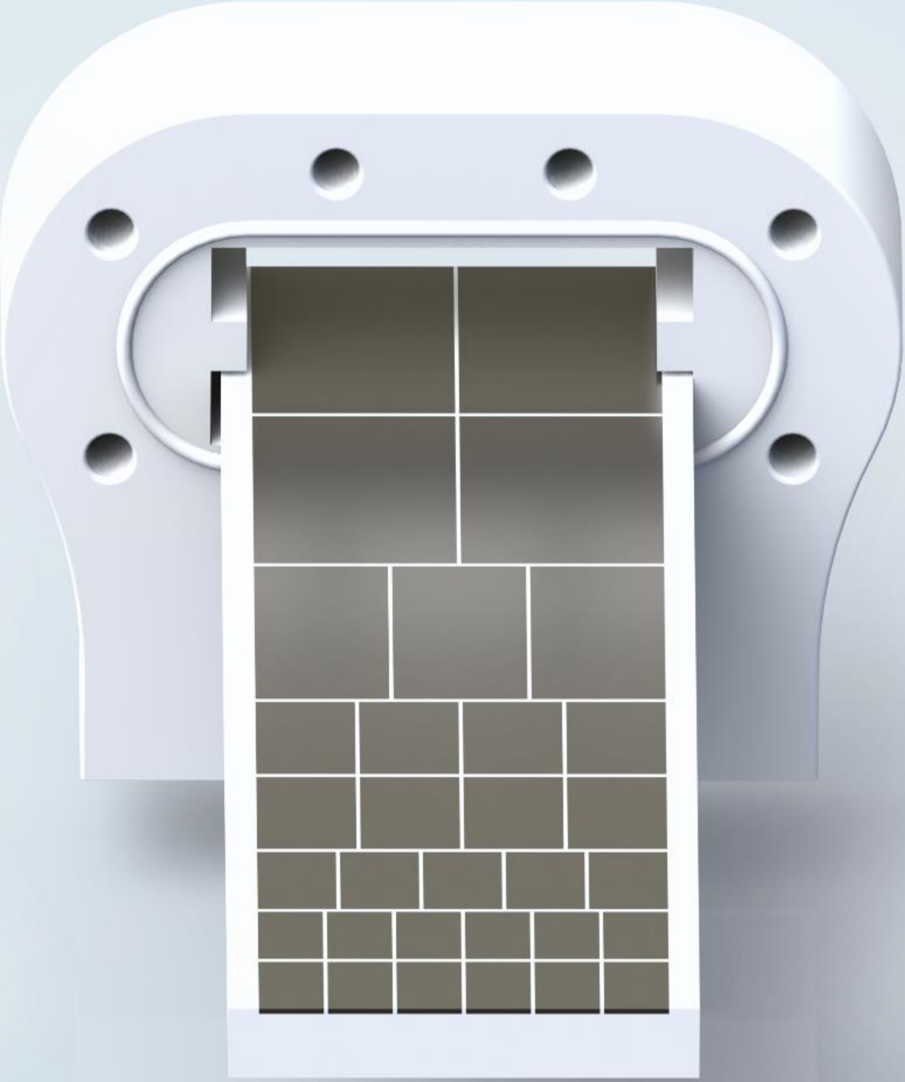

The effect of inlet design and developing flow on local mass transfer in electrolyzers

S.J.C. Weusten, L.C.E.M. Murrer, J. van der Schaaf, M.T. de Groot

4 - Abstract

The mass transfer performance of electrolyzers can vary significantly depending on the type of inlet that is used. Furthermore, significant local effects can occur if the flow is not distributed well by the inlet. In this work, these local effects are investigated using segmented electrodes. Three different segmentation patterns were used: a series, matrix and focused pattern. It was found that the cross-sectional area ratio of the inlet to the channel is indicative of the degree of non-uniformity in local mass transfer. For a tube inlet, regions of low and high mass transfer are prevalent due to the formation of a jet and the resulting flow recirculation. A conic inlet resulted in significant flow channeling to the sides of the electrolyzer. These local effects were reduced significantly by using a divider inlet, or the addition of a calming section. The type of inlet also determines the flow regime in the electrolyzer: with the extended conic configuration the flow is developed laminar, whereas with the tube inlet the flow is developing turbulent. The other inlets show local variations in flow regimes that depend on the Reynolds number. In contrast the use of turbulence promotors results in negligible inlet effects and uniform mass transfer.

Image: The focused segmentation pattern

4.1. Introduction

The mass transfer performance of an electrolyzer is crucial to its overall productivity and therefore, much work has been done in the past regarding the subject.[1-7] For a large number of parallel plate electrolyzers, correlations are available that describe their mass transfer performance (expressed as the Sherwood number) as a function of flow rate (expressed as the Reynolds number). [8-12] Between these reactors, there is a large variance in mass transfer performance as a result of the differences in cell and inlet geometry.

The mass transfer performance of these reactors is significantly higher than expected from correlations for hydrodynamically developed laminar and turbulent flow as established by Pickett et al. (eq.1 and eq.2).[1,3,8,13] These equations represent the mass transfer performance in electrolyzers with a well-developed flow profile as established in experiments with a calming section prior to the electrolyzer.[3] In practice, though, such calming section are not used and inlet effects and the resulting hydrodynamically developing flow can lead to significantly higher mass transfer rates.

Developed laminar flow: [1,3]

$$Sh = 1.467\left(\frac{2}{1+\gamma}\right)^{0.33}\left(Re\,Sc\,\frac{d_H}{L}\right)^{0.33} \qquad \text{eq. 1}$$

Developed turbulent flow: [3]

$$Sh = 0.023\,Re^{0.8}Sc^{0.33} \text{ for } Le > 12 \qquad \text{eq. 2a}$$

$$Sh = 0.125\,Re^{0.66}Sc^{0.33}Le^{-0.25} \text{ for } Le < 10 \qquad \text{eq. 2b}$$

In previous work we investigated how inlet effects influence the average mass transfer performance by comparing different inlet types.[13] The results suggested that the inlet induces an earlier transition to the turbulent regime, which in turn causes increased mass transfer. Several studies on the topic can also be found in the literature.[14-16] Among those is the work of Djati et al., which established a mass transfer correlation for electrolyzers with slit and tube inlets (eq. 3).[14]

$$Sh = 0.068 \left(\frac{A_{in}}{A_{ch}}\right)^{-0.5} Re^{0.72} Sc^{0.33} \qquad \text{eq. 3}$$

In this correlation the mass transfer rate depends on the ratio between A_{in} (cross-section of the inlet) and A_{ch} (cross-section of the channel). This correlation also proved to be valid for our printed electrolyzer and its divider, conic and tube inlets.[13] Though in case of the conic inlet, the geometric mean cross-section of the inlet should be used to for A_{ch}.

A weakness of nearly all existing mass transfer correlations is that they are space averaged. Yet, on a local scale there can be significant differences due to inlet effects, local turbulence and dead zones. For practical applications it is important to understand the local scale in order to avoid a non-uniform current distribution, which can lead to regions of the electrode degrading faster than others. There are several experimental studies on the local scale, however, most do not present correlations.[16-19] The correlations that do exist for local mass transfer are typically one-dimensional in the direction of the flow.[20] Numerous CFD studies have been performed to give insight into such localized effects.[21-25] However, these studies are typically validated using space-averaged experimental data and therefore it is unclear whether they adequately describe local behavior.

The aim of this work is to investigate the effect of different inlet manifolds on mass transfer on a local scale. For this purpose, a 3D printed electrolyzer is used, which can be equipped with three different segmentation patterns and inlet types. [13,26] Additionally, the effect of a gyroid type turbulence promoter is evaluated.

4.2. Experimental

The 3D-printed electrolyzer shown in previous work was used. [13,26] The dimensions are shown in table 1. The electrode module was modified to fit the nickel segmented working electrodes. The counter electrode was a flat nickel plate. Three different segmentation patterns were used, namely a series, matrix and a focused pattern. These are shown in figure 1. The four different inlet configurations shown in figure 2 were used: (unextended) conic, (unextended) tube, (unextended) divider and extended conic. No calming sections were used for the conic, tube and divider inlet configurations. For the extended conic configuration a 30 cm long calming section was used. Together these components form the 3D printed electrolyzer (see also figure A1), with the geometric details shown in table 1.

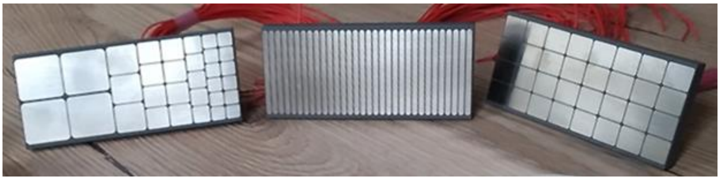

Figure 1: Segmentation patterns of electrode. left: focused, middle: series, right: matrix. The electrodes are installed in such a way that the flow crosses the electrodes from the right to the left.

The segmented electrode module was built by a combination of techniques. The electrode segments were cut from a 0.5 mm thick nickel sheet using wire EDM (electrical discharge machining). These segments were then placed onto a CNC milled PVC support, and affixed using epoxy glue. Wires were soldered onto the back of the electrode plate, and covered using epoxy resin. The front side of the electrode was machine polished to form a smooth surface between the electrode and the support. The electrode assembly was then placed and epoxy glued into a 3D printed ABS part. The ABS part contained the outside electrical connections and screw holes for the 3D printed electrolyzer.

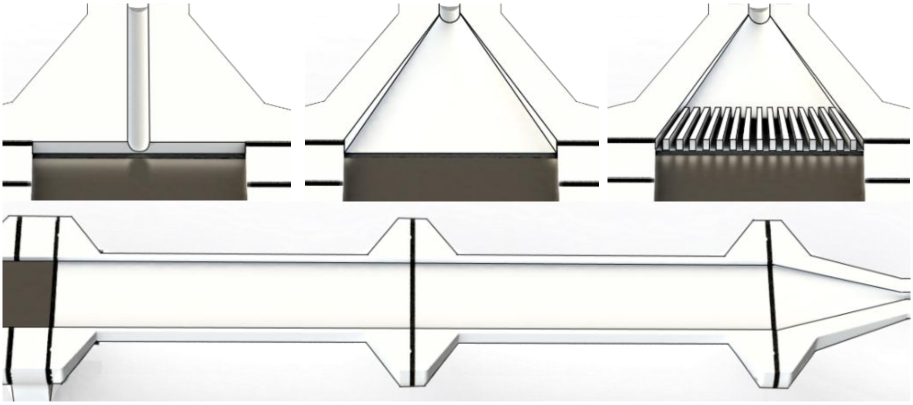

Figure 2: Rendered cutout images of the inlet configurations of the 3D printed electrolyzer. Top left: tube inlet, top middle: conic inlet, top right: divider inlet, bottom: extended conic configuration. The black stripes are the rubber gaskets between different printed components. For the top three configurations, photographs can be found in previous work. [13]

Table 1: Geometric details of the electrolyzer used in this work

Symbol	Property	Value
$\boldsymbol{L}$	Electrode length	10 cm
$\boldsymbol{B}$	Electrode width (breadth)	4 cm
$\boldsymbol{S}$	Electrode spacing	0.5 cm
$\boldsymbol{A}$	Electrode area	40 cm^2
$\boldsymbol{\gamma}$	Electrode aspect ratio B/L	0.40
$\boldsymbol{d_H}$	Hydraulic diameter 2*B*S/(B+S)	0.89 cm
$\boldsymbol{Le}$	Length number L/d_H	11.25

In Figure 3, a schematic of the setup is shown. Electrolyte was continuously recirculated through the electrolyzer using a gear pump (Tuthill). The flowrate was measured using a variable area flowmeter (Swagelok). The electrolyte was stored in a glass storage vessel. This vessel was continuously flushed with nitrogen to remove dissolved gases such as oxygen. The bulk concentration of hexachloroiridate(IV) in the electrolyte was measured by an inline UV-VIS flow cell (Avantes) shortly before the entrance of the reactor.

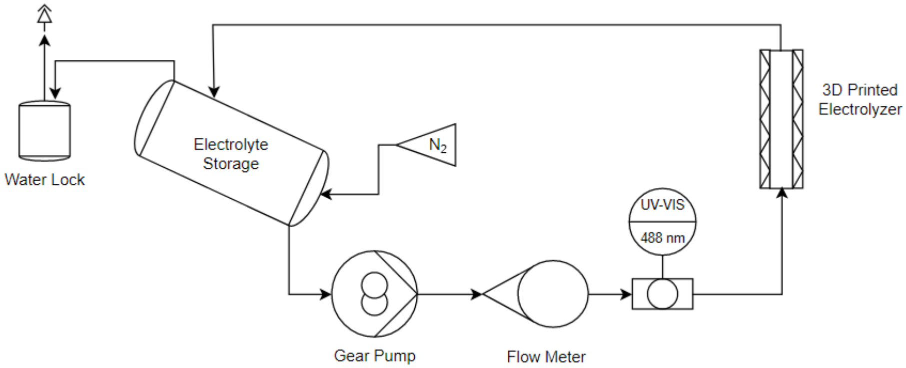

Figure 3: Schematic of the experimental setup.

The limiting current density method was used to measure the rate of mass transfer. For this purpose, the hexachloroiridate(IV)/hexachloroiridate(III) redox couple was used.[27] The concentration of the redox couple was 0.5 mM hexachloroiridate(IV) (>99.9%, Merck/Alfa Aesar) and 1.0 mM hexachloroiridate(III) (>99.9%, Merck/Alfa Aesar). The supporting electrolyte was 0.5 M KNO3 (>99%, VWR). A 0.1 M mix of potassium acetate (>99%, VWR) and acetic acid (>99%, VWR) was used to maintain a solution pH of 4. The electrolyte properties are listed in table 2.

The pretreatment procedure outlined by Szánto et al. in their recommendations was followed.[30] Before assembly of the reactor, the electrodes were polished using an ascending series of grit sizes of sandpaper (namely 400, 800, 1200 and 2000). A suspension with alumina particles was used as polishing fluid (respectively 1.0 µm, 0.3 µm and 0.05 µm). The electrodes were then rinsed and sonicated two times for 15 minutes. Once assembled, the reactor was filled with 0.5 M KOH solution (prepared from dissolving solid pellets, >99.9%, VWR) and the segmented working electrode was set to evolve hydrogen for 15 minutes. The setup was then filled with a solution of 0.1 M pH 4 and 0.5 M KNO_3, and the baseline for the UV-VIS was measured. The setup was then emptied and flushed using nitrogen. The electrolyte solution containing hexachloroiridate was then added and bubbled through with nitrogen for 10 minutes in order to remove dissolved gases.

Table 2: Physical properties of the electrolyte, relevant constants

Symbol	Property	Value
ρ	Density of the electrolyte	1029.8 kg/m^3 [28,29]
ν	Kinematic viscosity	$9.52*10^{-7}$ m^2/s [29]
T	Temperature	298 K
$C_{(III)}$	Concentration of hexachloroiridate(III)	1.0 mol/m^3
$C_{(IV)}$	Concentration of hexachloroiridate(IV)	0.5 mol/m^3
D	Diffusion coefficient of hexachloroiridate(IV)	$8.38*10^{-10}$ m^2/s [27]
Sc	Schmidt number of the electrolyte	1011

The chronoamperometric measurements were obtained using an Ivium Compactstat connected to a single MultiWE32 module. A two-electrode setup was used. The measurements were performed at a constant cell potential of -0.8 V across all electrode segments. The measurement itself consisted of a 20 second or longer stabilization period, and a 10 second measuring period. The purpose of the stabilization period was to allow the current to settle to a constant value. At lower flowrates, this occurred more slowly, therefore the stabilization time was increased to 50 seconds. Baseline measurements were taken at 0 L/h in order to determine the deviation in current density between segments. For this purpose, a 50 second stabilization time was used followed by a 10 second measuring time. The results in figure A3 show that some variation between segments was found possibly caused by surface irregularities. Although relatively small compared to the current densities measured in the experiments, it could explain why we sometimes see significant scatter in the experimental data, especially for the focused segmentation pattern.

4.3. Results and discussion

4.3.1. Space averaged mass transfer performance of segmented electrodes

In Figure 4 the space-averaged mass transfer performance of the segmented electrodes is shown alongside the flat plate electrode reported earlier for different inlet configurations.[26] The mass transfer results are consistent across the different segmentation patterns. Generally, results for the segmented electrode fall within 15% of the flat plate performance. Typically, the results for the flat plate are found in the middle of the range of segmented electrode data, though there is some variance. For the tube inlet at low flow rates the flat plate performance is slightly lower, for the extended conic configuration, it is slightly higher. However, no systematic under- or overperformance is observed. There also does not appear to be a significant effect from the segmentation itself. Such a segmentation effect could potentially result from the inert breaks between different electrode segments that can lead to partial dissipation of the boundary layer and increased mass transfer in the next segment.[16] Presumably, the inert breaks are sufficiently small (approximately 0.1 mm) to avoid significant enhancements in mass transfer from this partial boundary layer dissipation.

The data in figure 4 show both laminar as well as turbulent regions. The divider inlet at Re <400 and the extended conic configuration show a small slope with a power b of 0.33 indicative of laminar flow. Here eq.1 (Pickett et al.) offers a good description for the slope, but systematically underpredicts the rate of mass transfer by about 20%.[1,3] The difference is likely due to imperfections and irregularities as a result of the 3D printing process.

For the tube inlet, the conic inlet and the divider inlet at Re > 400 a higher slope with a power of ~0.7 is found. Normally, a high slope is characteristic of turbulent flow. However, because of the low Reynolds numbers (Re < 2000), the slope alone is insufficient evidence to claim that the flow is fully turbulent. The apparently high slope could also be caused by laminar recirculation streams, localized or residual turbulence or because the flow is in a transitional regime. The mass transfer performance significantly exceeds the correlations for developed turbulent flow given in eq. 2a and 2b. This can be explained by the fact that the flow profile is not yet fully developed enhancing the mass transfer. Instead the mass transfer performance is predicted fairly well by eq.3 (Djati et al.),[14] in which the mass transfer enhancement due to the inlet effect depends on the ratio of the cross-sectional surface area of the inlet A_{in} and the channel A_{ch}. [13]

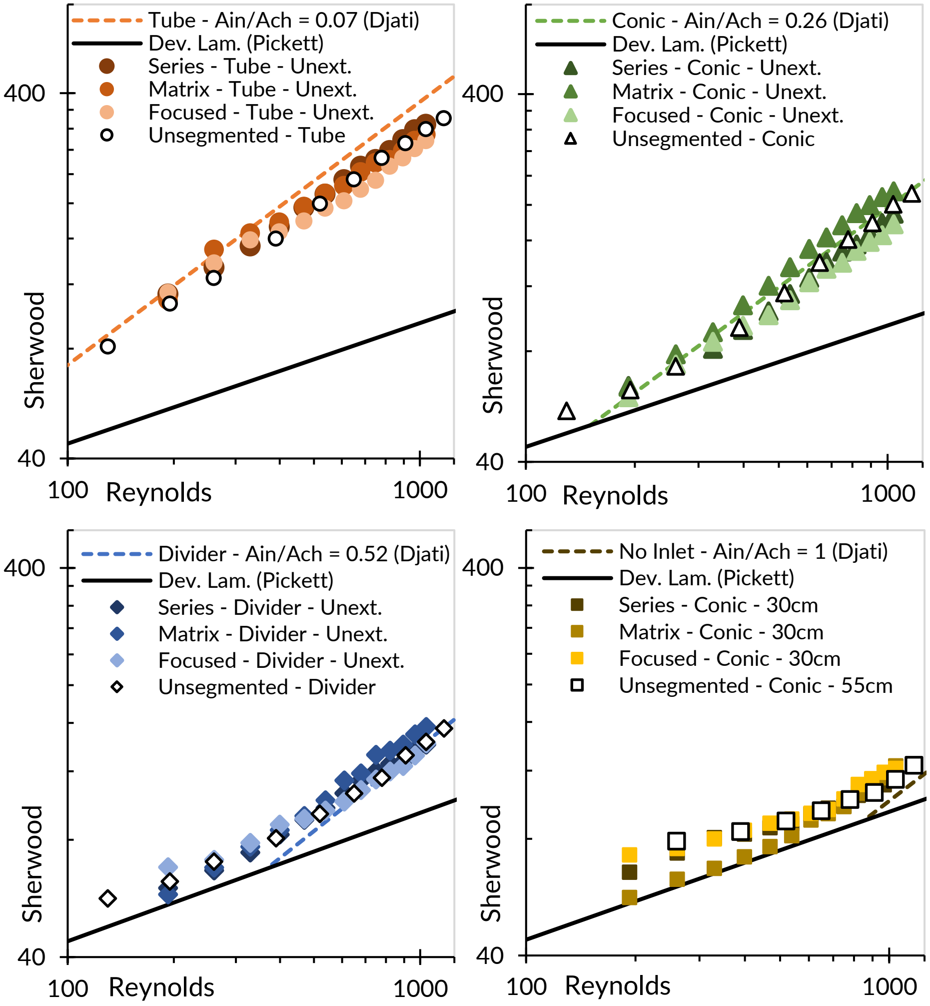

Figure 4: Space averaged mass transfer of the printed electrolyzer with different inlet configurations and segmentation patterns. Top left: tube inlet, top right: conic inlet, bottom left: divider inlet, bottom right: extended conic inlet. The segmentation patterns are shown as different shades: the series pattern is always the darkest shade, the matrix pattern is the intermediate shade and the focused pattern is the lightest shade. The flat plate electrode results reported previously are shown as black edged, white filled symbols.[26] *The empirical mass transfer correlations as suggested by Djati (eq. 3)*[14] *are plotted as dashed lines for the different inlets using the area ratios (tube: A_{rat} = 0.07, conic : A_{rat} = 0.26, divider: A_{rat}= 0.52, extended conic A_{rat} = 1). Finally, a full black line is added for fully developed laminar flow, i.e. eq. 1. Electrolyte data is available in table 2 and the dimensions of the printed electrolyzer is available in table 1.*

4.3.2. Local mass transfer

In figure 5a-6d, the local Sherwood numbers are shown for the four inlet combinations and three segmentation patterns for a Reynolds number of 399. These Sherwood numbers have been determined from the measured limiting current densities (see also figure A2, A3 and A4). Since the local flow velocities are not known, the Reynolds number is based on the average flow.

When comparing the results of the three segmentation patters for the same inlet, they generally show comparable behavior, but there are some differences. For instance, with the conic inlet there is a distinct region of high mass transfer at the left with the matrix pattern that cannot be seen with the focused pattern. This is likely because of small variations in the construction of the electrode. Due to the manual method of assembly and 3D printed support, there are unavoidable non-identicalities. These are tiny features (<200 μm) close to the wall or at the edges of the object. Though small, they can have an effect on mass transfer and as a result they could explain the observed differences. This shows how susceptible the flow pattern and resulting mass transfer is to minor perturbations. It also means that we have to be careful with interpretation of the absolute local values. Yet, the data can still be effectively used to discern trends.

The figure shows that there is significant local variation in two directions for all inlet types. Differences in the x-direction (bottom to top, parallel to the flow) are most easily seen using the series segmentation pattern. Except for the tube inlet, the highest rates of mass transfer with this pattern are found close to the leading edge (i.e. at x = 0 mm) of the electrode. This is expected, as the boundary layers are thinnest close to this edge and similar behavior is seen in literature.[16-18,20] For the tube inlet, mass transfer is highest slightly further downstream (at x = 25 mm). From the x-direction alone it is difficult to determine the reason for this, but from the results for the matrix and focused patterns, it becomes clear that there is a narrow region of very high mass transfer starting from the bottom middle {x = 0 mm, y = 0 mm} to the middle right (matrix, {x = 50 mm, y = 15 mm}) or middle left (focused, {x = 40 mm, y = -15 mm}). This region is likely the result of a jet originating from the tube inlet. Initially, this jet is narrow and therefore only a small region of the electrode shows high mass transfer rates caused by the locally high flow velocities. As this jet dissipates into the channel, it results in wider vortices and therefore a broader region of high mixing and mass transfer. In the series pattern, only the latter, broader region is seen due to the y-direction averaging. Presumably, it is this region that is causing the elevated mass transfer at x = 25 mm for the series pattern. This clearly shows that only studying the mass transfer in the x-direction does not offer a full picture of the local mass transfer behavior.

Figure 5a-6d show notable differences in local mass transfer depending on the type of inlet that is used. With the extended conic configuration, Sherwood numbers are relatively low showing a gradual decrease in the x-direction with limited variation in the y-direction. In contrast, for the tube inlet Sherwood numbers are much higher and show a large variation in both x and y-direction. In the work of Gerber et al., a local distribution was found that is similar to that of the extended conic configuration.[18] In their cell, the flow is evenly distributed across the entire electrode, resulting in minimal differences in local mass transfer. Conversely, in the work of Wragg et al., significant local variations were observed as a result of jets emanating from the inlet nozzles.[17] As a result it is clear that the local mass transfer behavior strongly depends on the inlet configuration. Generally, there is a trend where the largest expansion (i.e. the smallest A_{in}/A_{ch}) results in the largest Sherwood numbers and largest local variations. This can be easily seen by comparing the tube inlet (A_{in}/A_{ch} = 0.07) to the divider inlet (A_{in}/A_{ch} = 0.52).

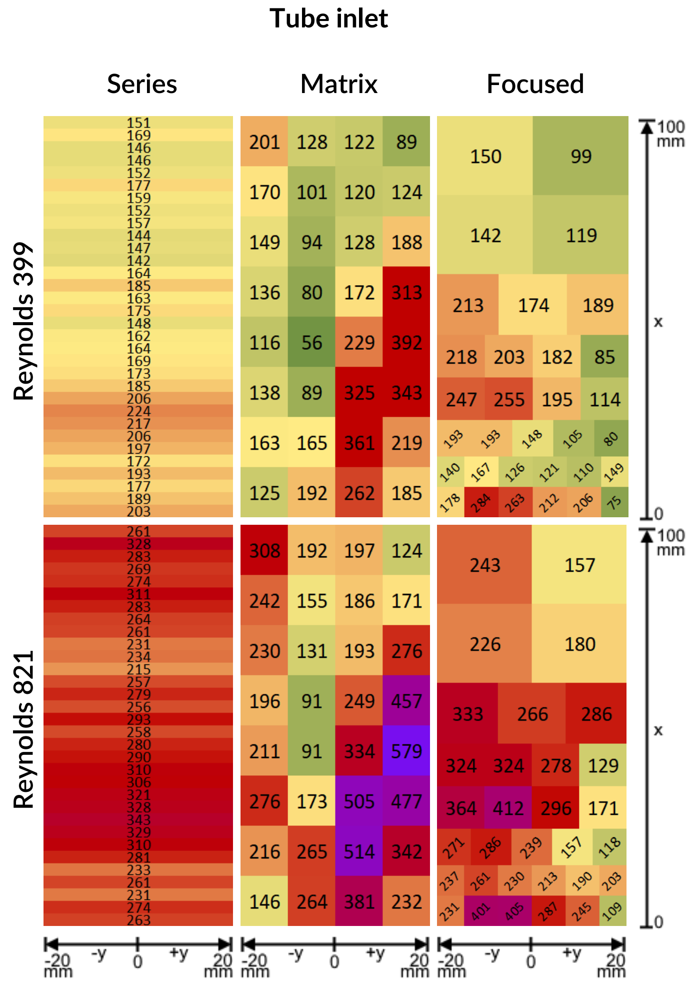

Figure 5a: Local mass transfer in the printed reactor with tube inlet at Re = 399 and Re = 821. The data is shown in colored rectangles ranging from green to yellow and then red and purple for respectively low, intermediate, high and very high Sherwood numbers. These colored rectangles represent the approximate location of the segment. Electrolyte properties are found in table 2, properties of the reactor are found in table 1. Additional data at Re = 821 is found in the supporting info (figure A1).

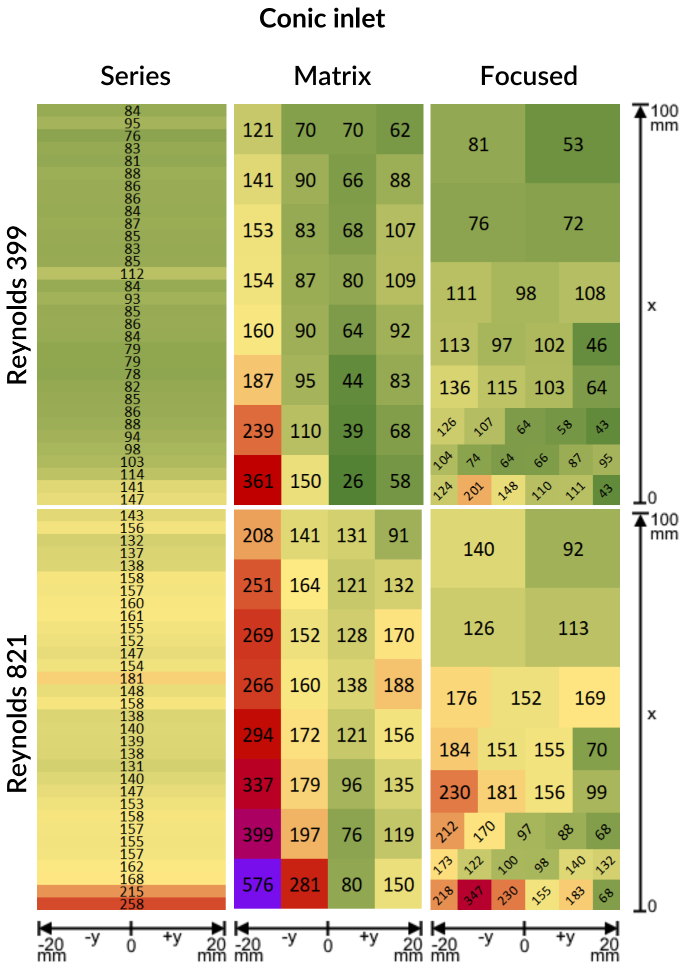

Figure 5b: Local mass transfer in the printed reactor with conic inlet at Re = 399 and Re = 821. The data is shown in colored rectangles ranging from green to yellow and then red and purple for respectively low, intermediate, high and very high Sherwood numbers. These colored rectangles represent the approximate location of the segment. Electrolyte properties are found in table 2, properties of the reactor are found in table 1. Additional data at Re = 821 is found in the supporting info (figure A1).

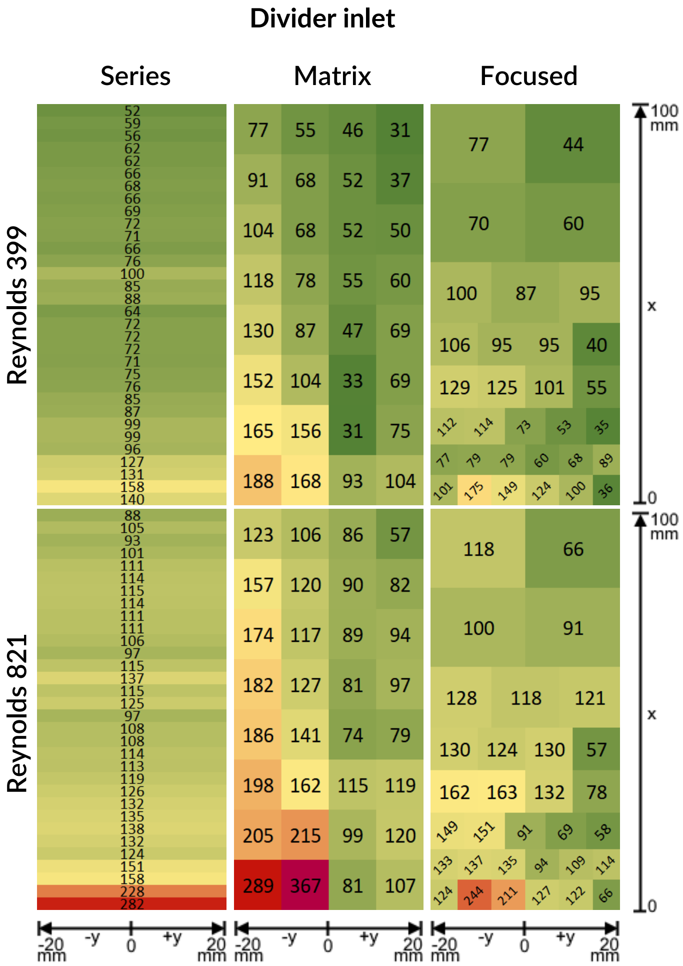

Figure 5c: Local mass transfer in the printed reactor with divider inlet at Re = 399 and Re = 821. The data is shown in colored rectangles ranging from green to yellow and then red and purple for respectively low, intermediate, high and very high Sherwood numbers. These colored rectangles represent the approximate location of the segment. Electrolyte properties are found in table 2, properties of the reactor are found in table 1. Additional data at Re = 821 is found in the supporting info (figure A1).

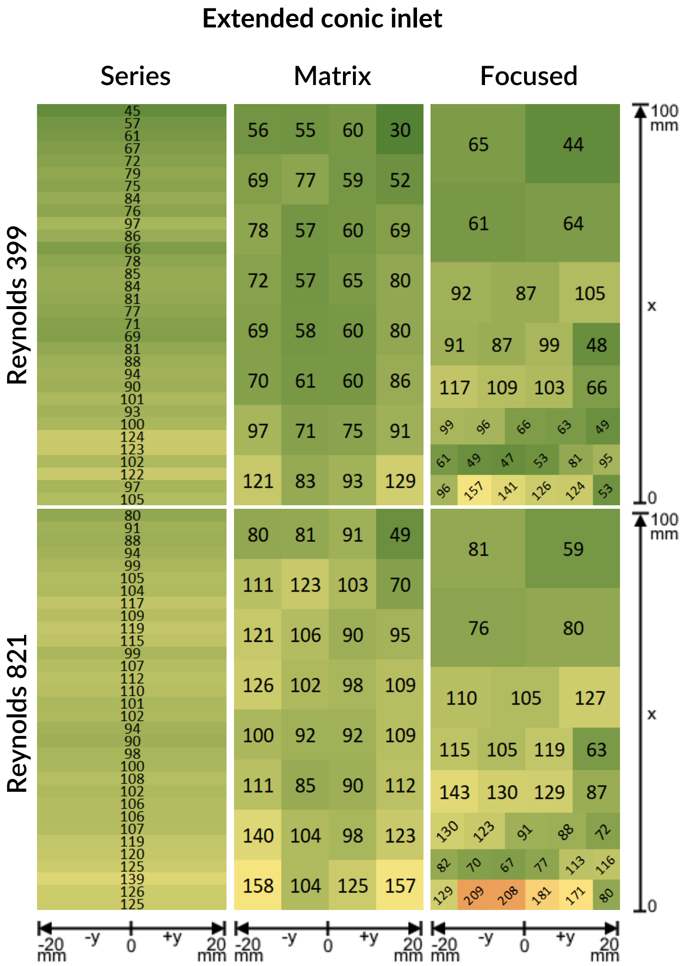

Figure 5d: Local mass transfer in the printed reactor with extended conic inlet at Re = 399 and Re = 821. The data is shown in colored rectangles ranging from green to yellow and then red and purple for respectively low, intermediate, high and very high Sherwood numbers. These colored rectangles represent the approximate location of the segment. Electrolyte properties are found in table 2, properties of the reactor are found in table 1. Additional data at Re = 821 is found in the supporting info (figure A1).

For each inlet there are some clear flow patterns that seem to develop. These are schematically depicted in Figure 6. As mentioned earlier, the tube inlet results in a jet flow with high mass transfer starting from the leading edge (at {x = 0 mm, y = 0 mm}), which continues to the left or right. Interestingly, the jet is not centered and therefore asymmetrical. Moreover, the jet moves in a different direction in the matrix and focused pattern. Both phenomena could result from the small non-identical features of the cell as mentioned earlier. Furthermore, in the matrix pattern a distinct zone of low mass transfer appears in the center left. This is likely the eye of a recirculation stream covering the entire electrode. A similar local distribution was observed in the unbaffled cell used by Wragg et al.[17] In the focused pattern, this low mass transfer zone is not seen. There the turbulence caused by the jet appears to dissipate more evenly.

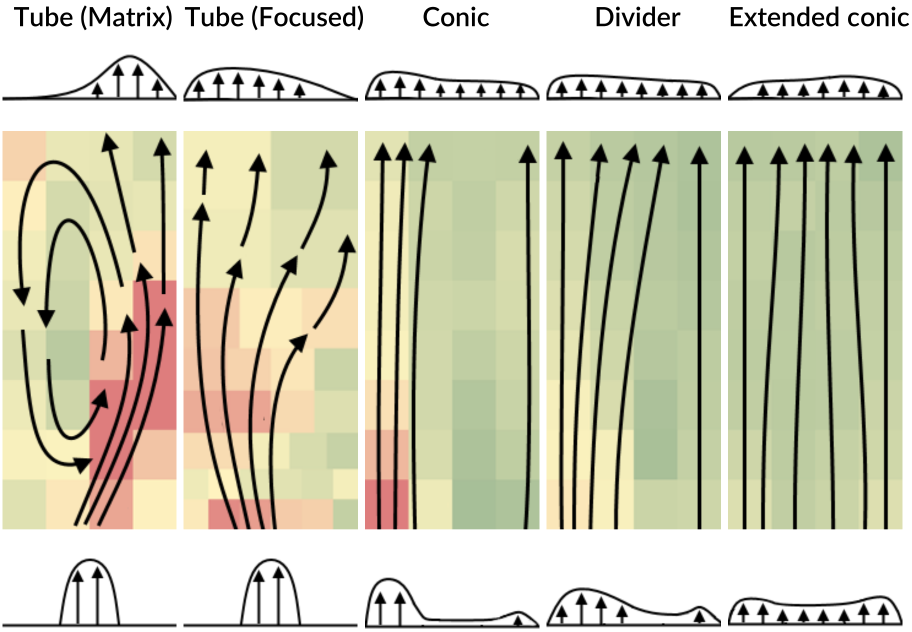

Figure 6: Sketches of hypothetical flow patterns that could lead to the observed mass transfer patterns. On the top and bottom hypothetical velocity profiles are drawn. The patterns are constructed using data at Reynolds 399, which is shown in the background of the sketch. The tube (matrix) and tube (focused) results are shown separately due to different mass transfer behavior.

For the conic inlet, the leftmost segments display increased mass transfer, especially for the matrix pattern. The flow seems to preferentially channel through the left most side of the cell. This channeling was confirmed visually by removing the exit manifold of the electrolyzer, and flowing water through it. We could clearly see that most of the water flowed out of the left side of the electrolyzer. To a lesser extent, the matrix pattern shows that there is a second channeling stream on the right side of the electrolyzer. Though less pronounced, similar behavior is seen for the divider inlet. This type of channeling close to the walls has also been reported by Brown et al. for the FM01-LC electrolyzer.[16] It is therefore possible that it is a more common characteristic of lab-scale electrolyzers.

For the extended conic configuration, a fairly uniform mass transfer is found throughout the cell with a gradual decrease in the x-direction and limited variation in the y-direction. The results show that the addition of a calming section significantly increases the uniformity of mass transfer. Compared to the conic inlet, a much more uniform profile is obtained. At higher Reynolds numbers, similar patterns are observed. In the case of the tube inlet, the jet flow becomes more violent due to the higher flow rates involved. Likewise, the flow channeling in the divider and conic inlet becomes even more apparent, while the extended conic configuration maintains its uniformity even at high flow rates.

More experiments with the series segmentation pattern were carried out to obtain a better understanding of the differences between hydrodynamically developing and fully developed flow. In Figure 7, local Sherwood numbers are shown as a function of the x-distance from the leading edge of the electrode for different Reynolds numbers. The distribution of mass transfer varies greatly depending on the inlet configuration. The tube inlet results in a relatively chaotic distribution as a result of the previously described jet flow, whereas the conic and divider inlets follow a pattern with an initial peak in mass transfer. Interestingly, the initial increase in mass transfer rate is not seen for the extended conic configuration, which only shows a slight decrease in mass transfer over the complete length of the cell. This suggests that the increase in mass transfer for the conic and divider inlet is primarily a result of the development of the hydrodynamic boundary layer, which is already mostly developed for the extended conic configuration. It should be noted that for all inlets, there is a small increase in the Sherwood number for the segments around x = 55 mm. This is can probably be explained by irregularities in these segments.

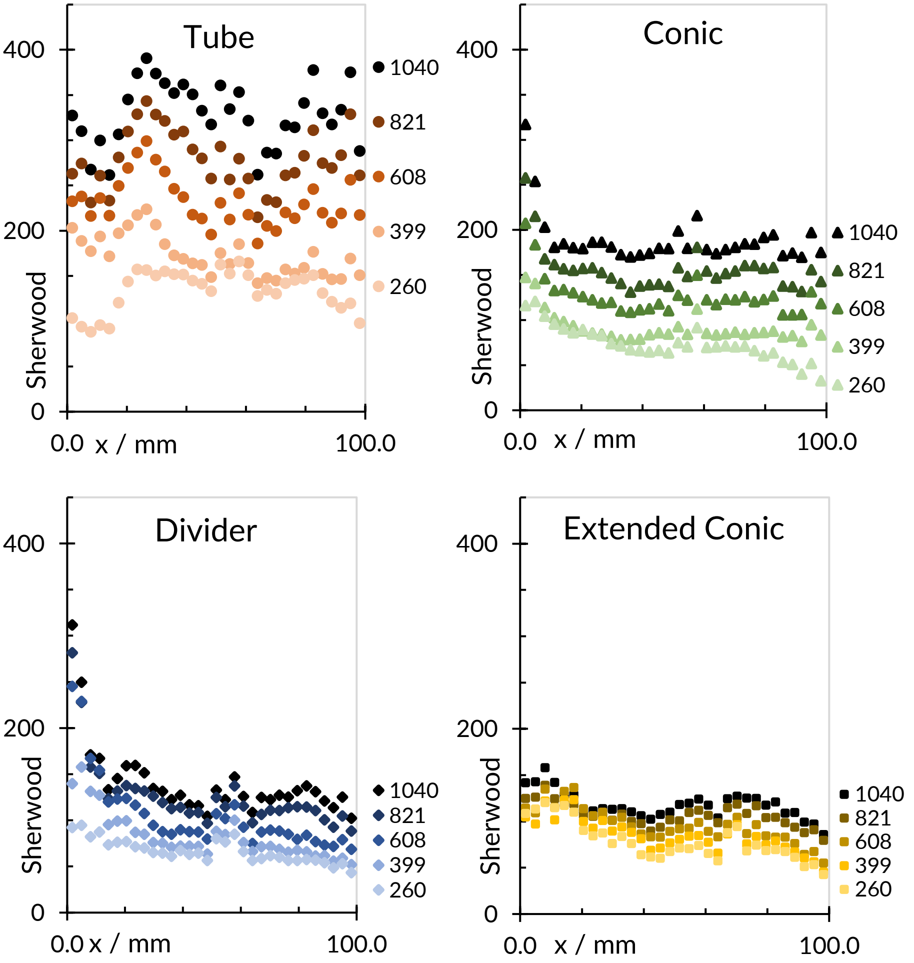

Figure 7: One-dimensional mass transfer as observed using the series segmentation pattern. The four different inlet configurations are shown: top left: tube (red circles), top right: conic (green triangles), bottom left: divider (blue diamonds), bottom right: extended conic (yellow squares). Data is shown at four different Reynolds numbers, which are listed on the right side of each graph. Data points are shaded light to dark in ascending order of the Reynolds number (low to high). Electrolyte data and electrolyzer properties are given in table 1 and 2.

4.3.3. Hydrodynamically developing and fully developed laminar flow

The slope of the Reynolds-Sherwood plot shown in Figure 4 suggests that laminar behavior is seen for the divider inlet (at Re <400) and extended conic configuration (for all measured Reynolds numbers). Figure 7 does not show any significant difference between these inlets at Re = 260 (see also figure A5-A6), despite the difference in hydrodynamic entry lengths between both inlets. This suggest that for laminar flow the influence of hydrodynamically developing flow is limited. Conversely, the effect of the developing diffusive layer appears to be important, as there is a steady decrease of the Sherwood number over the full length of the electrode for both inlets.

Typically, experimental correlations for laminar diffusively developing flow follow the form given in eq.6, where a, b and d are fitting constants.

$$Sh_x = a\,Re^b Sc^{0.33}\left(\frac{d_H}{x}\right)^d \qquad \text{eq. 6}$$

For hydrodynamically developed, diffusively developing, laminar flow, Pickett and Stanmore[1] have proposed the values for a, b and d listed in table 3, corresponding to a Lévêque-type equation derived for rectangular channels. For both hydrodynamically and diffusively developing laminar flow, Qi et al.[20] have proposed a semi-empirical correlation that considers mass transfer due to a developing hydrodynamic boundary layer. Reynolds-Sherwood graphs for both equations are depicted in supporting Information A5. It should be noted that at Re = 260 the difference between these correlations is limited.

Table 3: correlations for diffusively developing laminar flow

Reference	Condition	a	b	d
Pickett-Stanmore[1]	Developed	$0.978\left(\frac{2}{1+\gamma}\right)^{0.33}$	0.33	0.33
Qi et al.[20]	Developing	0.57	0.5	0.43
This work	Developed	3.78	0.3	0.12
This work	Developing	2.08	0.5	0.20

Overall, there is a significant difference between these equations and our experimental results. While the equations predict high initial mass transfer and a relatively rapid decline, our experimental data shows a more gradual decline. We have fitted our data to eq. 6 and the resulting values for a, b and d are listed in table 3. The result of the fitting is shown in figure A6.

In table 3 there is a notable difference in the Reynolds power (i.e.: b) between hydrodynamically developing and developed flow. For hydrodynamically developed flow, a power of around 0.33 (Pickett-Stanmore) or 0.30 (this work) is found, whereas for hydrodynamically developing flow a power of 0.5 (Qi et al. and this work) is found. Regarding the Reynolds power, our findings are in line with previous observations. However, the same is not true for the distance dependency (i.e.: d). We observe a significantly smaller distance dependency than in the works of Pickett-Stanmore and Qi. We do not have a clear explanation for this. The small irregularities due to the 3D print process and the non-uniform flow patterns observed in Figure 4 could be possible causes for the difference. It should also be noted that there is significant scatter in our experimental data (especially for the extended conic configuration). Nevertheless, we can still conclude that hydrodynamically developing flow seems to result in a stronger distance dependence, in line with the works of Qi and Pickett-Stanmore.

4.3.4. Transition or mixed flow

In Figure 4, the slope of graph increases for the divider inlet at around Re = 400. This indicates that a transition from laminar to turbulent flow is occurring. At Re > 400, mass transfer on a local scale is characterized by an initial peak followed by a gradual decline. The rate of mass transfer in the divider inlet at Re > 400 is described well by an equation of the form given in eq.6. On average, eq. 9 results in a deviation of 9% compared to the experimental data.

$$Sh = 3.24\, Re^{0.53} Sc^{0.33} \left(\frac{d_H}{x}\right)^{0.27} \qquad \text{eq. 9}$$

Interestingly, the Reynolds power is small and close to 0.50, which is similar to the developing laminar correlations given in table 3. This would imply that the flow is laminar, however, this contrasts with the space-averaged results in Figure 4 where a high slope is observed. It is therefore likely that there is an intermediate, transitionary regime.

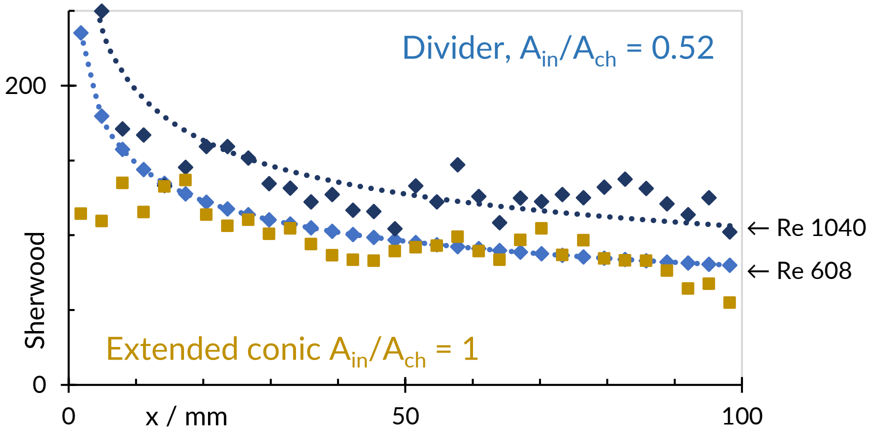

Figure 8: One-dimensional mass transfer as a result of the divider (blue diamonds) inlet in comparison to eq. 10 (blue dotted lines) and to the extended conic data (yellow squares, Re = 608). Electrolyte data is found in table 2, electrolyzer properties are listed in table 1.

The divider inlet consists of 16 square holes through which the flow enters the channel. As a result of these holes, small jets can form that are invisible to the matrix and focused pattern due to their small size. These jets induce high mass transfer as they dissipate. If a large amount of turbulence is present in the first few segments of the electrode, this could induce apparently turbulent behavior on the space-averaged scale. On the local scale, eq. 9 accounts for the initial mass transfer spike through the d_H/x term. The Reynolds power in eq. 9 is therefore less influenced by this local effect and becomes lower.

In Figure 8, the results of the extended conic configuration are shown next to those of the divider inlet. Initially, the divider inlet results in significantly higher mass transfer. However, after around 20 mm, presumably when the inlet jets have dissipated, little difference remains. This implies that the flow is laminar after a certain distance, and only appears turbulent on a space-averaged scale due to initially high mass transfer.

4.3.5. Developing and developed turbulent or turbulent-appearing flow

The conic and tube inlets show a high slope in Figure 4, which suggests that they result in turbulent flow. For turbulent flow, a local correlation for hydrodynamically developed, diffusively developing turbulent flow may be derived from eq. 2b.[3] This equation is the average of the local mass transfer function from $x = 0$ to $x = L$ and can therefore be seen as the solution of the average integral of the local mass transfer function. Inversing this operation results in eq. 10 (see supporting info). Eq. 10 is of the same form as eq. 6 and is valid for Re > 3000 and Le < 10.

$$Sh_x = 0.09375\, Re^{0.66} Sc^{0.33} \left(\frac{d_H}{x}\right)^{0.25} \qquad \text{eq. 10}$$

For hydrodynamically and diffusively developing turbulent flow, such a correlation is not available. This is in part due to the entrance effect, which complicates finding a generalized local description. For the tube inlet for instance, mass transfer as a function of x behaves chaotically.

In Figure 9, local data for the conic and tube inlet are shown next to the values predicted from eq. 3. Outside of the initial peak in mass transfer for the conic inlet, there does not seem to be a clear x-dependency of mass transfer as suggested by eq. 10. A plausible explanation is that the flow is not yet hydrodynamically developed over the entire length of the electrolyzer and as a result eq. 10 does not apply. Instead the space-averaged eq. 3 for simultaneously diffusively and hydrodynamically developing turbulent flow describes the performance reasonable well as shown in Figure 9.

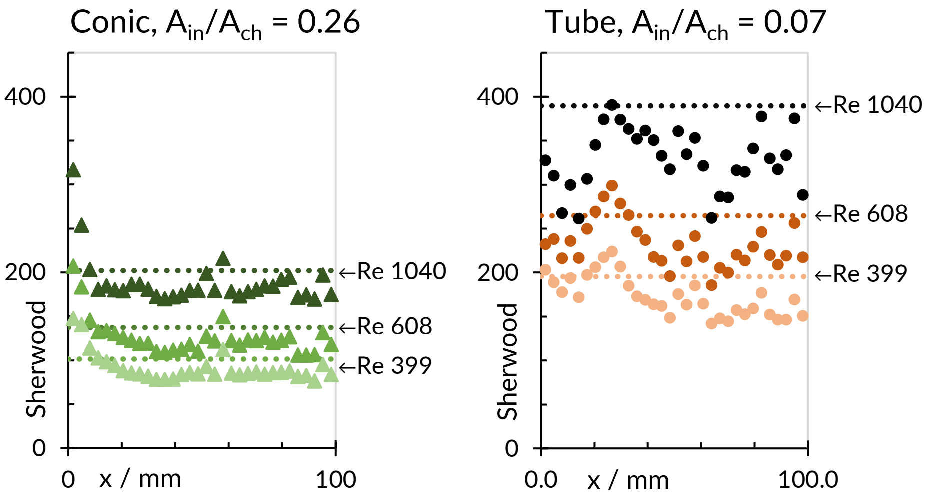

Figure 9: One-dimensional mass transfer as a result of the conic (green triangles) and tube (orange circles) inlets in comparison to eq.3 (green dotted line or orange dotted line). For both inlets, developing turbulent flow is observed. Electrolyte data is found in table 2, electrolyzer properties are listed in table 1.

4.3.6. Turbulence promotors

Turbulence promoters are often added to electrolyzers in order to enhance mass transfer.[8,10-12,31-33] This enhancement comes at a minimal cost in additional pressure drop.[8,13]

In figure 10 the effect of turbulence promoters on the local scale is shown. Overall, high mass transfer is found compared to Figure 5. Moreover, the distribution is uniform as there are no regions with exceptionally high or low mass transfer. There does not seem to be an effect of the inlet on the rate of mass transfer. Compared to the empty channel performance, an enhancement factor between 1.3 (tube) and 3.4 (extended conic) is found, depending on the inlet used in the empty channel experiments. In the work of Brown et al. a regional blocking effect is seen on segments that are covered by the promoter.[16] In our case, this does not occur because the structure of the promoter is much smaller relative to the segments. Therefore, we can conclude that turbulence promotors are an effective way to not only enhance mass transfer, but also to avoid undesired differences in local mass transfer.

Small Gyroid

Figure 10a: the small gyroid turbulence promoter pattern.

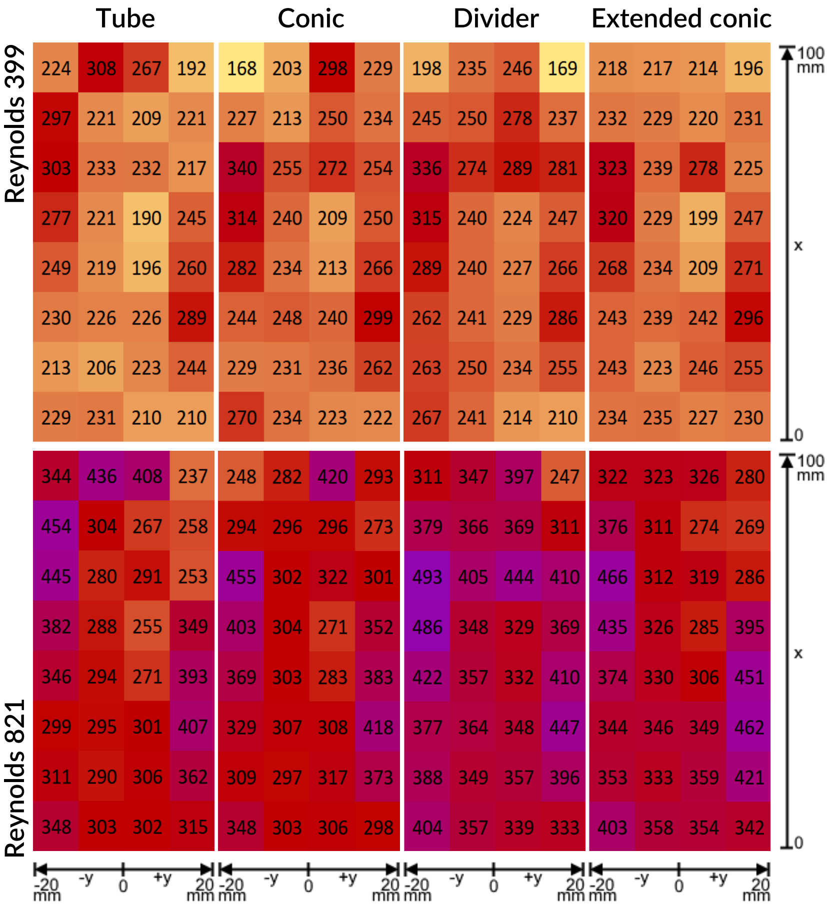

Reynolds 399	Tube				Conic				Divider				Extended conic			
	224	308	267	192	168	203	298	229	198	235	246	169	218	217	214	196
	297	221	209	221	227	213	250	234	245	250	278	237	232	229	220	231
	303	233	232	217	340	255	272	254	336	274	289	281	323	239	278	225
	277	221	190	245	314	240	209	250	315	240	224	247	320	229	199	247
	249	219	196	260	282	234	213	266	289	240	227	266	268	234	209	271
	230	226	226	289	244	248	240	299	262	241	229	286	243	239	242	296
	213	206	223	244	229	231	236	262	263	250	234	255	243	223	246	255
	229	231	210	210	270	234	223	222	267	241	214	210	234	235	227	230

Reynolds 821	Tube				Conic				Divider				Extended conic			
	344	436	408	237	248	282	420	293	311	347	397	247	322	323	326	280
	454	304	267	258	294	296	296	273	379	366	369	311	376	311	274	269
	445	280	291	253	455	302	322	301	493	405	444	410	466	312	319	286
	382	288	255	349	403	304	271	352	486	348	329	369	435	326	285	395
	346	294	271	393	369	303	283	383	422	357	332	410	374	330	306	451
	299	295	301	407	329	307	308	418	377	364	348	447	344	346	349	462
	311	290	306	362	309	297	317	373	388	349	357	396	353	333	359	421
	348	303	302	315	348	303	306	298	404	357	339	333	403	358	354	342

Figure 10b: Local mass transfer in the printed reactor with a small gyroid turbulence promoter at Re = 399. The data is colored in rectangles as a gradient from yellow to red for respectively intermediate and high Sherwood numbers. These colored rectangles represent the approximate location of the observed segment. Electrolyte properties are found in table 2, properties of the reactor are found in table 1.

4.4. Conclusion

Inlet design has a significant effect on mass transfer in electrolyzers. On the space-averaged scale, the effect of the inlet is described well using eq.3. However, there are significant effects on the local scale that space-averaged measurements do not capture. Among those are jet formation, flow channeling and recirculation streams. Consequently, regions of the electrode will experience high or low mass transfer and therefore different reaction rates.

Generally, inlet designs with the highest expansions (for instance a tube or conic inlet) result in the largest regional effects with the largest variations in both the x and y-direction. Conversely, a calmer entry (for instance with a divider inlet) results in a more uniform distribution of the rate of mass transfer. However, with a calmer flow entry, turbulence is lost and therefore the overall rate of mass transfer decreases. Therefore, a trade-off exists between high mass transfer and high uniformity. This trade-off can be avoided by using turbulence promoters. The addition of a gyroid type promoter results in both high mass transfer and high uniformity. Furthermore, the mass transfer performance became independent of the type of inlet.

One-dimensional local mass transfer can be described using equations of the form shown in eq.6. In this equation, values for the Reynolds power (i.e. b) are representative of the flow situation. For laminar flow, low values of b are found (hydrodynamically developed: b = 0.33, developing: b = 0.5), whereas for turbulent flow high values are found (hydrodynamically developed: b = 0.66, hydrodynamically developing: 0.72). The x-dependency term d_H/x describes the local variations for laminar flow well. In turbulent, hydrodynamically developing flow, the same is not true. For the conic inlet the rate of mass transfer quickly stabilizes and does not show an x-dependency. For the tube inlet, chaotic behavior is seen in both the x and y-direction.

As seen in the divider inlet, local effects can lead to a flow that appears turbulent on the space-averaged scale but behaves laminar on the local scale. In the divider inlet, this is because of significant inlet turbulence that quickly dissipates. This initially high mass transfer drives the appearance of turbulence flow on a space-averaged scale, despite laminar-like behavior in the latter half of the cell.

Acknowledgements

Funding was received for this work as part of the HIGHSINC project from Nouryon. We thank Nobian for their involvement. We enjoyed frequent discussions surrounding mass transfer with A.W. Vreman (Nobian, TU Eindhoven), who we thank for their insights.

Nomenclature

A = Electrode area, m^2

A_{ch} = Cross-sectional area of the channel, m^2

A_{in} = Cross-sectional area of the inlet, m^2

B = Electrode width (breadth), m

$C_{(III)}$ = Concentration of hexachloroiridate(III), mol/m^3

$C_{(IV)}$ = Concentration of hexachloroiridate(IV), mol/m^3

C_{bulk} = Bulk concentration of the reacting species, mol/m^3

D = Diffusion coefficient, m^2/s

d_H = Hydraulic diameter 2 BS/(B+S), dimensionless

F = Faraday's number, 76485 C/mol

$i_{A,lim}$ = Limiting current density, A/m^2

k_{LS} = Liquid-solid mass transfer coefficient, m/s

L = Electrode length, m

L_{entry} = Hydrodynamic entry length, m

n = number of electrons exchanged, dimensionless

S = Electrode spacing, m

T = Temperature, K

v_0 = Flow velocity over the electrode, m/s

Dimensionless groups

Le = Length number (= L/d_H), dimensionless

Re = Reynolds number (= $v_0 d_H/\nu$), dimensionless

Sc = Schmidth number (= ν/D), dimensionless

Sh = Sherwood number (= $k_{LS} d_H/D$), dimensionless

Greek Letters

γ = Electrode aspect ratio (=B/L), dimensionless

ν = Kinematic viscosity, m^2/s

ρ = Density of the electrolyte, kg/m^3

References

[1] Ong KL, Doctoral Thesis: The Influence of Hydrodynamic and mass-transfer entrance effects on the performance of parallel plate electrochemical flow cells, Victoria University of Manchester, 1972.

[2] Pickett DJ and Stanmore BR, Ionic mass transfer in parallel plate electrochemical cells, J. of Applied Electrochemistry 2, pp. 151-156, 1971.

[3] Pickett DJ and Ong KL, The Influence of Hydrodynamic and Mass Transfer Entrance Effects on the Operation of a Parallel Plate Electrolytic Cell, Electrochimica Acta, vol. 19, pp. 875-882, 1974.

[4] Mizushina T. The Electrochemical Method in Transport Phenomena. Adv. Heat Transf. 1971;87-161:7

[5] Velasco-Martinez G, Gutiérrez-Granados S, Alatorre-Ordaz A, Rodriguez-Torres I, Methodology for the Characterization of a parallel-plates Electrochemical Reactor, ECS Transactions, vol. 3, no. 18, pp. 1-12, 2007.

[6] Mizushina T, Ogino F, Oka Y, Fukuda H. Turbulent Heat and Mass Transfer between Wall and Fluid Streams of Large Prandtl and Schmidt Numbers. J. Heat Mass Transf. 1971;1705-1716:14.

[7] Frias-Ferrer Á, González-Garcia J, Sáez V and Expósito E, The Entrance and Exit Effects in Small Electrochemical Filter-Press Reactors Used in the Laboratory, J. Chem. Ed., vol. 82, no. 9, pp. 1395-1398, 2005.

[8] Ralph TR, Hitchman ML, Millington JP, Walsh FC. Mass transport in an Electrochemical Laboratory Filterpress Reactor and its Enhancement by Turbulence Promoters. Electrichim. Acta. 1996;41:591-603.

[9] Rivera FF, Ponce de León C, Nava JL, Walsh FC, The filter-press FM01-LC laboratory flow reactor and its applications, Electrochimica Acta, no. 163, pp. 338-354, 2015.

[10] Rivera FF, Ponce de León C, Nava JL, Walsh FC, The reaction environment in a filter-press laboratory reactor: the FM01-LC flow cell, Electrochimica Acta, no. 161, pp. 436-462, 2015.

[11] González-Garcia J, Frias A, Expósito E, Montiel V, Aldaz A. Characterization of an electrochemical pilot-plant filter-press reactor by hydrodynamic and mass transport studies. Ind. Eng. Chem., 2000;1132-1142:39.

[12] Carlsson L, Sandegren B, Simonsson D, Rihovsky M, Design and Performance of A Modular, Multi-Purpose Electrochemical Reactor, J. Electrochem. Soc., vol. 130, no. 2, pp. 342-345, 1983.

[13] Weusten SJC, Murrer LCEM, de Groot MT, van der Schaaf J, Mass transfer in 3D-printed electrolyzers: The importance of inlet effects, AIChE Journal, vol. e17263, pp. 1-12, 2021.

[14] Djati A, Brahimi M, Saidani B. Entrance effect on mass transfer in a parallel plate electrochemical reactor. J. Apl. Electrochem. 2001;833-837:31.

[15] Frías-Ferrer Á, González-García J, Sáez V, Ponce de Léon C, Walsh FC. The effects of manifold flow on mass transport in electrochemical filter-press reactors. AIChE Journal, 2008;811-823:54.

[16] Brown CJ, Pletcher D, Walsh FC, Hammond JK, Robinson D, Local mass-transport effects in the FM01 laboratory electrolyzer, Journal of Applied Electrochemistry, vol. 22, no. 7, pp. 613-619, 1992.

[17] Wragg AA, Leontaritis A. Local mass transfer and current distribution in baffled and unbaffled parallel plate electrochemical reactors. Chem. Eng. J. 1997;1-10:66T.

[18] Gerber T, Fischer P, Pinkwart K, Tübke J, Segmented Printed Circuit Board Electrode for Locally-resolved Current Density Measurements in All-Vanadium Redox Flow Batteries, Batteries, vol. 5, no. 38, pp. 1-16, 2019.

[19] Tangirala RC, Low CTJ, Ponce-de-León C, Campbell SA and Walsh FC, Copper deposition at segmented, reticulated vitreous carbon cathode in Hull cell, Transactions of the institute of metal finishing, Vols. 88-92, no. 22, pp. 84-, 2010.

[20] Qi J, Savinell R. Mass transfer in a laminar-flow parallel plate electrolytic cell with simultaneous development of velocity and concentration boundary layers. J. Appl. Electrochem., 1990;885-892:20.

[21] Santos JLC, Geraldes V, Velziarov S, Crespo J. Characterization of fluid dynamics and mass-transfer in an electrochemical oxidation cell by experimental and CFD studies. Chem. Eng. J. 2010;379-392:157

[22] Cruz-Diáz M, Rivero E, Almazán-Ruiz F, Torres-Mendoza A and González I, Design of a new FM01-LC reactor in parallel plate configuration using numerical simulation and experimental validation with residence time distribution (RTD), Chemical Engineering and Processing: Process Intensification, vol. 85, pp. 145-154, 2014.

[23] Colli AN, Bisang JM. Mass-transfer characterization in a parallel-plate electrochemical reactor with convergent flow. Electrochim. Acta, 2013;575-582:113.

[24] Rivera FF, T. Pérez T, Castañeda LF, Nava JL, Mathematical modeling and simulation of electrochemical reactors: A critical review," Chemical Engineering Science, vol. 239, p. 116622, 2021.

[25] Rivero EP, Rivera FF, Cruz-Diaz MR, Mayen E, González I. Numerical simulation of mass transport in a filter press type electrochemical FM01-LC: Comparison of predicted and experimental mass transfer coefficient. Chem. Eng. Research and Design, 2012;1969-1978:90.

[26] Weusten SJC, de Groot MT, van der Schaaf J. A comparative study of the stability of hexachloroiridate and hexacyanoferrate in electrochemical mass transfer measurements. J. Electroanal. Chem., 2020;114512:878.

[27] Weusten SJC, Murrer LCEM, de Groot MT, van der Schaaf J., Demystifying Mass Transfer in Electrolyzers through Rapid Prototyping with 3D Printed Parallel Plate Cells, in 2019 AIChE Annual Meeting, Orlando, 2019.

[28] Söhnel O, Novotny P, Densities of Aqueous Solutions of Inorganic Substances, Amsterdam: Elsevier, 1985.

[29] Wolf AV, Aqueous Solutions and Body Fluids, Hoeber, 1966

[30] Griffiths M, Ponce de Léon C, Walsh FC. Mass transport in the rectangular channel of a filter-press electrolyzer (the FM01-LC reactor). AIChE Journal. 2005;681-687:51

[31] Brown CJ, Pletcher D, Walsh FC, Hammond JK and Robinson D, Studies of space-averaged mass transport in the FM01-LC laboratory electrolyser. J. Apl. Electrochem., 1993;38-43:23.

[32] Letord-Quemere MM, Coeuret F, Legrand J. Mass transfer at the wall of a thin channel containing an expanded turbulence promoting structure. J. Electrochem. Soc. 1988;3063-3067:135.

Supporting information A

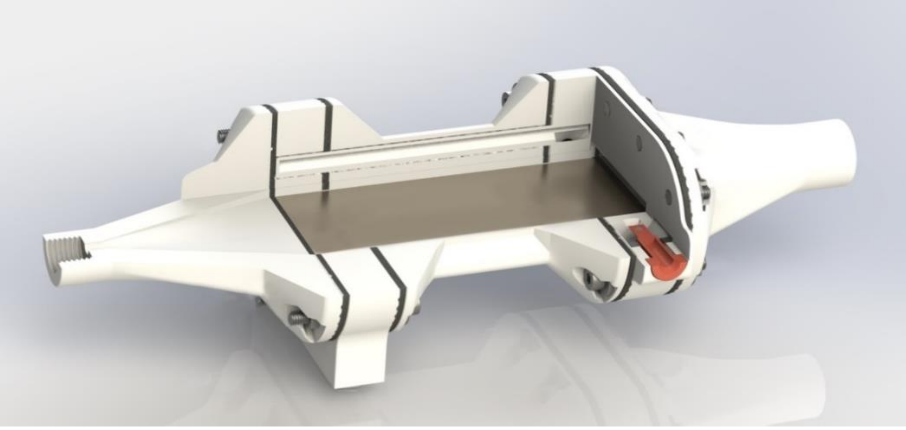

Figure A1: Rendered cutout of the printed electrolyzer in its unextended configuration, using a conic inlet and outlet. The brown nickel working electrode here is represented as a plate, though in reality this would be a segmented electrode as shown in figure 1.

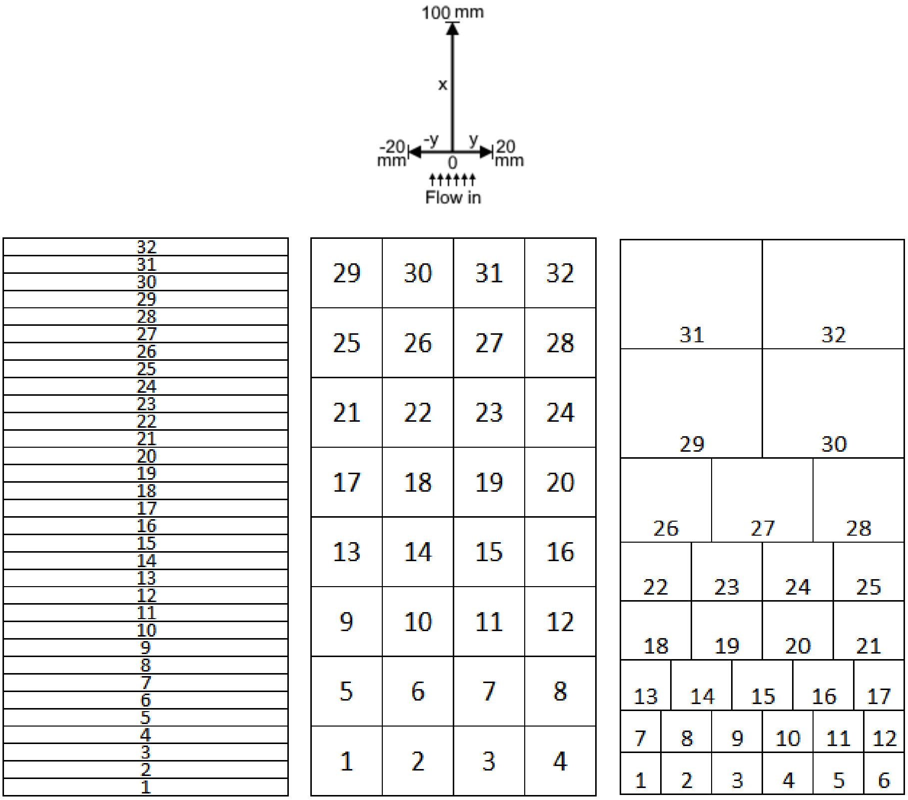

Figure A2: Segment numbering scheme. Left: series, middle left: matrix, middle right: focused, right: the axes and dimensions in mm. The bottom edge (at x = 0) is the leading edge of the electrode, i.e. the edge that is closest to the inlet.

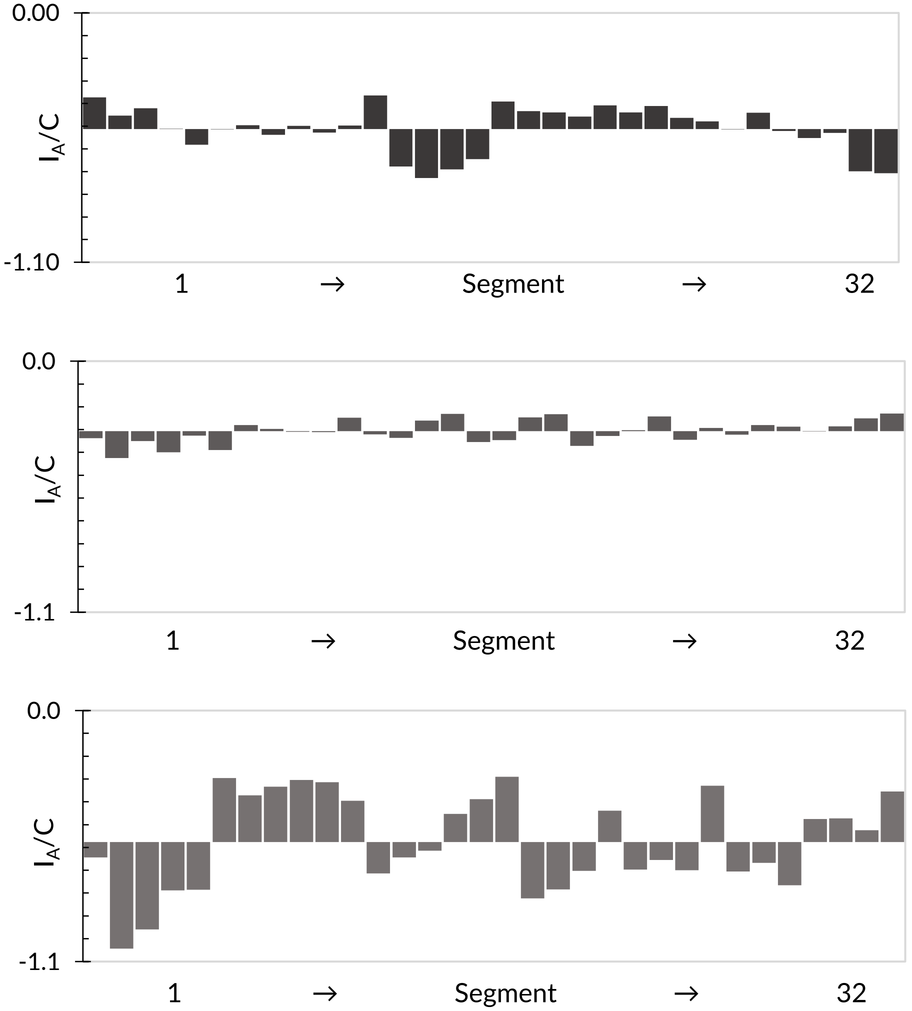

*Figure A3: averaged baseline current density measurements. These were obtained at 0 L/h, using a 50 second stabilization time, followed by a 10 second measuring period. The results are normalized by the concentration of the hexachloroiridate(IV). top: series (average -0.512 A/m^2*m^3/mol), middle: matrix (average -0.307 A/m^2*m^3/mol), bottom: focused (average -0.576 A/m^2*m^3/mol). Segment numbering is shown in figure A2*

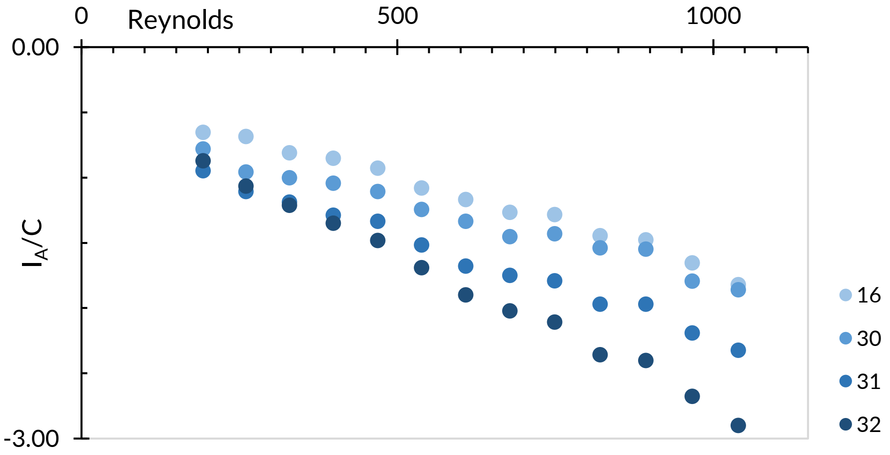

Figure A4: Current density measurement, normalized by concentration of the hexachloroiridate(IV), for the series segmentation pattern. Segment 16, 30, 31 and 32 are shown. Segments 1 through 15 and 17 through 29 perform similarly to segment 16.

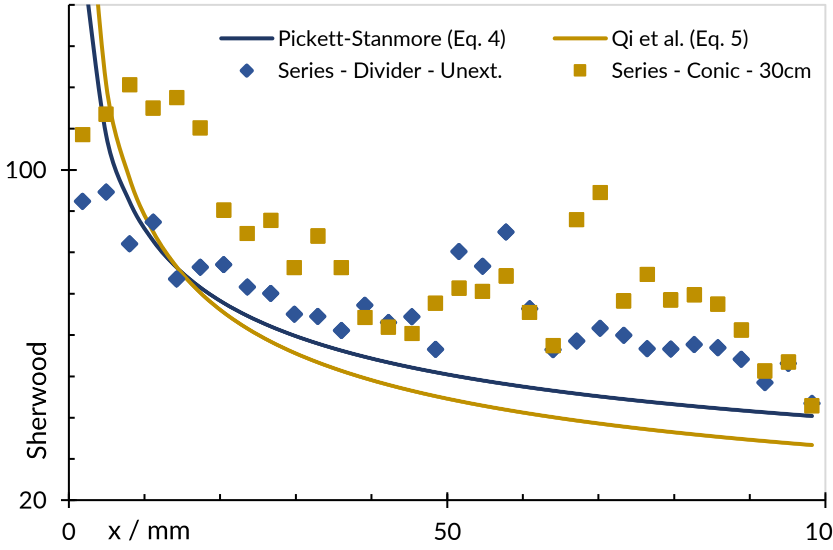

Figure A5: Laminar, one-dimensional mass transfer as a result of the extended conic (yellow squares) and divider (blue diamonds) configurations in comparison to eq. 4 (blue line) and eq. 5 (yellow line). Sherwood numbers are shown at Re = 260. Electrolyte data is found in table 2, electrolyzer properties are listed in table 1.

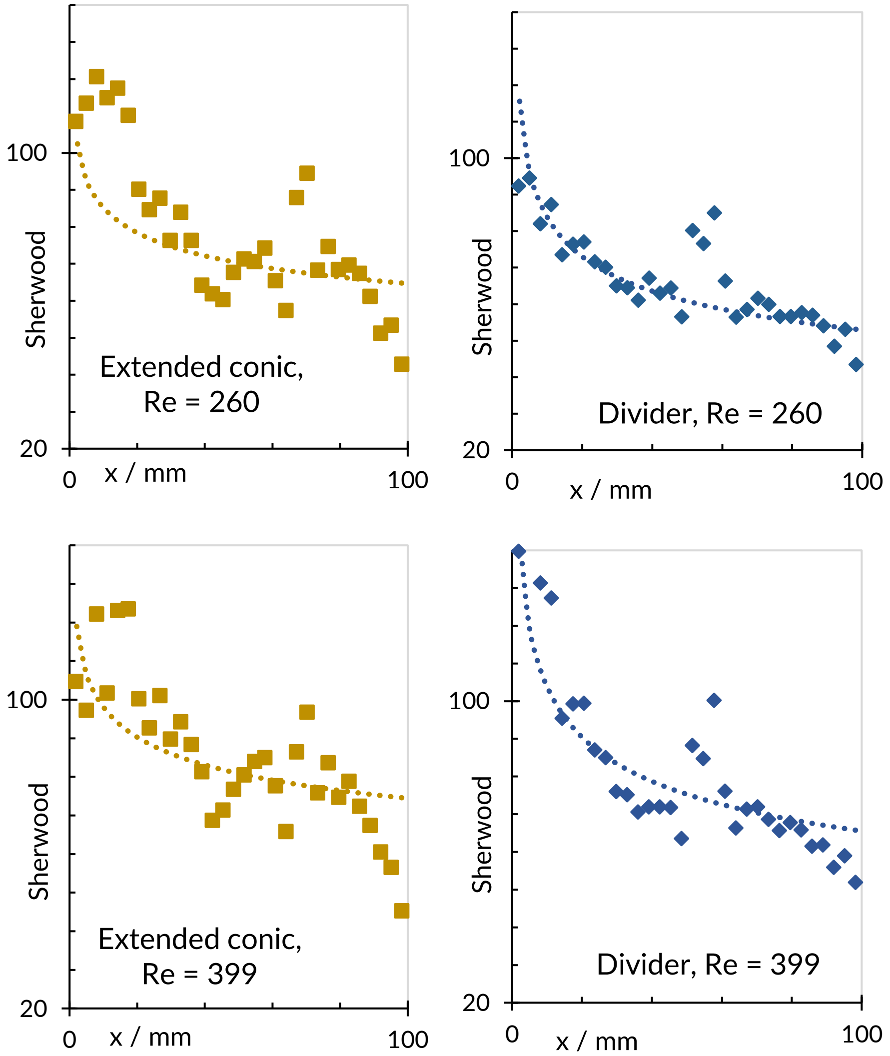

Figure A6: Local, x-direction Sherwood numbers for the extended conic (left, yellow) and divider inlet (right, blue). Dotted lines represent eq.7 (left, yellow) and eq.8 (right, blue). Experimental data is shown as either yellow squares (for the extended conic configuration on the left) or blue diamonds (for the divider inlet on the right)

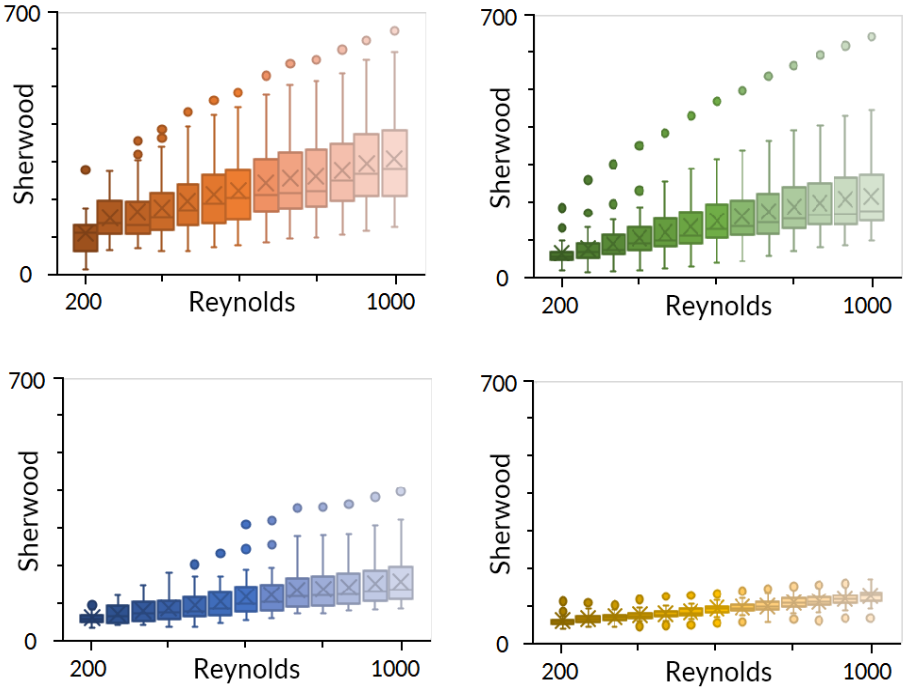

Figure A7: Boxplots of the variation in mass transfer (Sh) as observed with the matrix pattern, from Re = 192 to Re = 1040 (left to right)

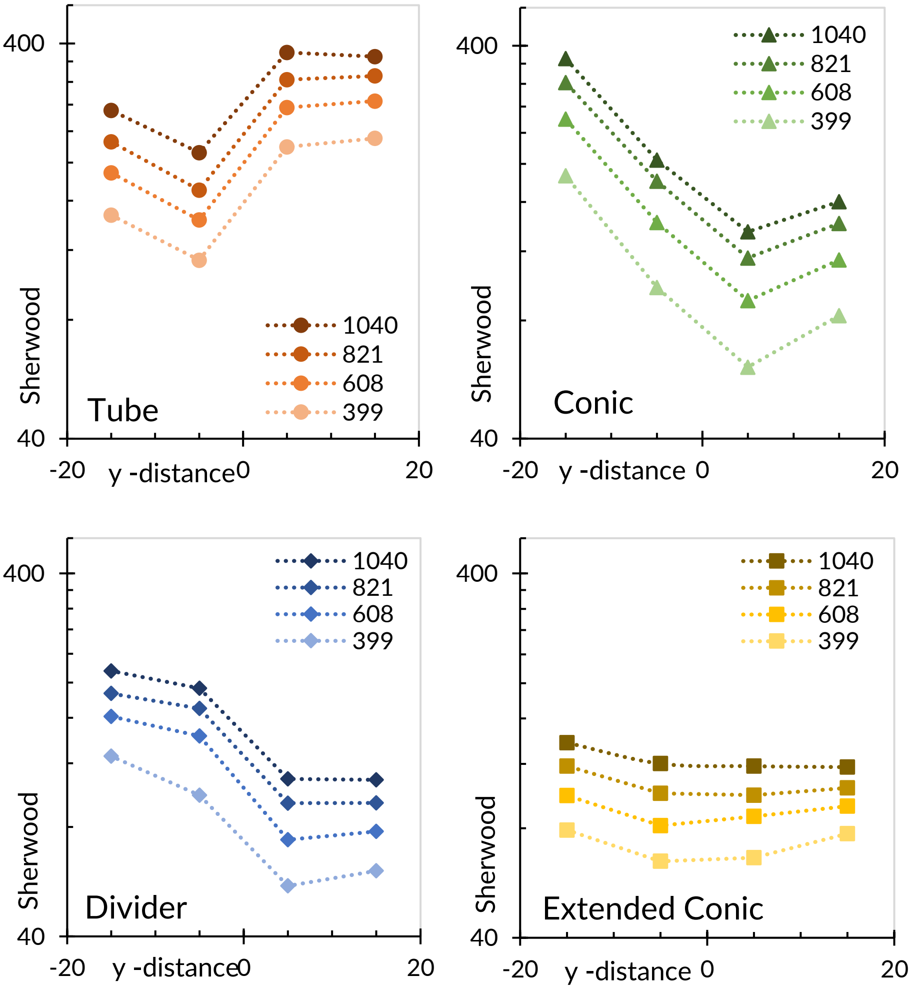

Figure A8: One-dimensional mass transfer in the y-direction as observed using the matrix segmentation pattern. Data at a given y-distance is obtained from the average of all segments sharing the same y-coordinate. The four different inlet configurations are shown: top left: tube (red circles), top right: conic (green triangles), bottom left: divider (blue diamonds), bottom right: extended conic (yellow squares).

Supporting Information B: Derivation for eq.10:

The average of a function f(x) is found using an integral:

$$f_{average} = \frac{1}{b-a}\int_{a}^{b} f(x)\,dx$$

Eq.2b is the average of an unknown local function from x=0 to x=L:

$$Sh = \frac{1}{L-0}\int_{0}^{L} Sh_x\,dx$$

Assuming only Le depends on x, rewriting Eq.2b into this format yields:

$$Sh = \frac{1}{L-0} \quad [0.125\,Re^{0.66}Sc^{0.33}d_H^{0.25}\,x^{0.75}]_0^L$$

The local function Sh_x is found by taking the derivative of the bracketed term with respect to x:

$$Sh_x = \frac{d(0.125\,Re^{0.66}Sc^{0.33}d_H^{0.25}\,x^{0.75})}{dx}$$

Rearranging the constants yields:

$$Sh_x = 0.125\,Re^{0.66}Sc^{0.33}d_H^{0.25}\frac{d(\,x^{0.75})}{dx}$$

Which after derivation and simplification results in eq.10:

$$Sh_x = 0.09375\,Re^{0.66}Sc^{0.33}\left(\frac{d_H}{x}\right)^{0.25}$$

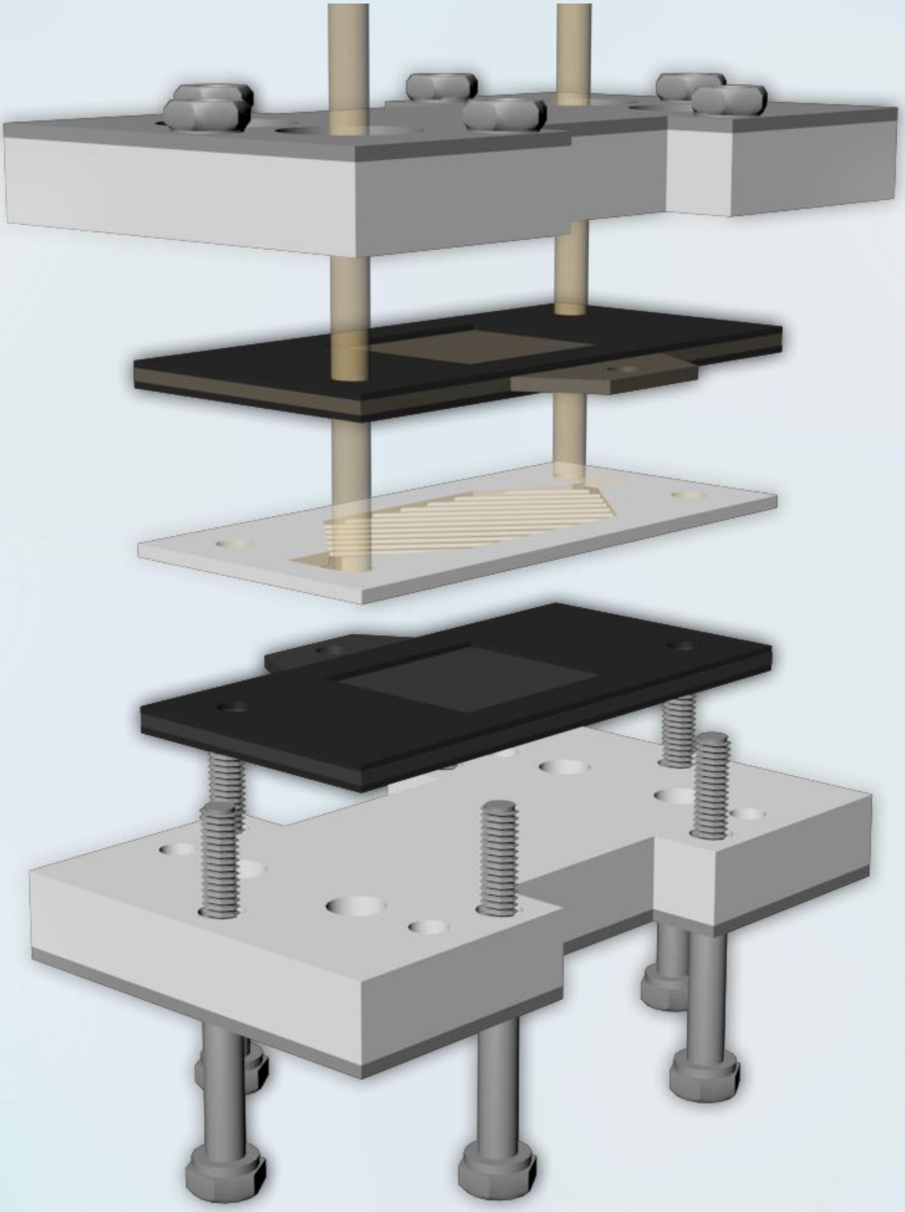

Mass transfer in the ElectroCell Microflow and MP cell and the effect of mesh electrodes

S.J.C. Weusten, J. van der Schaaf, M.T. de Groot

5 - Abstract

The Electrocell family of electrolyzers is a set of differently sized commercially available electrochemical flow reactors, suitable for scaling up new electrochemical processes. In this work mass transfer correlations are established for the smallest two flow cells namely the Microflow cell (MFC) and MP cell (MPC). The empty channel performance of the MFC and MPC is comparable to similar lab-scale reactors in literature, such as the FM01-LC and the larger Electrocell Electro Syn cell. Turbulence promoters enhance mass transfer in the MFC and MPC by only a factor 1.4 and 1.5 respectively. Also, the performance of mesh electrodes was investigated: woven and expanded mesh electrodes result in a factor 2.1 to 2.8 enhancement in mass transfer when the surface area of the mesh is considered. The overall reaction rate is enhanced by a factor 5.9 to 6.7 for woven meshes, and 1.9 to 3.0 for expanded meshes due to the higher surface area of the woven meshes. Fine woven meshes therefore seem the preferred type of electrodes for reactions limited by mass transfer.

Image: exploded view of the Electrocell MFC

5.1. Introduction

Parallel plate electrolyzers are universally used for electrochemical studies. Of these electrolyzers the filter-press arrangement is most common, due to its simple yet effective design. An example of such an electrolyzer is the FM01-LC cell, which has been extensively studied in in literature.[1-6] However, this electrolyzer is no longer commercially available, making it less accessible to present-day researchers. At the moment one of the few suppliers of commercial laboratory scale electrolyzers is ElectroCell. ElectroCell offers a family of electrolyzers with similar properties, namely the Microflow cell (MFC, electrode area: 0.001 m^2) the electro MP cell (MPC, electrode area: 0.01-0.2 m^2), the Electro Syn cell (ESC, electrode area: 0.04-1.04 m^2) and the Electro Prod cell (EPC, electrode area: 0.4-16.0 m^2). For scale-up research this family of electrolyzers is valuable since these reactors are essentially differently sized variants of a similar design.[7]

While much is known about the FM01-LC cell, only a few studies are available for the ElectroCell reactors.[8,9] In one of these studies, the mass transfer performance of the ESC is characterized by Carlsson et al.[8] However, for the MFC, MPC and EPC these characterizations are still missing. This makes it more difficult to interpret the data that are obtained using these electrolyzers.

The performance of lab-scale electrolyzers is commonly improved by using turbulence promoters.[2,5,10-13] These inert structures enhance mass transfer at a minimal cost of pressure drop.[10,14] Moreover, they help distribute flow leading to less dead volume and fewer hot spots.[1] The MFC, MPC and ESC contain a turbulence promoter by default.

Further improvements may be obtained by using 3D electrodes. These have the benefit of both inducing turbulence and increasing the available surface area. Also, these types of electrodes are commonly used in zero gap configurations, which are typically used in industrial electrochemical processes such as chlor-alkali and water electrolysis.In this work, the mass transfer performances of the MFC and MPC are investigated. The effect of the turbulence promoter is evaluated and compared to the empty channel. Finally, the mass transfer enhancement of mesh electrodes is evaluated for the MFC.

5.2. Experimental

The Electrocell MFC and MPC cells were used for this work. Their dimensions are listed in table 1. For both the mesh electrodes (shown in figure 1) and plate electrodes, the electrode spacing was 4 mm and an undivided cell was used. In the experiments with the flat plate electrodes, both the counter and working electrode were made of nickel. For the experiments using mesh electrodes, a nickel woven mesh or 316 stainless steel expanded mesh was placed on top of the plate electrode. The mesh electrode was pressed against the plate at the sides by the force of the gaskets being compressed by the screws of the microflow cell. At the sides, the nickel plate touched the mesh electrodes and served as a current collector. The middle of the nickel plate, i.e.: the part exposed to the electrolyte, was covered using electrical tape to prevent it from acting as an electrode. The nickel woven meshes were acquired from VWR chemicals, the expanded steel meshes from the Expanded Metal Company. For the expanded metal meshes the naming scheme given by the Expanded Metal Company was followed.

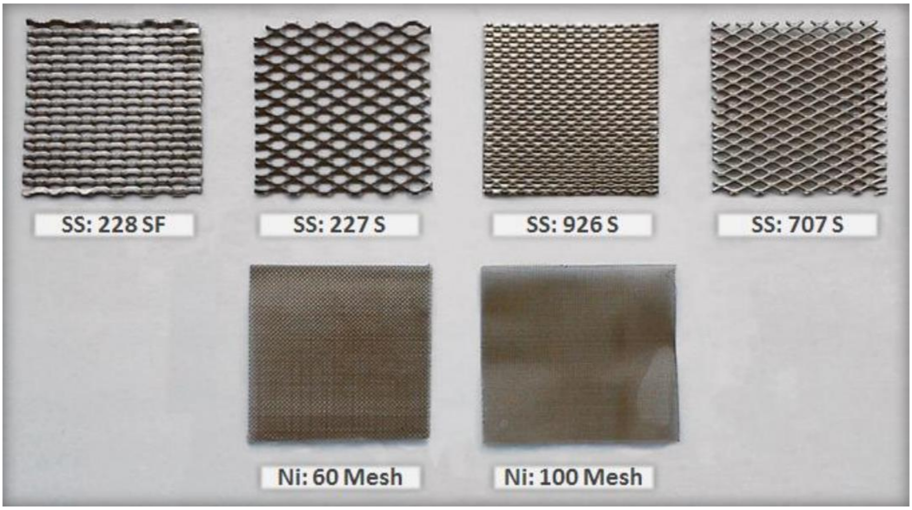

Figure 1: mesh electrodes used in this work. The top row consists of 316 stainless steel expanded meshes, the bottom row of nickel wire meshes. The ratio A_{mesh}/A_{plate}, *as well as the geometric parameters are given in table 4a and table 4b.*

By default, both the MP and MF cells contain turbulence promoters. In the case of the MF cell, this promoter could easily be omitted. For the MP cell, it was integrated with the plastic spacer and had to be cut out to obtain an empty channel configuration.

A schematic of the setups used for the experiments with the MF and MP cell is shown in figure 2, where it should be remarked that the setup for the MP cell was larger than for the MF cell. Electrolyte was stored at ambient conditions in a closed vessel. Nitrogen was bubbled through the electrolyte vessel in order to remove dissolved gases. From this vessel, electrolyte was recirculated through the electrolyzer using a pump (MF cell: Tuthill D-type gear pump, MP cell: Iwaki MD-F type centrifugal pump). The flow rate of 20-90 L/h was measured using a variable area flow meter (MF cell: Brooks-Instruments ShoRate, MP cell: Krohne). A pressure gauge was placed at the inlet of the electrolyzer to obtain an indication of the pressure drop (MF cell: analog gauge: 0.5-2.5 barg, MP cell: digital gauge 0.5-5.0 barg).

Table 1: Geometric details of the electrolyzers used in this work

Symbol	Property	MF cell	MP cell
L	Electrode length	3.4 cm	10 cm
B	Electrode width (breadth)	3.3 cm	10 cm
S	Electrode spacing	0.4 cm	0.8 cm
A	Electrode area	10.2 cm^2	100 cm^2
γ	Electrode aspect ratio B/L	0.97	1
d_H	Hydraulic diameter $2 * B * S/(B+S)$	0.71 cm	1.5 cm
Le	Length number L/d_H	4.68	6.75

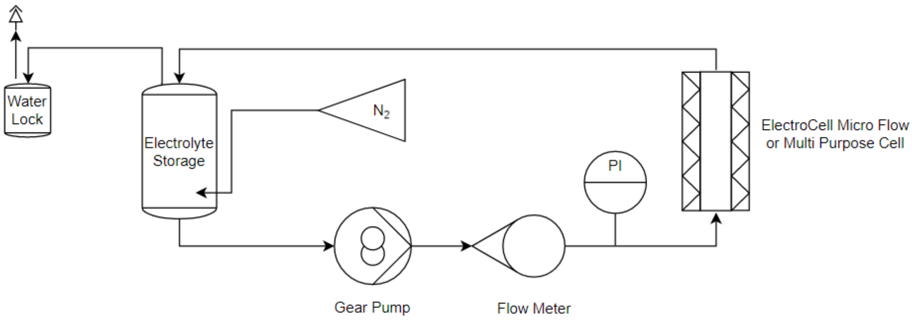

Figure 2: Schematic of the experimental setup.

The limiting current density method was used in order to measure the electrochemical rates of mass transfer.[15] The electrolyte consisted of 0.5 mM / 0.5 mM hexachloroiridate(IV)/(III) (>99.9% Sigma Aldrich) dissolved in a 0.5 M solution of potassium nitrate (>99%, VWR). The hexachloroiridate redox couple was used because it does not cause irreversible poisoning of the electrodes.[15-16] In the MF cell setup, the concentration of the hexachloroiridate(IV) was routinely measured using an offline UV-VIS spectrophotometer (Shimadzu UV2501-PC). In the MP cell setup, the electrolyte storage was sampled continuously using a Merck-Hitachi L4000A UV-VIS detector and a HPLC pump. Properties of the electrolyte are available in table 2.

Chronoamperometric experiments were performed using a potentiostat (MF cell: PGstat32 (Autolab), MP cell: Keithley 2440) at a cell potential of -0.8 V. For each measurement, the limiting current was allowed to stabilize for 20 seconds before it was registered as the average of a 10 second measurement.

The electrodes were pretreated according to the recommendations of Szanto et al.[17] The flat plate electrodes were polished using felt paper and a descending series of suspended alumina particles (i.e. 1.0 µm, 0.3 µm and 0.05 µm). Since the mesh electrodes could not be adequately polished, this step was not performed for them. In the next step, the electrodes were rinsed and sonicated twice (15 minutes at ambient conditions). Finally, the electrodes were set to evolve hydrogen for 15 minutes in a 0.5 M KOH solution (prepared from dissolving solid pellets, >99.9%, VWR). The KOH solution was then removed and the electrodes were rinsed rigorously.

Table 2: Physical properties of the electrolyte, relevant constants

Symbol	Property	Value
$\boldsymbol{\rho}$	Density of the electrolyte	1029.8 kg/m^3 [18,19]
$\boldsymbol{\nu}$	Kinematic viscosity	9.52*10^{-7} m^2/s [19]
$\boldsymbol{T}$	Temperature	298 K
$\boldsymbol{C}_{(III)}$	Concentration of hexachloroiridate(III)	1.0 mol/m^3
$\boldsymbol{C}_{(IV)}$	Concentration of hexachloroiridate(IV)	0.5 mol/m^3
$\boldsymbol{D}$	Diffusion coefficient of hexachloroiridate(IV)	8.38*10^{-10} m^2/s [20]
$\boldsymbol{Sc}$	Schmidt number of the electrolyte	1011

5.3. Results and discussion

5.3.1. Mass transfer correlations of the empty channel Electrocell Microflow cell and MP cell

Mass transfer in electrolyzers is expressed using Sherwood vs. Reynolds correlations in the form of eq. 1. [21] The Sherwood number is directly related to the limiting current density, and the Reynolds number is related to the flow rate and the hydraulic diameter d_H. In some correlations, the length number Le is used to include a dependency of mass transfer on the length of the electrode.

$$Sh = a\, Re^b Sc^c Le^d \qquad \text{eq. 1}$$

The mass transfer performance of an electrolyzer is often compared to the correlations of Pickett et al. shown in table 3. These are valid for mass transfer in hydrodynamically developed, diffusively developing flow.[21-23] Typically, much higher rates of mass transfer are found compared to these correlations, since electrolyzers usually do not contain calming sections and therefore have a hydrodynamically developing flow profile. Moreover, inlet effects canresult in enhanced mixing.[21,24]

In figure 3 the results for the empty channel electrocell MFC and MPC are shown alongside selected literature correlations (see also table 3). Significantly higher mass transfer rates are found compared to the correlations by Pickett et al., which is expected as neither the MFC nor the MPC use calming sections. Compared to the Electrocell ESC and the FM01-LC, similar performance is found for the Electrocell MPC. The Electrocell MFC on the other hand results in slightly lower mass transfer. This is likely the result of a small difference in geometry, namely a different gap distance and inlet design. The MFC has a conic inlet that is followed by a sudden expansion in gap distance of 2 mm in the inlet to 4 mm in the channel. The MPC has a flow distributor with many small channels. In the MFC it is therefore likely flow channeling is occurring, whereas in the MPC the electrode is used more evenly.[21]

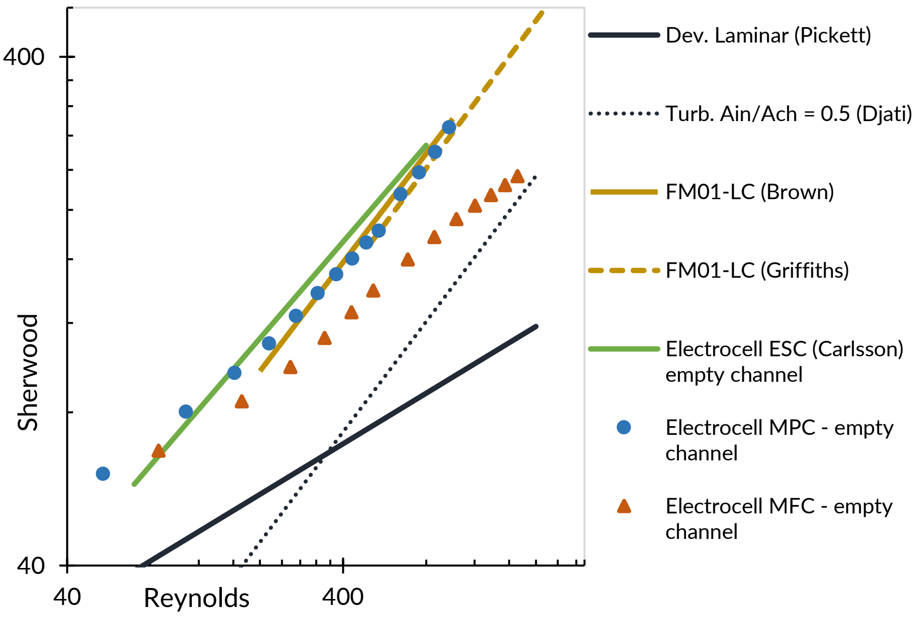

Figure 3: Mass transfer of the Electrocell MFC (orange triangles) and MPC (blue circles) alongside selected literature correlations. The correlations are given in table 3. Electrolyte data is available in table 2 and the dimensions of the MFC and MPC are available in table 1.

In table 3, mass transfer correlations are shown for the MFC and MPC alongside the literature electrolyzers. The Reynolds power (b-coefficients) of the Electrocell MFC and MPC are around 0.5. This is higher than expected for hydrodynamically developed laminar flow (b = 0.3, see eq. 2), but lower than expected for hydrodynamically developed turbulent flow (b = 0.66, eq. 4a). It is therefore likely that the flow is neither fully laminar nor turbulent, but a mixture of both regimes. This could be the case when there are small regions of turbulent flow, combined with regions of laminar flow. Such behavior was observed in previous work in experiments with segmented electrodes. (see chapter 4)

Table 3: Correlations of empty channel electrolyzers given in the form: $Sh = a\,Re^{b}Sc^{c}Le^{d}$

	Cell type	a	b	c	d	Reynolds
[22] [23]	Hydrodynamically developed, diffusively developing, laminar flow (Pickett)	$1.467\left(\frac{2}{1+\gamma}\right)^{0.33}$	0.33	0.33	-0.33	58 - 2000
[22] [23]	Hydrodynamically developed, diffusively developing, turbulent flow for Le < 10 (Pickett)	0.125	0.66	0.33	-0.25	2000 - 20000
[22] [23]	Hydrodynamically developed, diffusively developing, turbulent flow for Le > 12 (Pickett)	0.023	0.8	0.33	-	4000 - 20000
[1]	FM01-LC (Brown)	0.22	0.71	0.33	-	200 - 1000
[11]	FM01-LC (Griffiths)	0.18	0.73	0.33	-	500 - 2200
[8]	Electrocell ESC (Carlsson)	0.39	0.63	0.33	-	70 - 800
x	Electrocell MFC empty channel*	0.89	0.44	0.33	-	100 - 1700
x	Electrocell MPC empty channel*	0.60	0.54	0.33	-	50 - 1000
[8]	Electrocell ESC (Carlsson) SU grid promoter	5.57	0.40	0.33	-	70 - 800
[8]	Electrocell ESC (Carlsson) cylinders d = 7 mm promoter	0.98	0.62	0.33	-	70 - 800
[8]	Electrocell ESC (Carlsson) cylinders d = 5 mm promoter	0.38	0.71	0.33	-	70 - 800
x	Electrocell MFC with promoter	0.50	0.58	0.33	-	200 - 1700
x	Electrocell MPC with promoter	1.15	0.49	0.33	-	50 - 1000
[8]	Electrocell ESC (Carlsson) SU grid promoter	5.57	0.40	0.33	-	70 - 800

[x] *Current work.*

* *The MFC and MPC cell contain a turbulence promoter by default, these were removed to obtain the empty channel results*

5.3.2. Mass transfer enhancement by turbulence promoters

Turbulence promoters generally enhance mass transfer in electrolyzers. In figure 4, the effect is shown for the Electrocell MFC, MPC and ESC.[8] On average, there is a factor 1.5 enhancement for the MFC and a factor 1.4 enhancement for the MPC. For the ESC, the lowest enhancement of 1.5 is found for the cylindrical 5 mm (d5mm) turbulence promoter, which is of a similar structure to the tube grid promoters in the MFC and MPC. Larger enhancement factors are found by Carlsson et al. for the cylindrical 7 mm (d7mm) and the SU grid, which are 2.4 and 4.2 respectively.[8]

Correlations for the turbulence promoted Electrocell MFC, MPC and ESC are given in table 3. For all but the ESC d7mm promoter (b=0.62), the Reynolds power in these correlations differs significantly from the empty channel correlation. Important to note is that the quality of the fit for the different cells with or without promoter is affected by a slight curvature in the data. This curvature is likely representative of a flow transition or mixed regime. For the MFC promoter (b = 0.58) and the ESC with d5mm promoter (b = 0.71) a larger power is found, which indicates more turbulent flow. The opposite is true for the MPC promoter (b = 0.49) and the ESC with SU grid promoter (b = 0.40). Interestingly, a high Reynolds power does not directly imply high rates of mass transfer (see figure 4). The opposite is true for the ESC, where the smallest Reynolds power coincides with the largest average enhancement factor. Consequently, the relative difference in performance between the different ESC promoters decreases as the flow rate increases.

These results can be interpreted considering the expected flow profile. For the MFC, significant channeling is expected due to the conic inlet. With a turbulence promoter a better flow distribution is obtained. The MPC and ESC have flow distributing inlets and therefore the difference in uniformity is not as large between the empty and promoted channel.

In some cases we see lower Reynolds powers with than without turbulence promoters. This suggests that the promoters can also reduce turbulence. This loss of turbulence can be explained by friction with the inert structure, which removes energy from the flow. However, mass transfer is still high, because the flow continuously moves over and under the inert obstacles.[25]

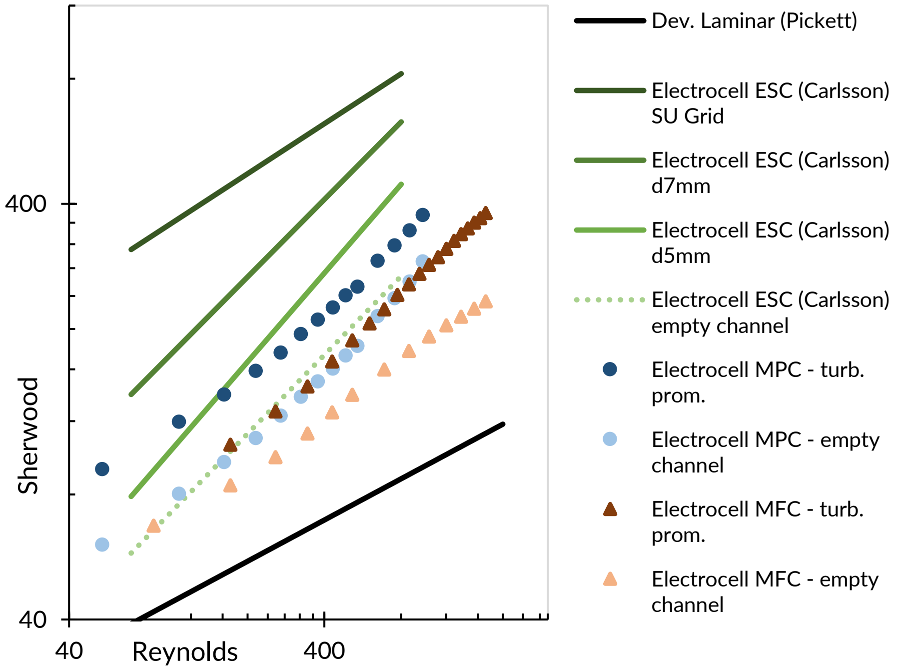

Figure 4: Mass transfer of the Electrocell ESC (Carlsson et al.[8]) (green lines), MFC (orange triangles) and MPC (blue circles) with and without turbulence promoters. The black lines represent the correlations for hydrodynamically developed flow by Pickett et al.[22-23] The correlations are given in table 4. Electrolyte data is available in table 2 and the dimensions of the MFC and MPC are available in table 1.

5.3.3. Mesh electrodes in the modified Electrocell microflow cell

The addition of mesh electrodes can result in a significant increase in mass transfer. On one hand, this is because the 3D structure increases the available surface area for reaction. On the other hand, turbulence is induced by the flow moving along the many ridges and valleys of the mesh. To separate both effects, it is useful to make a distinction between the surface area of the mesh A_{mesh} and a flat plate surface area A_{plate}. In the former, the general geometry of the mesh electrode is included, but not the surface area on a microscopic scale (< 10 µm). This is because these microscopic features likely do not contribute to macroscopic mass transfer as they are much smaller than the boundary layer (thickness between 10 – 100 µm).[26] The flat plate area A_{plate} is the width times the length of the mesh, which is the area of a flat plate with the same outer dimensions as the mesh. Due to the intricate structure of the mesh, it is more difficult to determine A_{mesh}. Though, for woven wire meshes and expanded metal meshes, the following relations can be derived (see supporting information).

Woven mesh:

$$\frac{A_{mesh}}{A_{plate}} = 0.0031\,\pi\, d_w\, n_w^2 \sqrt{(0.5\, d_w + d_o)^2 + (2\, d_w)^2} \qquad \text{eq. 2}$$

Where d_w is the wire diameter, d_o the opening size, and n_w the mesh number.

Expanded mesh:

$$\frac{A_{mesh}}{A_{plate}} = \frac{4\,d}{SWD} \sqrt{1 + \left(\frac{SWD}{LWD}\right)^2} - 4\,d\,w \left(\frac{1}{SWD^2} + \frac{1}{LWD^2}\right) + z\left(1 - p_{open}\right) \qquad \text{eq. 3}$$

Where SWD is the short width of the diamond shaped openings, LWD the long width of this diamond, d the thickness of the mesh, w the width of the expanded strands, p_{open} the percentage of open area, and z a covering factor where $z = 1$ if the back of the mesh is covered, and $z = 2$ if the mesh is exposed on all sides. In our case, $z = 1$ since the backside is covered.

For the expanded meshes a ratio of A_{mesh}/A_{plate} between 0.93 and 1.39 is found (see table 4a). The actual area of these meshes is close to that of a flat plate of the same outer dimensions. This is because of the relatively large open area of these meshes, which negates the effect of additional area from the 3D structure. More importantly, the 3D structures are relatively large and introduce little additional area. For the 227S mesh, this results in a mesh area A_{mesh} smaller than the plate area A_{plate}. The woven meshes produce much larger ratios of 2.77 (100 mesh) and 3.00 (60 mesh) due to their fine structure and low open area (see table 4b).

Table 4a: Dimensions of the expanded meshes used in this study (with z = 1)

Expanded mesh	LWD (mm)	SWD (mm)	w (mm)	d (mm)	p_{open}	$\frac{A_{mesh}}{A_{plate}}$
SS 228 SF	5.90	2.00	1.22	0.50	29 %	1.09
SS 227 S	5.84	3.39	0.81	0.46	52 %	0.93
SS 926 S	3.18	1.95	0.79	0.46	19 %	1.39
SS 707 S	4.75	2.38	0.56	0.46	53 %	1.11

Table 4b: Dimensions of the woven wire meshes used in this study

Woven mesh	n_w	d_w (mm)	d_0 (mm)	p_{open}	$\frac{A_{mesh}}{A_{plate}}$
Ni 60 Mesh	60	0.18	0.22	30 %	3.00
Ni 100 Mesh	100	0.1	0.15	36 %	2.77

In figure 5 the electrode area adjusted mass transfer performance of the mesh electrodes is shown. Compared to the flat plate electrode, an average enhancement factor between 2.1 and 2.7 is found. This enhancement is solely due to induced turbulence, since the Sherwood number is calculated based on the actual area of the mesh A_{mesh}. The 228SF, 707S and 100 meshes result in the highest average enhancement, and the SS 227 S in the lowest. Between the 926 S and the 227 S, a notable difference in slope is seen in the mass transfer performance. At low flow rates (Re < 600), the 227 S results in higher mass transfer, whereas at high flow rates (Re > 600) the 926 S offers better performance. The 228SF, 707S and 100 mesh perform almost identically, despite having significantly different geometry and therefore there does not seem to be a correlation between any individual geometrical parameter and the mass transfer performance.

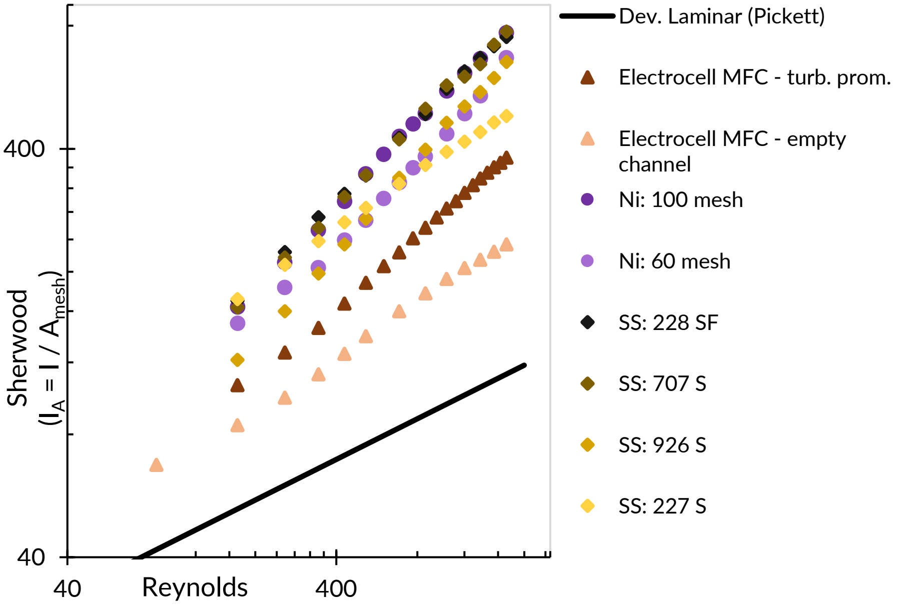

Figure 5: Mass transfer performance of mesh electrodes, excluding the effect of surface area. The Sherwood number is calculated from the limiting current density, in which the area is defined as the area of the mesh A_{mesh}. The geometric parameters of the meshes are given in table 4a and table 4b. Electrolyte data is available in table 2 and the dimensions of the MFC are available in table 1. See also supporting info figure A1.

Compared to the turbulence promoter, higher rates of mass transfer are found for the mesh electrodes. This may be because the mesh electrodes induce turbulence right at the surface of the electrode, and therefore are more effective at thinning the boundary layer. This is difficult to confirm, because the standard MFC turbulence promoter has a relatively small enhancement factor compared to literature promoters.[2,5,8,11-13] It is possible that with more effective promoters, rates of mass transfer can be achieved that are higher than those of the mesh electrodes used here.

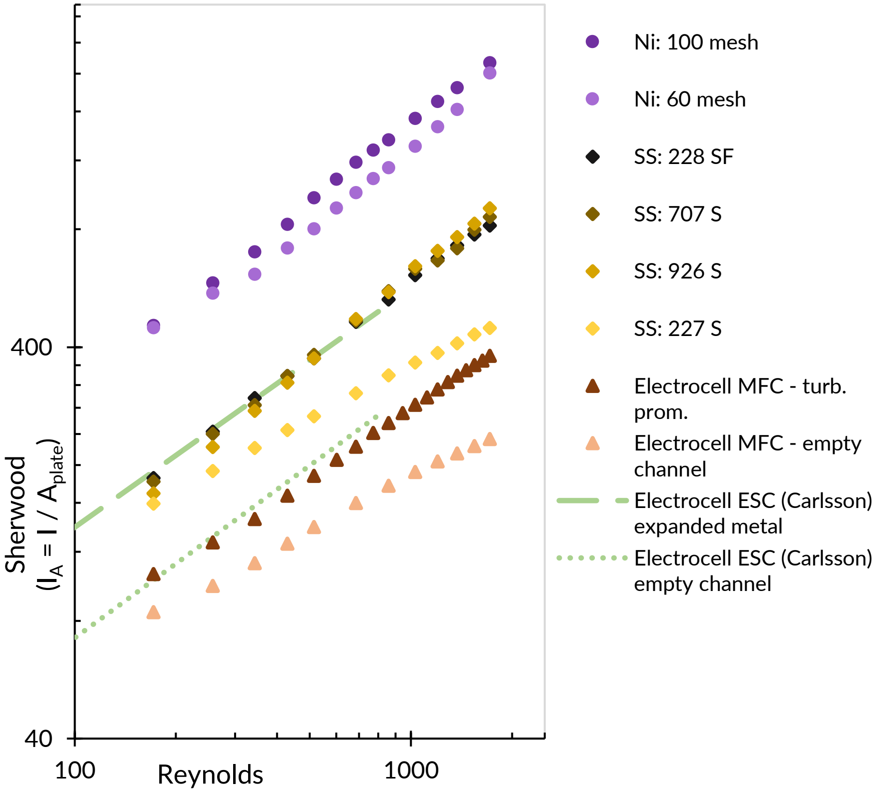

Figure 6: Mass transfer performance of mesh electrodes, including the effect of surface area. The Sherwood number is calculated from the limiting current density, in which the area is the area of the mesh A_{mesh}. The geometric parameters of the meshes are given in table 4a and table 4b. Electrolyte data is available in table 2 and the dimensions of the MFC are available in table 1. The literature correlation by Carlsson et al. is assumed to give the Sherwood number in terms of A_{plate}, which is equal to the Sherwood number multiplied by the area ratio A_{mesh}/A_{plate} reported here.[8]

In table 5, correlations are given for the MFC with mesh electrodes. For all the meshes except the 227 S, a high Reynolds power is found. This indicates that turbulent flow is occurring. Furthermore, the power in these correlations (b=0.65 to b=0.74) is higher than that of the empty channel (b = 0.44), further indicating that the mesh electrodes are effective at inducing turbulence. The exception is the 227 S (b = 0.45), which does not seem to result in more turbulent flow, despite increasing mass transfer by roughly a factor two. It is not clear why this particular mesh deviates from the others.

Though the expanded and woven mesh electrodes perform similarly in figure 5, the overall mass transfer rates vary significantly due to the difference in surface area. In figure 6, the effect of the surface area is included by basing the Sherwood number on the plate area. In a mass transfer limited reaction, the woven mesh electrodes result in vastly increased rates of reaction, owing to both a high surface area and high rate of mass transfer. Compared to the flat plate, a factor 6.7 and 5.9 difference is found for the woven 100 mesh and 60 mesh. The 228 SF, 707 S and 926 S expanded meshes only have slightly increased surface area compared to the flat plate and therefore show comparable enhancement as in Figure 5 (roughly a factor 3.0). Furthermore, these three expanded meshes appear to perform almost identically. The 227 S is the only expanded mesh that has a smaller area relative to the plate, and as a result the performance is low compared to the other meshes. The 227 S performs on average a factor 1.9 higher than the flat plate. For the ESC, the difference in performance between an expanded mesh electrode and a flat plate is around a factor 2.[8]

Table 5: Correlations of electrolyzers with mesh electrodes, excluding the effect of surface area, in the form: $Sh = a\,Re^{b}Sc^{c}Le^{d}$

Configuration	a	b	c	d	Reynolds
MF cell Ni 100 mesh	0.49	0.68	0.33	-	200 – 1700
MF cell Ni 60 mesh	0.43	0.67	0.33	-	200 – 1700
MF cell SS 228 SF	0.61	0.65	0.33	-	200 – 1700
MF cell SS 707 S	0.52	0.67	0.33	-	200 – 1700
MF cell SS 926 S	0.28	0.74	0.33	-	200 – 1700
MF cell SS 227 S	1.75	0.45	0.33	-	200 – 1700

5.4. Conclusion

Our results have shown that the empty channel mass transfer performance of the MFC and MPC are similar to that of the ESC and FM01-LC reported in literature.[1,8,11] The turbulence promoters in the MFC and MPC result in a mass transfer enhancement factor of 1.5 and 1.4 compared to the empty channel. This is low compared to other turbulence promoters seen in literature. In the ESC for instance, the SU grid promoter results in an enhancement factor of 4.2.

Mesh electrodes both increase mass transfer and surface area. To separate both effects, equations can be derived for the actual surface area of the mesh.[26] For expanded mesh electrodes, the resultant area is close to that of an equivalently sized flat plate electrode. Woven meshes on the other hand, result in roughly three times more surface area. This is because woven meshes have a fine internal structure and a small amount of open area. Between different mesh types, there is a limited variation in mass transfer performance (factor 2.1 to 2.8 enhancement) based on the actual surface area. However, because of the large area, the rate of reaction of mesh electrodes in mass transfer limited reactions will be significantly higher. Compared to a flat plate electrode, a woven mesh results in reaction rates that are 5.7 to 6.7 times faster. For the expanded mesh electrodes, there is a factor 1.9 to 3.0 difference. When deciding on the optimal electrode design for mass transfer limited reactions, the surface area seems more important that the mesh structure.

Acknowledgements

This work was funded as part of the HIGHSINC project from AkzoNobel (now Nobian). Part of this work was carried out at AkzoNobel RD&I (now Nobian) in Deventer. We thank them for their involvement. Though we did not include CFD studies in this work, we thank A.W. Vreman for his insights based on preliminary calculations in the subject area.

Nomenclature

A = Electrode area, m^2

A_{mesh} = Actual electrode area, m^2

A_{plate} = Flat plate electrode area, m^2

B = Electrode width (breadth), m

$C_{(III)}$ = Concentration of hexachloroiridate(III), mol/m^3

$C_{(IV)}$ = Concentration of hexachloroiridate(IV), mol/m^3

D = Diffusion coefficient, m^2/s

d = Thickness of the expanded mesh, mm

d_H = Hydraulic diameter 2 BS/(B+S), dimensionless

d_o = Diameter of the opening of a woven mesh, mm

d_w = Diameter of the wire of a woven mesh, mm

F = Faraday's number, 76485 C/mol

I = Current, A

I_A = Current density, A/m^2

L = Electrode length, m

LWD = Long width of the diamond, mm

n_w = Mesh number, mesh units per square inch

p_{open} = Open area, dimensionless

SWD = Short width of the diamond, mm

S = Electrode spacing, m

T = Temperature, K

w = Width of the expanded mesh, mm

Dimensionless groups

Le = Length number (= L/d_H), dimensionless

Re = Reynolds number (= $v_0 d_H/\nu$), dimensionless

Sc = Schmidth number (= ν/D), dimensionless

Sh = Sherwood number (= $k_{LS} d_H/D$), dimensionless

Greek Letters

γ = Electrode aspect ratio (=B/L), dimensionless

ν = Kinematic viscosity, m^2/s

ρ = Density of the electrolyte, kg/m^3

References

[1] Brown CJ, Pletcher D, Walsh FC, Hammond JK, Robinson D, Local mass-transport effects in the FM01 laboratory electrolyzer, Journal of Applied Electrochemistry, vol. 22, no. 7, pp. 613-619, 1992.

[2] Brown CJ, Pletcher D, Walsh FC, Hammond JK and Robinson D, Studies of space-averaged mass transport in the FM01-LC laboratory electrolyser. J. Apl. Electrochem., 1993;38-43:23.

[3] Hammond J, Robinson D, Mass transport studies in filterpress monopolar (FM-Type) Electrolysers, Dechema-Monographs, vol. 123, pp. 279-295, 1991.

[4] Rivera FF, Ponce de León C, Nava JL, Walsh FC, The filter-press FM01-LC laboratory flow reactor and its applications, Electrochimica Acta, no. 163, pp. 338-354, 2015.

[5] Rivera FF, Ponce de León C, Nava JL, Walsh FC, The reaction environment in a filter-press laboratory reactor: the FM01-LC flow cell, Electrochimica Acta, no. 161, pp. 436-462, 2015.

[6] Rivero EP, Rivera FF, Cruz-Diaz MR, Mayen E, González I. Numerical simulation of mass transport in a filter press type electrochemical FM01-LC: Comparison of predicted and experimental mass transfer coefficient. Chem. Eng. Research and Design, 2012;1969-1978:90.

[7] Arenas LF, Ponce de León C, Walsh FC, Critical Review - The Versatile Plane Parallel Electrode Geometry: An Illustrated Review, J. Electrochem. Soc., vol. 167, 2020.

[8] Carlsson L, Sandegren B, Simonsson D, Rihovsky M, Design and Performance of A Modular, Multi-Purpose Electrochemical Reactor, J. Electrochem. Soc., vol. 130, no. 2, pp. 342-345, 1983.

[9] Carlsson L, Holmberg H, Johansson B, Nilsson A, Technique of Electroorganic Synthesis part III, New York: J. Wiley & Sons, 1982.

[10] Ralph TR, Hitchman ML, Millington JP, Walsh FC. Mass transport in an Electrochemical Laboratory Filterpress Reactor and its Enhancement by Turbulence Promoters. Electrichim. Acta. 1996;41:591-603.

[11] Griffiths M, Ponce de Léon C, Walsh FC. Mass transport in the rectangular channel of a filter-press electrolyzer (the FM01-LC reactor). AIChE Journal. 2005;681-687:51

[12] González-Garcia J, Frias A, Expósito E, Montiel V, Aldaz A. Characterization of an electrochemical pilot-plant filter-press reactor by hydrodynamic and mass transport studies. Ind. Eng. Chem., 2000;1132-1142:39.

[13] Letord-Quemere MM, Coeuret F, Legrand J. Mass transfer at the wall of a thin channel containing an expanded turbulence promoting structure. J. Electrochem. Soc. 1988;3063-3067:135.

[14] Weusten SJC, Murrer LCEM, de Groot MT, van der Schaaf J, Mass transfer in 3D-printed electrolyzers: The importance of inlet effects, AIChE Journal, vol. e17263, pp. 1-12, 2021.

[15] Mizushina T. The Electrochemical Method in Transport Phenomena. Adv. Heat Transf. 1971;87-161:7

[16] Petrovic S, Cyclic Voltammetry of Hexachloroiridate(IV): An Alternative to the Electrochemical Study of the Ferricyanide Ion, Chem. Educator, 5 (2000) 231.

[17] Szánto DA, Cleghorn S, Ponce-de-Léon C and Walsh FC, The Limiting Current for Reduction of the Ferricyanide Ion at Nickel, AIChE, 54 (2008) 802.

[18] Söhnel O, Novotny P, Densities of Aqueous Solutions of Inorganic Substances, Amsterdam: Elsevier, 1985.

[19] Wolf AV, Aqueous Solutions and Body Fluids, Hoeber, 1966

[20] Weusten SJC, de Groot MT, van der Schaaf J. A comparative study of the stability of hexachloroiridate and hexacyanoferrate in electrochemical mass transfer measurements. J. Electroanal. Chem., 2020;114512:878.

[21] Weusten SJC, Murrer LCEM, de Groot MT, van der Schaaf J., Demystifying Mass Transfer in Electrolyzers through Rapid Prototyping with 3D Printed Parallel Plate Cells, in 2019 AIChE Annual Meeting, Orlando, 2019.

[22] Pickett DJ and Ong KL, The Influence of Hydrodynamic and Mass Transfer Entrance Effects on the Operation of a Parallel Plate Electrolytic Cell, Electrochimica Acta, vol. 19, pp. 875-882, 1974.

[23] Ong KL, Doctoral Thesis: The Influence of Hydrodynamic and mass-transfer entrance effects on the performance of parallel plate electrochemical flow cells, Victoria University of Manchester, 1972.

[24] Djati A, Brahimi M, Saidani B. Entrance effect on mass transfer in a parallel plate electrochemical reactor. J. Apl. Electrochem. 2001;833-837:31.

[25] Frias-Ferrer Á, González-Garcia J, Sáez V and Expósito E, The Entrance and Exit Effects in Small Electrochemical Filter-Press Reactors Used in the Laboratory, J. Chem. Ed., vol. 82, no. 9, pp. 1395-1398, 2005.

[26] Granados-Mendoza P, Weusten SJC, M. Groot, Keurentjes J, Schouten J and van der Schaaf J, Liquid-solid mass transfer to a rotating mesh electrode in a rotor-stator spinning disc configuration, Int. J. Heat Mass Transf., 104 (2017) 650.

Supporting information A

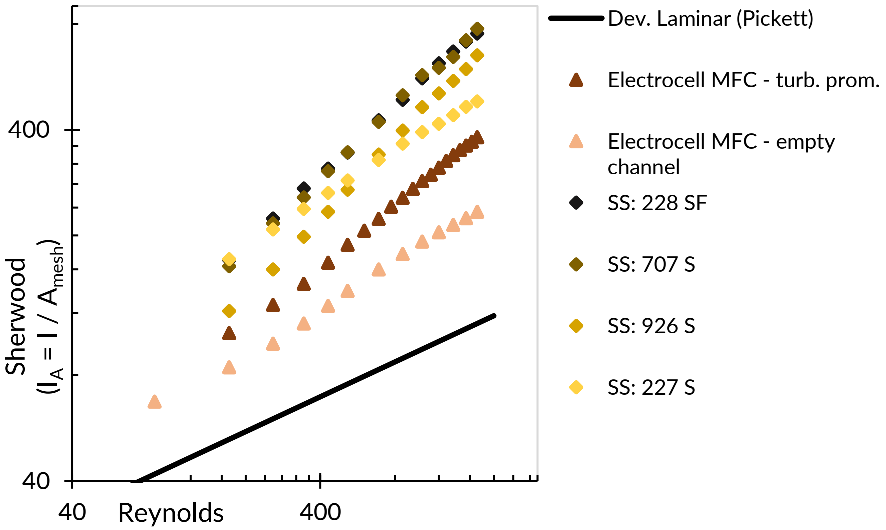

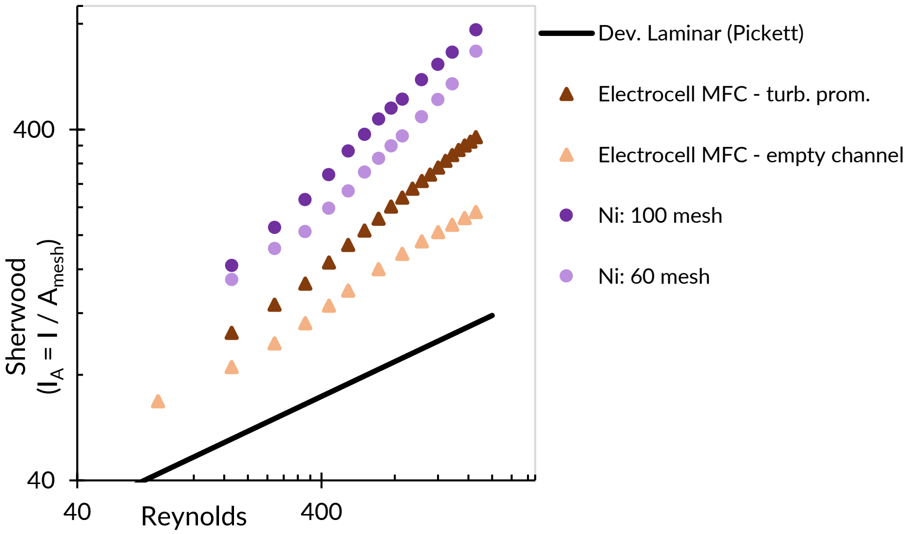

Figure A1: Mass transfer performance of mesh electrodes, excluding the effect of surface area. Top: expanded meshes, bottom: woven meshes. The Sherwood number is calculated from the limiting current density, in which the area is defined as the area of the mesh A_{mesh}. *The geometric parameters of the meshes are given in table 4a and table 4b. Electrolyte data is available in table 2 and the dimensions of the MFC are available in table 1. A selection of this data is shown in figure 6.*

Supporting information B

A formula is derived here for the actual surface area of expanded mesh electrodes. The expanded mesh is divided into rhombus shaped units with an area: $\mathrm{A_{plate}} = 0.5\ \mathrm{SWD} * \mathrm{LWD}$. The exposed surface area of the mesh within one rhombus unit is given as:

$$\mathrm{A_{mesh}} = \mathrm{z\,A_{front}} + 4\,\mathrm{A_{side}}$$

Here $\mathrm{z} = 1$ if the back of the expanded mesh is covered and $\mathrm{z} = 2$ if the mesh is exposed on all sides. The area of the front and back face can be calculated using the fraction of open area:

$$\mathrm{n\,A_{front}} = \mathrm{z\,A_{plate}}\left(1 - \mathrm{p_{open}}\right)$$

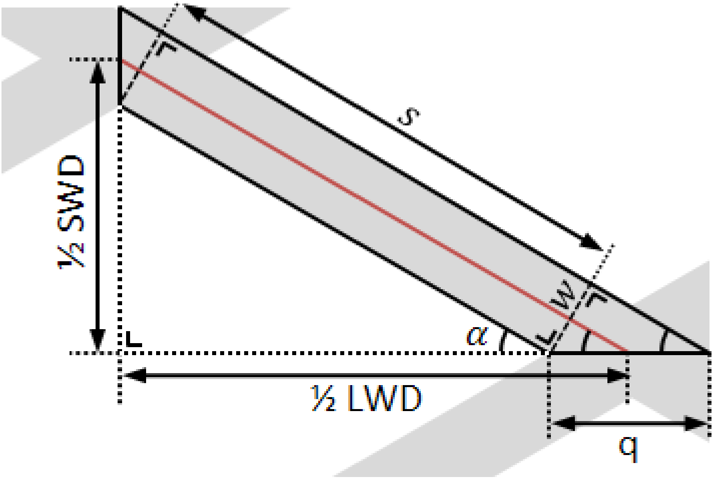

Figure B1: Trigonometric relations of an expanded mesh.

To calculate A_{side}, length s must be known, which can be calculated using trigonometric relations (see figure B1):

$$A_{\mathrm{side}} = \mathrm{d} * \mathrm{s} = \mathrm{d} * \left(\frac{\mathrm{LWD}}{2} - \frac{\mathrm{q}}{2}\right) \cos(\alpha)^{-1},$$

$$\text{with } \mathrm{q} = \mathrm{w}\sin(\alpha)^{-1}, \qquad \alpha = \mathrm{atan}\left(\frac{\mathrm{SWD}}{\mathrm{LWD}}\right)$$

The expression can be simplified and rewritten by recognizing that:

$$\sin(\mathrm{atan}(x))^{-1} = x^{-1}\sqrt{1 + x^2}$$

$$\cos(\mathrm{atan}(x))^{-1} = \sqrt{1 + x^2}.$$

The expression for A_{side} then becomes:

$$A_{\mathrm{side}} = \frac{\mathrm{d}}{2}\left[\mathrm{LWD}\sqrt{1 + \left(\frac{\mathrm{SWD}}{\mathrm{LWD}}\right)^2} - \mathrm{w}\left(\frac{\mathrm{LWD}}{\mathrm{SWD}} + \frac{\mathrm{SWD}}{\mathrm{LWD}}\right)\right]$$

The ratio of exposed surface area of the mesh to the actual area of the rhombus unit is then found to be:

$$\frac{A_{\mathrm{mesh}}}{A_{\mathrm{plate}}} = \frac{4\,\mathrm{d}}{\mathrm{SWD}}\sqrt{1 + \left(\frac{\mathrm{SWD}}{\mathrm{LWD}}\right)^2} - 4\,\mathrm{d}\,\mathrm{w}\left(\frac{1}{\mathrm{SWD}^2} + \frac{1}{\mathrm{LWD}^2}\right) + \mathrm{z}\left(1 - \mathrm{p}_{\mathrm{open}}\right)$$

Conclusions and outlook

In this work the mass transfer performance of parallel plate electrolyzers was investigated. The research can be divided into three subtopics: 1) improving electrochemical mass transfer measurements by finding a redox couple that does not poison the electrodes, 2) characterizing mass transfer in parallel plate cells, specifically in relation to entrance effects, 3) intensifying mass transfer with 3D electrodes. Here we discuss the outcomes and implications of our investigations.

Image: 3D printed zero gap water electrolyzer

6.1. Electrochemical mass transfer measurements

Electrochemical mass transfer measurements are typically performed using the hexacyanoferrate redox couple. However, during such measurements, hexacyanoferrate can undergo a side reaction that results in the deposition of an inhibiting layer on the electrode. This electrode poisoning can affect the accuracy of the measurement and therefore additional steps must be included in the experimental procedure to limit its effects. For instance, the electrode should be polished routinely to remove the passivating layer.

In **chapter 2**, hexachloroiridate is investigated as an alternative to hexacyanoferrate. It is shown that hexachloroiridate does not poison the electrodes. As a result, accurate measurements can be obtained without frequent polishing. For 3D electrodes this is particularly useful, as it is not practical to polish them. However, the bulk concentration of hexachloroiridate(IV) degrades comparatively fast due to spontaneous reduction and/or attack by hydroxide groups. This can be troublesome, as this redox couple is relatively expensive. The degradation is strongly dependent on the pH of the solution. In weakly acidic to strongly acidic solutions (pH 2-5), the iridate complex is most stable. In alkaline solutions, the complex is quickly attacked by hydroxide groups. This severely limits the pH-range of the solution used for mass transfer measurements with hexachloroiridate. A secondary consequence is that hexachloroiridate cannot be used to measure electrodes with limited stability in acidic media.

Nevertheless, much remains to be discovered about the hexachloroiridate redox couple. For instance, there may be different types of supporting electrolyte that can be used to slow the rate of degradation. Furthermore, deeper investigations into the experimental conditions can lead to better understanding in how to preserve the stability of the redox couple. Alternatively, there are possibly other redox couples which avoid electrode poisoning. Further investigations into such alternatives could lead to finding a more ideal redox couple.

6.2. Mass transfer in parallel plate cells

In **chapter 3** and **chapter 4** it is shown that the mass transfer performance of parallel plate cells is greatly dependent on the design of the inlet. Up to a factor 2.2 difference in Sherwood numbers is seen depending on the type of inlet that is used. Furthermore an earlier than expected transition to turbulent flow is seen. Both effects are explained by the sudden expansion of the flow from the inlet to the channel. The ratio of the crossectional area of the inlet to the channel explains the difference in performance well. The inlet effect can be reduced by using either calming sections or turbulence promoters. In the former case, this coincides with a reduction is mass transfer performance, since the flow becomes calmer before it enters the space between the electrodes. In the latter case, high mass transfer is observed (up to a factor 4 larger).

On a local scale, the type of inlet also affects the uniformity of the mass transfer profile. With the tube inlet, very large regional effects are seen due to the formation of a jet and a recirculating stream. Such effects are not observed when turbulence promoters are used. With the gyroid promoter, uniform high rates of mass transfer are found.

Since many electrochemical processes are mass transfer limited, it stands to reason that the type of inlet will greatly affect the productivity of these processes. A point of attention herein is the transition from lab-scale research to larger-scale production. In large electrolyzers, the inlet area is relatively small compared to the size of the electrode. This means that the inlet effect is therefore localized to a smaller area in the electrolyzer. In lab-scale electrolyzers, the inlet effect is much stronger due to the difference in scale. As a result, if the mass transfer enhancement by the inlet is not properly accounted for, significantly different performance may be observed between the lab-scale and the production-scale. In the worst case, this could result in processes that are unexpectedly unproductive after scaling up from the lab-scale.

A limited selection of 3D printed geometries has been tested in this thesis. Though this selection gives adequate insight into the mass transfer behavior of parallel plate cells, there are further opportunities to deepen our understanding. For instance, the geometries (conic, tube, divider) used for the inlets are fairly simple and represent geometries typically seen in traditionally manufactured electrolyzers. However, the design freedom in additive manufacturing is much greater than traditional machining. This means that far more complex designs could be built and investigated. For instance, turbulence promoting structures could be integrated into the inlet or channel. Moreover, one could design an electrolyzer that takes advantage of the inlet effect. Perhaps this could be achieved by using an inlet manifold that splits the flow into many smaller nozzles distributed over the length of the electrolyzer. Using 3D printing, such complex geometries would not be out of the realm of possibilites.

6.3. 3D electrodes

In **chapter 5**, the ElectroCell MicroFlow and MP cell were characterized and Sherwood-Reynolds correlations describing their performance were established. Similar performance is found compared to electrolyzers in literature. The addition of 3D electrodes to the ElectroCell MicroFlow cell results in a significant increase in productivity. Four different expanded meshes and two woven meshes were investigated for this chapter. For each of them, a significant increase in the limiting current density is observed. This increase is the result of two effects: 1) the 3D structure typically results in a larger electrode area and 2) there is a turbulence promoting effect due to the shape of the mesh. In order to distinguish between both effects, a surface area is defined for the expanded and woven mesh electrodes. Taking into account this surface area, the mass transfer enhancement due to the turbulence promoting effect is between a factor 2.1 to 2.8. Considering that the surface area of a woven mesh is roughly three times higher than that of a flat plate, this results in an overall reaction rate enhancement factor between 5.9 and 6.7. The expanded mesh electrodes increase the available surface area by a factor 0.9 to 1.4 and therefore the overall reaction rate is enhanced by a factor 1.9 to 3.0.

It is clear that a significant increase in productivity can be achieved by using 3D electrodes. In combination with optimized designs for the inlets and the reactor channel, intensified electrochemical reactors can be constructed. The electrodes shown in chapter 5 were constructed using traditional manufacturing. Currently, it is possible to 3D print metal electrodes and achieve more complicated designs cost-effectively. A potentially interesting area of future research is to investigate such 3D printed electrodes in combination with complex printed reactor geometries. Together, these could result in truly innovative and intensified electrolyzers.

List of publications

Articles

Weusten SJC, de Groot MT, van der Schaaf J, 2020, A comparative study of the stability of hexachloroiridate and hexacyanoferrate in electrochemical mass transfer measurements, J. Electroanal. Chem., doi: j.jelechem.2020.114512

Weusten SJC, Murrer LCEM, de Groot MT, van der Schaaf J, 2021, Mass transfer in 3D-printed electrolyzers: The importance of inlet effects, AIChE J., doi: aic 17263

Weusten SJC, Murrer LCEM, van der Schaaf J, de Groot MT, submitted, Mass transfer in 3D printed electrolyzers: The effect of inlets and developing flow on local mass transfer

Weusten SJC, van der Schaaf J, de Groot MT, submitted, Mass transfer in the ElectroCell Microflow and MP cell and the effect of mesh electrodes

Oral presentations

Weusten SJC, Murrer LCEM, de Groot MT, van der Schaaf J, Mass transfer correlations in laboratory scale parallel plate electrolyzers: effect of 3D electrodes and gas evolution, 10th World Congress of Chemical Engineering, 1-5 October, Barcelona

Weusten SJC, de Groot MT, van der Schaaf J Hexachloroiridate as an alternative to hexacyanoferrate in electrochemical mass transfer measurements, AIChE Annual Meeting, 10-15 November 2019, Orlando

Weusten SJC, Murrer LCEM, de Groot MT, van der Schaaf J, Demystifying mass transfer in electrolyzers through 3D printed parallel plate cells: the importance of inlet effects, AIChE Annual Meeting, 10-15 November 2019, Orlando

Weusten SJC, Murrer LCEM, de Groot MT, van der Schaaf J, Demystifying mass transfer in electrolyzers through rapid prototyping with 3D printed parallel plate cells, AIChE Annual Meeting, 10-15 November 2019, Orlando

Weusten SJC, Murrer LCEM, van der Schaaf J, de Groot MT, Improved reactor design using 3D printed electrolyzers, 12th European Symposium on Electrochemical Engineering, 13-17 June 2021, Leeuwarden

Poster Presentations

Weusten SJC, Murrer LCEM, de Groot MT, van der Schaaf J, Rapid prototyping through 3D printing as a tool for achieving intensified electrolyzer designs, Leuven, The second international process intensification conference, 27-29 may 2019, Leuven

Acknowledgements

The research presented in this thesis was performed as part of the HIGHSINC project, a joint endeavor by TU Eindhoven and AkzoNobel (now Nobian). This project has lead to interesting developments, which I am grateful to have seen unfold from a front line perspective. I thank the TU/e and AkzoNobel for investing into this project. I also thank the committee members for reviewing the resulting thesis.

Behind every large organisation there are people who make a difference. John van der Schaaf and Thijs de Groot are examples of this. Through their guidance I was pushed to discover more, question more deeply and think more critically. John, you especially had a way of asking deep questions that could throw the investigation into unexpected directions. Through the unexpected, knowledge often followed and for that I am thankful to you. Thijs, as a daily supervisor, you regularly went above and beyond in your support, and made sure that I could overcome any obstacle we faced. There are too many of those to list, but thanks to you I never had to doubt whether we would make it past them.

Within the extended network around this project there are people who offered support despite not having a direct incentive to do so. I am especially thankful to Bert Vreeman for following this project closely and offering insight. Bert, it is clear that you are passionate about science and that that passion has lead to considerable knowledge. You never hesitated to share that knowledge, for which I am thankful. To Paola Granados-Mendoza and Riaan Schmuhl I am thankful as they always took the time to catch up and ask how things were going. Their kind words helped push past some of the tougher moments during the project.

Technicians are the unsung heros of science: They do not get the recognition of a high-ranking academic and they are often taken for granted. Yet, they are a crucially important part of the scientific machine. Without them, it would be near impossible to achieve anything productive in the lab. Equipment would go unmaintained, complicated procedures would go unexplained and due to the second law of thermodynamics, chaos would be inevitable. Peter and Marlies, thank you for having the patience to explain and help us through the plentiful technical difficulties. Erik and Madan, if anything needed to be built it was always you who had the best ideas. I cannot imagine how poorly designed our contraptions would be without your insight. Carlo, you had perhaps the most thankless job of all, as you were the one who made sure we did not accidently destroy ourselves in the lab. Despite this surprisingly difficult job, you were always happy to help us with our questions.

Metaphorically, a PhD project is similar to a train journey: You are on your way to a destination and you are faced with many stops. Throughout this journey, you see fellow travelers come and go. Some of those travelers you might only see for a fraction of time and yet, they can leave lasting impressions. Such is the case for the many collegues I have had over the years at the TU Eindhoven. To my colleagues at reactor engineering, I will not forget the moments we shared and the support we found in eachother in darker days. Pia, Carola, Ria, Luc, Rodrigo, you were the ones I worked most closely with and will remember most fondly. We rode the rollercoaster of science together and shared plenty of ups and downs. It was great having you as colleagues and I hope the best for you.

About the author

Stephane Weusten was born on the 20th of May 1994 in Tongeren, Belgium. In 2011 he started studying Chemistry at Hasselt University with a focus on materials science. During this time, he completed an Erasmus exchange to Université de Montpellier 2 and attended the a summerschool at Manchester University. He obtained his bachelor degree in 2015, with his final project focused on electrochemical mass transfer in the rotor-stator spinning mesh reactor. Subsequently, he enrolled in the master of Chemical Engineering at the Technical University of Eindhoven with a focus on chemical process technology. As part of this degree program, he interned at AkzoNobel RD&I in deventer where he investigated the mass transfer performance of the ElectroCell MP Cell. Research for the MSc graduation project was performed within the group of dr. ir. J. van der Schaaf, where he investigated hexachloroiridate and how this species could be used to measure the performance of 3D electrodes in the ElectroCell MicroFlow cell. Immediately after obtaining his masters degree with honors in 2017, he started his PhD within the Laboratory of Chemical Reactor Engineering, now Sustainable Process Engineering, at the Technical University of Eindhoven. The project was under the supervision of dr. ir. J. van der Schaaf and dr. ir. M.T. de Groot, in collaboration with AkzoNobel (now Nobian) as an industrial partner. This resulted in this PhD thesis titled “Demystifying mass transfer in electrolysis through 3D printed reactors“.